

**CHEMICAL CHARACTERIZATION OF AFRICAN BIOMASS BURNING
OVER THE SOUTHEAST ATLANTIC OCEAN**

A THESIS SUBMITTED TO THE GRADUATE DIVISION OF THE UNIVERSITY OF
HAWAI'I AT MĀNOA IN PARTIAL FULFILLMENT OF THE REQUIREMENTS FOR
THE DEGREE OF

MASTER OF SCIENCE

IN

OCEANOGRAPHY

MAY 2018

By
Amie Dobracki

Thesis Committee:

Steve Howell, Chairperson
Jennifer Griswold
Kathleen Ruttenberg

TABLE OF CONTENTS

LIST OF TABLES	iii
LIST OF FIGURES	iv
CHAPTER 1 : INTRODUCTION	1
1.1 Atmospheric Aerosol	2
1.1.1 Chemical Composition	5
1.1.2 Optical Properties	7
1.1.3 Hygroscopicity and CCN	8
1.1.4 Aerosol and Climate	9
1.2 Biomass Burning Aerosol	13
1.2.1 Organic Aerosol	15
1.3 African Biomass Burning and the Southeast Atlantic.....	16
1.3.1 SAFARI 2000.....	17
1.3.2 ORACLES	18
CHAPTER 2 : METHODS.....	21
2.1 Sampling inlet.....	21
2.2 Instrumentation	22
2.2.1 Counting Instruments	22
2.2.2 Optical Instruments	24
2.2.3 Composition Instruments.....	25
2.2.4 Sampling Issues.....	30
CHAPTER 3 : RESULTS	34
3.1 Plume Structure and Chemical Composition.....	35
CHAPTER 4 : DISCUSSION.....	44
4.1 Organic Aerosol	46
4.2 Other Chemical Tracers of Biomass Burning	55
4.3 Aerosol Acid/Base Balance	59
4.4 Back Trajectories and Modeling Observations	62

4.5 Comprehensive Studies	69
4.6 SAFARI 2000 Comparison	72
CHAPTER 5 : CONCLUSION	78
Appendix A	82
Appendix B	86
Appendix C	96
Appendix D	107
Appendix E	110
Appendix F	117
REFERENCES.....	120

LIST OF TABLES

<u>Table</u>	<u>Page</u>
1 Date of flight, flight number, and a short description of the flight.....	35
2 Summary of BBOA age indicators	45
3 Average oxidation state values.....	51

LIST OF FIGURES

<u>Figure</u>	<u>Page</u>
1 Schematic of aerosol modes.....	5
2 Chemical composition of submicron aerosol from different regions.....	7
3 Earth’s global energy balance.....	10
4 Direct and indirect effects of aerosol.....	11
5 IPCC sources of radiative forcing	12
6 Key processes occurring in marine stratocumulus clouds	13
7 Physical processes affecting biomass burning over the SEA.....	17
8 Direct, semi-direct, and indirect aerosol effects on climate over the SE Atlantic.....	19
9 HIGEAR sizing instruments, and the size ranges in which they sample.....	24
10 Schematic of the Aerodyne HR-ToF-AMS.....	26
11 Schematic diagram of HIGEAR rack set up	28
12 Time series plot of subratio	30
13 ORACLES 2016 flight track.....	34
14 Average mass spectra results from clean and polluted aerosol	36
15 Box plots of altitude and bulk species	37
16 Altitude vs latitude plot colored by NO ₃ :OA	39
17 Box plots of latitude and OA.....	41
18 WRF-AAM CO (ppb) and wind forecast at 700mb.....	42
19 OA age indicators and lifetime in atmosphere.....	45
20 Schematic Van Krevelen diagrams.....	47
21 ORACLES 2016 Van Krevelen diagram	48
22 Van Krevelen diagram adapted from Heald et al. (2010)	50
23 Average oxidation state for each flight.....	52
24 Schematic f44 v 60 diagram	53

25	ORACLES 2016 f44 vs f60 plots	55
26	Schematic of BBOA and modified combustion efficiency.....	56
27	BC vs CO for routine and TOO flights	57
28	OA vs CO for routine and TOO flights	59
29	OA vs BC for routine and TOO flights.....	59
30	Acid/Base molar ratios	61
31	HYSPLIT back trajectory and MODIS fire image.....	63
32	HYSPLIT back trajectory over mixed layer depth.....	64
33	ORACLES in situ f44 compared to WRF mean age cross section.....	66
34	Age vs TOC/BC	68
35	SAFARI 2000 flight tracks.....	70
36	SAFARI 2000 and ORACLES 2016 pie chart comparison	72
37	Vertical structure of BB from SAFARI 2000	74
38	Chemical ratios of SAFARI 2000 data	75
39	SAFARI 2000 HYSPLIT back trajectories	77

List of Abbreviations

AAE	Absorption Angstrom Exponent
AMS	Aerosol Mass Spectrometer
BB	Biomass Burning
BBOA	Biomass Burning Organic Aerosol
BC	Black Carbon
BrC	Brown Carbon
CCN	Cloud Condensation Nuclei
CE	Collection Efficiency
CO	Carbon Monoxide
CO ₂	Carbon Dioxide
EC	Elemental Carbon
ER	Enhancement Ratio
HIGEAR	Hawaii Group for Environmental Aerosol Research
IE	Ionization Efficiency
IPCC	Intergovernmental Panel on Climate Change
LV-OOA	Low Volatility Oxidized Organic Aerosol
LWC	Liquid Water Content
MBL	Marine Boundary Layer
NH ₄	Ammonium
NO ₃	Nitrate
OM	Organic Matter
OOA	Oxidized Organic Aerosol
ORACLES	Observations of Aerosols above Clouds and their Interactions
OA	Organic Aerosol
OC	Organic Carbon
OSc	Oxidation State
PM	Particulate Matter
POA	Primary Organic Aerosol

Ppb	Parts per billion
Ppm	Parts per Million
RF	Research Flight
RH	Relative Humidity
SAFARI 2000	Southern African Regional Science Initiative
SDI	Solid Diffuser Inlet
SEA	Southeast Atlantic Ocean
SO ₄	Sulfate
SOA	Secondary Organic Aerosol
SSA	Single Scattering Albedo
SST	Sea Surface Temperature
SV-OOA	Semi Volatile Oxidized Organic Aerosol
TC	Total Carbon
TOC	Total Organic Carbon
TOO	Target of Opportunity
WRF	Weather Research and Forecasting Model

Chapter 1. Introduction

Southern Africa produces almost a third of the Earth's biomass burning particles. These particles are transported westward over the southeast Atlantic Ocean (SEA) where a major stratocumulus cloud deck lies. The physical, optical, and chemical properties of the aerosol present in this region are not well captured by satellite retrievals. Models also have a hard time capturing the vertical and spatial distribution of aerosol, and the ability of aerosol to absorb shortwave radiation (Eck et al., 2013; Zuidema et al., 2016). Models and satellite retrievals poorly categorize the effects that aerosol has on the underlying cloud deck, which can alter predictions of low-cloud albedo. The latest Intergovernmental Panel on Climate Change (IPCC) report classifies aerosol-cloud interactions in climate models as the source of the greatest uncertainty in estimates of future climate.

Field campaigns are one way to help reduce this uncertainty. The Observations of Aerosols above CLouds and their interactions (ORACLES) campaign is a five-year investigation designed to study aerosol-cloud interactions. The project has three, one-month observation periods during September 2016, August 2017, and October 2018. The three field deployments will allow researchers to study the seasonal evolution of the chemical, physical, and optical properties of aerosol. The project is designed to combine in situ aerosol sampling with remote sensing retrieval to provide datasets that support future satellite retrievals, and to improve global and regional climate models (Redemann, 2015; Zuidema et al., 2016).

The main objectives of this thesis are to use data from in situ measurements to characterize and explain the chemical structure and properties of the biomass burning plume over the SEA. We use standard chemical analyses of organic aerosol, nitrates, sulfates, ammonium, black carbon, carbon monoxide, and carbon dioxide to track aerosol evolution in the

atmosphere. One major contribution we are looking to make is to expand research on how aerosol ages, and how aging processes drive changes in chemical properties. Not only will these results be helpful to the community of researchers studying aerosol, but the results will also help modelers spatially capture aerosol chemical properties.

1.1 Atmospheric Aerosol

1.1.1 Background

Atmospheric aerosols, suspended solid or liquid particles having diameters between 10^{-9} and 10^{-4} m in air (Poschl et al., 2005), significantly impact human respiratory health, geochemical cycling, and the global climate (IPCC 2013). They originate from a variety of natural and anthropogenic sources, such as emissions from vehicles, vegetation, volcanoes, sea spray, and biomass burning (BB). Atmospheric processes cause aerosols to undergo chemical and physical transformations, which can alter particle size and chemical composition (Jimenez et al., 2009). Understanding these physical and chemical properties and the ways they change is critical for assessing the impacts of aerosols within the atmosphere.

1.1.2 Physical Properties

Since aerosol particles range over five orders of magnitude in diameter and 15 in mass, the physics governing their behavior and their effects on the environment are strongly size dependent. Aerosols are often grouped into three broad size ranges: nucleation, accumulation, and coarse modes. These ranges are not rigidly defined, and there is considerable overlap, but this classification system is a convenient way to treat aerosol size distributions. When referring to particle diameter, one must be aware of the

implicit assumption that particles are spheres. This assumption works adequately for many types of aerosols, but is not always true, and can complicate data interpretation.

The smallest group of aerosol, the nucleation mode, accounts for particles between 1nm and ~100nm in diameter. These particles are generated by homogeneous nucleation in the atmosphere, or as combustion products cool and condense. The lifetime of nucleation mode particles in the atmosphere is typically short (seconds to days), since they diffuse rapidly and coagulate to form larger particles (Seinfeld and Pandis, 2016; Davies, 2015). Aerosols ranging from 100nm to roughly 800nm are known as accumulation mode particles. Particles in the accumulation mode are mainly formed from coagulation of nucleation particles. They have a relatively long lifetime (days) in the atmosphere because the only effective removal mechanism for accumulation mode particles is precipitation scavenging; their long lifetime allows these particles to be transported long distances. Accumulation mode particles are also important for cloud formation (Lagzi et al., 2013; Seinfeld and Pandis, 2016). Coarse mode particles with diameters > 800nm (Seinfeld and Pandis, 2016, Davies, 2015) are formed by mechanical processes, from both anthropogenic and natural sources, such as sea salt from ocean spray, dust, and biological material (Lagzi et al., 2013). Coarse particles, particularly those >10 μ m, have significant sedimentation speeds, and hence short lifetimes in the atmosphere.

Deposition is the process by which aerosol concentrations decrease in the atmosphere, due to collection or deposition of particles on the Earth's surface. The two deposition processes are dry and wet deposition. In dry deposition, particles deposit on the Earth's surface either through Brownian diffusion (nucleation mode) or gravitational

settling (coarse particles). Wet deposition refers to the scavenging of aerosols via precipitation. Below-cloud scavenging happens when falling precipitation, such as rain or snow, collides with aerosols. In-cloud scavenging occurs as cloud droplets, each one formed by condensation on an aerosol particle, combine to form rain and snow. It takes roughly one million $10\mu\text{m}$ cloud droplets to form a 1mm rain drop, rendering this an effective removal mechanism (ie. Section 1.1.5 for more discussion of aerosols and cloud droplets). Wet deposition is the only mechanism for removing accumulation mode particles, but it also removes nucleation and coarse mode particles.

A schematic diagram of these three modes of aerosol is illustrated in Figure 1a; emission and removal processes are indicated. Aerosol distributions can also be expressed in terms of particle surface area, volume or mass (Figure 1b). For example, nucleation mode may account for the majority of aerosol number, but the size of nucleation mode particles results in little contribution to the surface area, mass, or volume of the total aerosol. These figures are meant to be illustrative of the three modes; real atmospheric processes and aerosols are much more complex than these figures convey.

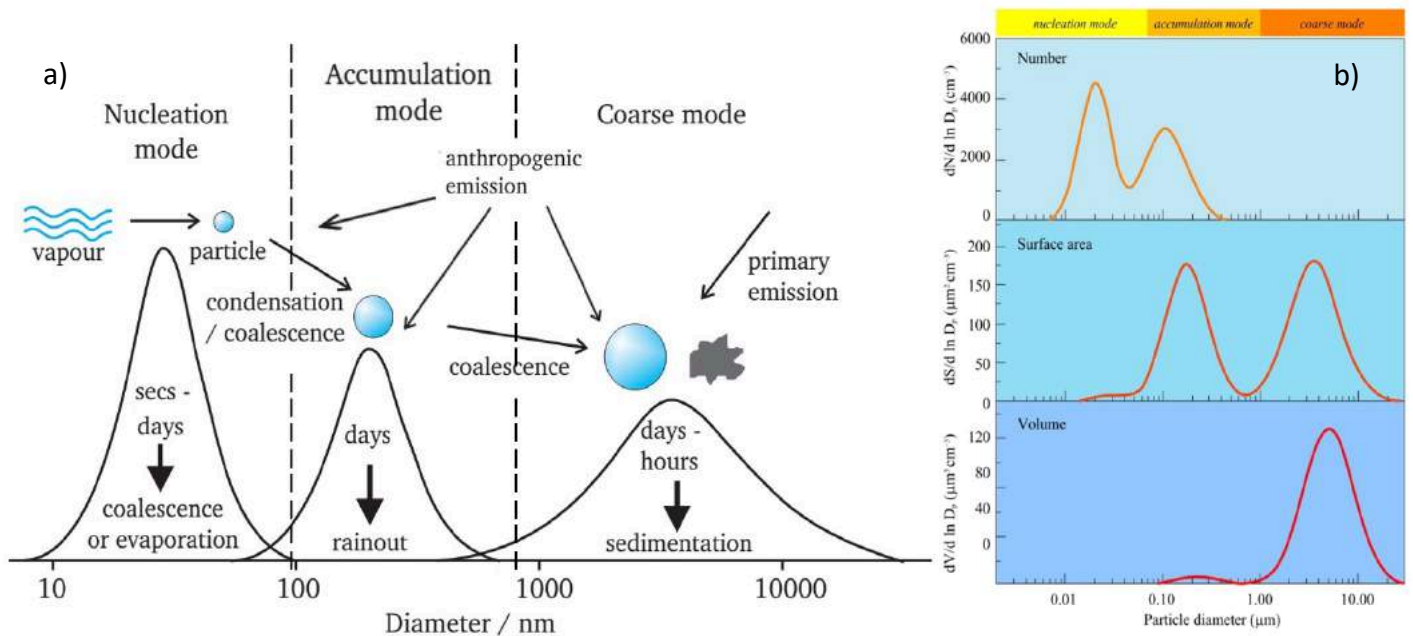


Figure 1 a) Schematic diagram of aerosol nucleation adapted from Lagzi et al. (2013). Nucleation, accumulation, and coarse mode size distributions are represented, along with their emission and removal processes. Blue circles are schematic—they dramatically understate the diameter disparity between modes. **b)** Number (cm^{-3}), surface ($\mu\text{m}^2\text{cm}^{-3}$) and volume ($\mu\text{m}^3\text{cm}^{-3}$) distributions for a typical aerosol population (Lagzi et al., 2013).

1.1.2 Chemical Composition

Composition varies across particle sizes. Coarse mode particles are generally crustal material (dust) or sea salt. While both contribute to smaller particles, as well, dust and sea salt are usually a small fraction of accumulation and nucleation mode particles. Nucleation and accumulation mode particles are primarily made up of inorganic sulfate, nitrate, ammonium salts, and carbonaceous material. Sulfates (SO_4) are formed from oxidation of sulfur dioxide (SO_2) derived from volcanoes, anthropogenic sources such as coal and oil burning, and from dimethyl sulfide (DMS), a vapor produced by some marine algae. Nitrates (NO_3) are produced naturally from lightning, and anthropogenically by high temperature combustion and burning of nitrogen containing organic materials (Lagzi et al., 2013; Seinfeld and Pandis, 2016). Ammonia

(NH₃) is the most common base in the atmosphere, and can react with various acids to form ammonium salts (see Section 4.3). Organic Aerosols (OA) can be produced directly, often from combustion, but sea spray containing organic material or suspension of spores and bacteria can also contribute to OA. OA can form as oxidation from organic vapors which produce low-volatility products, as well OA refers to the entire mass of particulate organic material, whereas Organic Carbon (OC) refers to the carbon fraction of OA (Lagzi et al., 2013; Seinfeld and Pandis, 2016). Another component of carbonaceous aerosol is elemental carbon (EC), also known as black carbon (BC), soot, or graphitic carbon. The variety for terms for EC are a consequence of different measurement techniques and hint at the difficulty of measuring or even defining the exact nature of EC. EC is the most refractory component of carbonaceous aerosols (Tomasi et al., 2016); it is formed exclusively by combustion, and it efficiently absorbs light of all wavelengths.

Fairly typical chemical compositions for urban, biomass burning, marine, and remote accumulation mode aerosol are represented in Figures 2a-e. The data used to construct the pie charts in Figure 2 correspond to the mass fraction percent of the total submicron particles. These data correspond to the mass fraction percent of the total submicron particles. These results are not rigidly defined for each source. For example, urban aerosols in South Africa are chemically different than aerosols in Mexico City, Mexico (Haywood et al., 2003; Jimenez et al., 2009). The variable distribution of components indicates that different regions produce chemically distinct aerosols (Figure 2a-e).

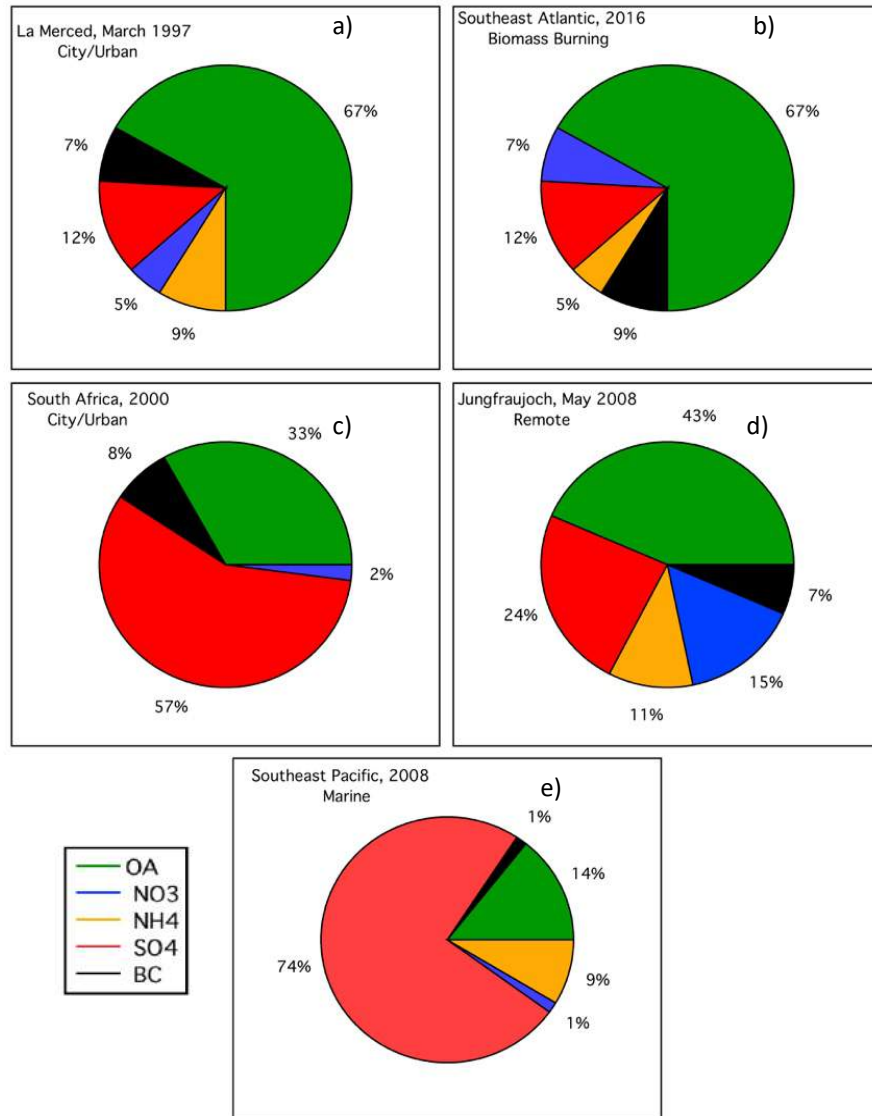


Figure 2. Chemical composition of submicron aerosols from different regions. **a)** Mexico City urban pollution (Chow et al., 2002); **b)** Biomass Burning pollution over the Southeast Atlantic; **c)** South Africa urban/biomass burning pollution (Sinha et al., 2003); **d)** Remote aerosol from Jungfraujoch, Switzerland (Lanz et al., 2010); **e)** Marine Aerosol from the South Pacific during the 2008 VOCALS experiment (Shank et al., 2011).

1.1.3 Optical Properties

Aerosol particles scatter and absorb light, affecting visibility and the Earth's radiative energy balance. Scattering is primarily a function of particle size and the wavelength of light. Accumulation mode particles are particularly effective at scattering,

since their size is close to the wavelengths of visible light. Absorption is more dependent than scattering on aerosol chemical composition. While all aerosol species scatter incoming radiation, absorption is limited to EC, some organics (usually dubbed brown carbon, or BrC), and dust. Dust and BrC primarily absorb relatively short (blue/green) wavelengths, whereas EC absorbs across the entire spectrum.

One commonly applied optical property is the single scattering albedo (SSA). The SSA is the ratio of scattering to total extinction (extinction is scattering + absorption); this term appears in the radiation calculation schemes used to determine aerosol forcing of climate (e.g. Chylek and Wong, 1995; Moosmüller and Sorenson, 2018). Another intensive property often used in large-scale models is the Absorption Ångström Exponent (AAE), defined as the negative of the slope of a log-log plot of absorption versus wavelength. The absorption efficiency of pure graphite is inversely proportional to the wavelength, yielding $AAE=1$. Absorption by BrC and dust are more strongly wavelength dependent, yielding $AAE=2$ or 3 for BrC and as high as 6 for dust. The relationship between wavelength and absorption is much more complicated when using in situ aerosol data, but over the relatively small wavelength range of visible light, the AAE is a satisfactory approximation.

1.1.4 Hygroscopicity and CCN

Salts found in aerosols are hygroscopic, which means that they attract water and will dissolve in it at sufficiently high relative humidities (RH). As water condenses, particle volume and diameter grow, increasing scattering effectiveness. Since every salt behaves differently, scattering becomes a strong function of particle composition at a specific RH.

Hygroscopicity has implications for cloud formation, which occurs as air is lifted and cools adiabatically to greater than 100% RH. Below a critical supersaturation, water uptake by a particle is an equilibrium process, with diameter a monotonic function of RH. Above 100% supersaturation, water vapor condenses rapidly onto particles, which then form cloud droplets and grow until there is insufficient water vapor to maintain supersaturation (Nenes et al., 2009; Seinfeld and Pandis, 2016). This process is called activation, and the critical supersaturation is a function of particle size and hygroscopicity. Cloud Condensation Nucleus (CCN) measurements determine the number of particles that activate at a given supersaturation, usually between 0.1 and 1% (Hudson et al., 1993; Seinfeld and Pandis 2016). Spontaneous nucleation of water droplets from the gas phase in the absence of CCN would require supersaturations of >400% (Seinfeld and Pandis, 2016). With particles present, cloud droplets form at much lower supersaturations.

1.1.5 Aerosol and Climate

Aerosols play an important role in global climate by scattering sunlight back into space, which has a cooling effect on global climate. This is known as the “direct effect”, and the magnitude depends on particle concentrations, and vertical distribution, particle size distributions, refractive indices, shapes, hygroscopicity, and the wavelength of the incident light (Seinfeld and Pandis, 2016). Natural and anthropogenic aerosols alter the Earth’s radiation balance. Particulate matter (PM) from anthropogenic sources, such as fossil fuel burning and biomass burning, can have effects on climate forcing both regionally and globally. Radiative forcing refers to changes in the energy fluxes of solar radiation (shortwave) and terrestrial radiation (longwave) in the Earth’s atmosphere

(Poschl, 2005; Seinfeld and Pandis, 2016). Forcing can also be defined as changes in net irradiance at the top of the atmosphere, and is measured in Watts per meter squared ($W m^{-2}$) (Seinfeld and Pandis, 2016). Positive forcing implies that the longwave radiation absorbed by greenhouse gases and clouds tends to warm the atmosphere, while negative forcing implies that clouds and aerosols scatter and reflect solar radiation to provide a cooling effect (Figure 3) (Poschl, 2005; Trenberth et al., 2009). The amount of incoming and outgoing radiation is summarized in Figure 3, which also illustrates some of the processes described above. Satellites can accurately measure overall

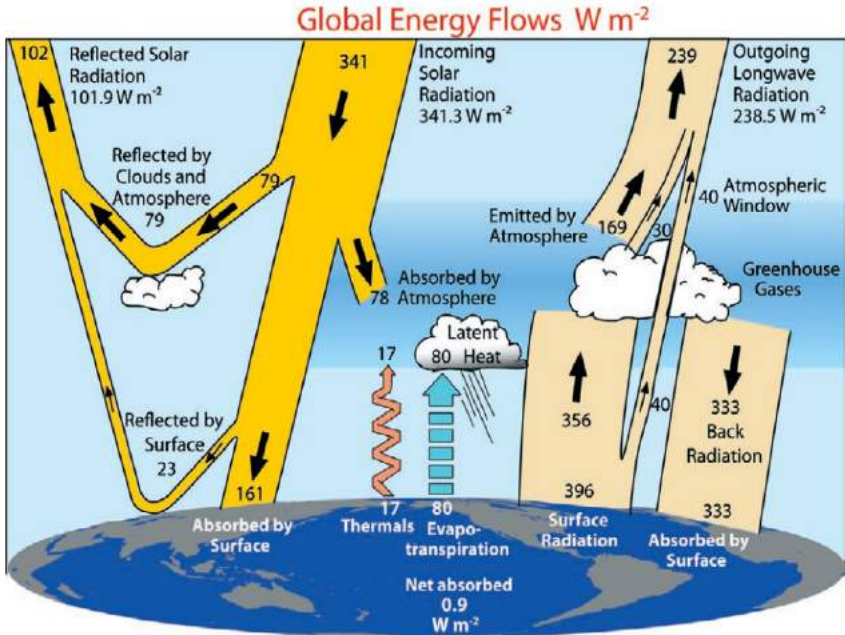


Figure 3. Earth’s global energy balance (Trenberth et al., 2009).

fluxes, but determining which processes are responsible for radiation is not a simple matter. Radiative transfer modeling, which is complex and requires accurate knowledge of aerosol optical properties and vertical distributions. Radiative transfer

modeling results are often hard to reconcile with the satellite data. In situ measurements are expensive and can only cover limited areas, but remain necessary to understand the radiative balance of the atmosphere. It is necessary to combine in situ and satellite

measurements with radiative transfer modeling to thoroughly understand the overall energy balance of the earth.

The term “indirect effect” refers to the ways in which aerosols can affect the radiation balance through altering cloud droplets (Lagzi et al., 2013). The Twomey effect was the first hypothesized indirect effect. Twomey (1977) believed that increasing concentrations of atmospheric aerosol would result in higher concentrations of CCN, thus leading to smaller cloud droplets given the same liquid water content (LWC), and an increase in cloud albedo. In 1989 the “second indirect effect” was proposed by Albrecht (1989), who noted that smaller cloud droplets suppress precipitation and thus extend the lifetime of the cloud, providing more cloud coverage and more reflective clouds. Both indirect effects lead to higher cloud albedos and thus enhanced cooling. Both the “direct” and “indirect” effects described above (Seinfeld and Pandis, 2016; Nenes, 2009) are illustrated in Figure 4. “Semidirect effects” are produced by absorbing aerosols either heating up a layer of the atmosphere and suppressing convection, or heating cloud droplets, and enhancing evaporation.

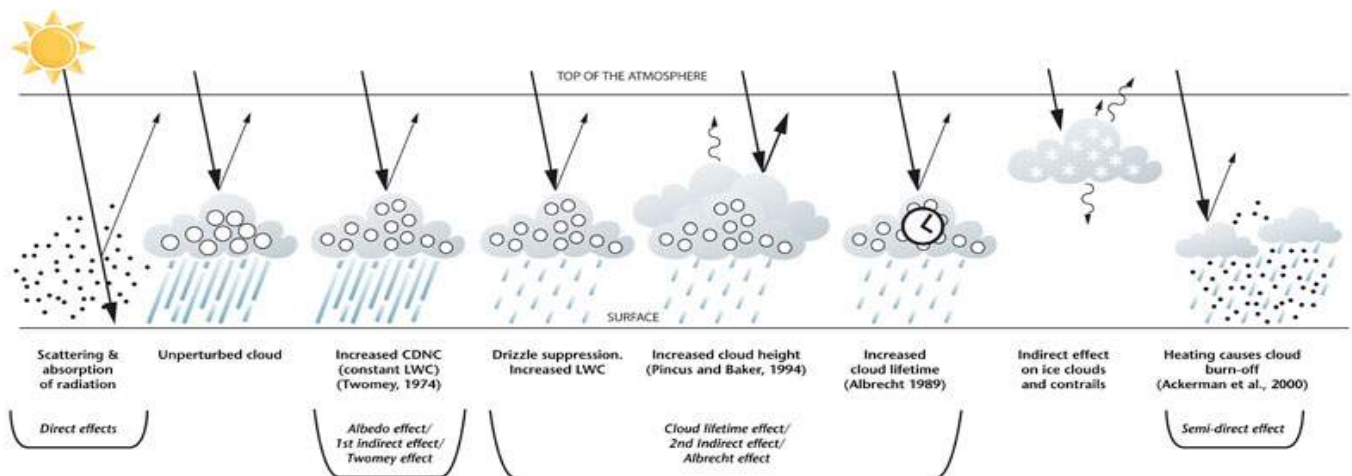


Figure 4. Direct and indirect effects of aerosol. The scattering and absorption of incoming solar radiation are illustrated. CDNC=cloud droplet number concentration, LWC=liquid water content (IPCC 2007).

Clouds and aerosols are responsible for the largest uncertainty in estimates of the Earth’s energy budget. The IPCC identifies and quantifies the magnitude of the sources of climate forcing. The different sources of radiative forcing, along with the associated magnitude and sign, are shown in Figure 5 (IPCC 2013). Aerosols and precursors are assigned a negative sign (i.e. cooling effect), while other sources like greenhouse gases have a positive sign (i.e. warming effect). Aerosols and precursors have some of the largest error bars, indicating large uncertainties (Figure 5), especially the quantification of cloud adjustments due to aerosols (“indirect effect”). The level of confidence of the forcing sources is also summarized in Figure 5. The level of confidence in understanding the direct and indirect effects of aerosols, and how they contribute to the Earth’s energy budget is low compared to other sources, such as greenhouse gases. Those uncertainties have driven much of the aerosol research over the past decade.

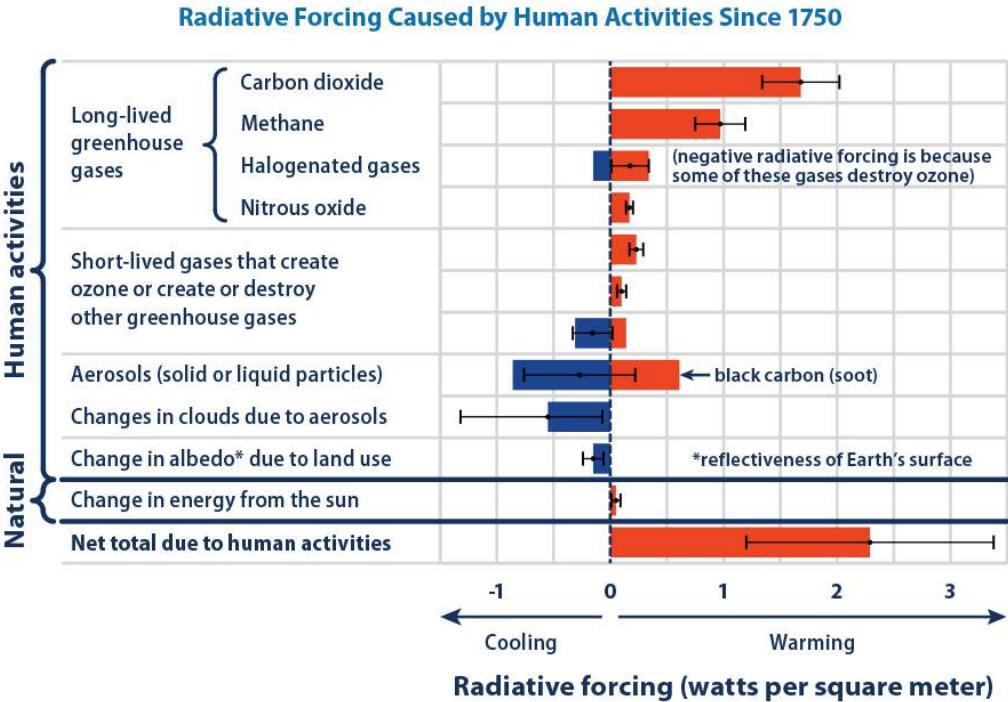


Figure 5. IPCC sources of radiative forcing and the estimated magnitude and sign (IPCC, 2013).

One type of cloud thought to be susceptible to indirect effects is the stratocumulus (Sc) cloud. This type of cloud covers roughly one-fifth of Earth's surface (23% of ocean surface, 12% of land surface), which makes them the dominant cloud type by area covered (Wood et al., 2012, Warren et al. 1986). Marine Sc clouds are particularly common off west coasts of continents where upwelling brings cool water to the surface and turbulent mixing provides these Sc clouds with cool moist air. During upwelling, cold, nutrient-rich waters are brought to the surface, producing sea-surface temperatures (SSTs) that are lower than SSTs at comparable latitudes elsewhere. This cool water limits convection and enhances stability of the marine boundary layer. Sc clouds are thin and have low supersaturations, which makes them more sensitive to the nature of CCN. This enhances the Twomey effect and other indirect effects. Key processes occurring in Sc are illustrated schematically in Figure 6. Understanding the factors that contribute to the persistence of Sc decks is essential to understanding how the coupled land-atmosphere-ocean climate system affects local and global albedo.

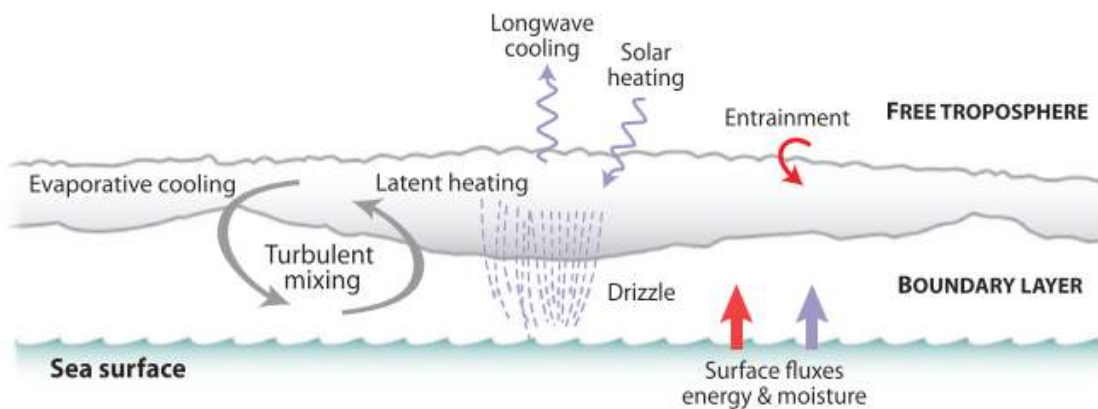


Figure 6. Key processes occurring in marine Sc clouds (Wood et al., 2012).

1.2 Biomass Burning Aerosol

Biomass burning (BB) is one of the largest contributors of aerosols to the atmosphere; it is the burning of living and dead vegetation, including but not limited to

forests, savannas, residential wood burning, and agricultural fields (Cole, 2001). It is estimated that humans are responsible for 90% of BB (Cole, 2001). BB releases over 30% of the total anthropogenic carbon into the atmosphere each year (Jacobson, 2014). The physical, chemical, and optical properties of BB aerosols have been studied for decades, all over the world (Adler et al., 2011). These studies show that BB aerosol properties are strongly dependent on fuel type, fire intensity, and meteorological conditions. However, there are some common features of BB. BB emissions are dominated by carbonaceous species, with the majority of the mass composed of gaseous combustion products such as CO₂, CO and CH₄. These gaseous components can account for up to 95% of the total emitted carbon mass (Langmann et al., 2009). The remaining fraction includes a contribution from particulate matter. BB aerosols are dominated by OC (50-60%) and BC (5-10%) (Reid et al., 2005), but also include sulfates, nitrates, chlorides, and ammonium, accounting for the remaining ~30% of the particulate matter. BB emissions on average have an SSA between 0.82 and 0.90, depending upon fire location and type of fuel being burned (Hobbs et al., 1997). The AAE is greater than 1 due to the presence of BrC in addition to BC. AAE is dependent on the fire conditions and source of the burning. Hot, flaming, efficient combustion fires result in relatively high quantities of BC and lower quantities of OC. In contrast, low flame, smoldering fires, produce copious OC and little BC. The impacts of particulate matter and greenhouse gas release from BB on atmospheric chemistry and climate is an active area of research (Cole, 2001).

1.2.1 Organic Aerosol

The origins of organic aerosol (OA) can be broadly divided into two categories, primary and secondary. Primary organic aerosol (POA) is directly released from BB, fossil fuel burning, and other sources (Jimenez et al., 2009). Secondary organic aerosols are typically formed when volatile organic precursors react to form low-volatility products that condense to produce new particles, or enlarge existing ones (Delfino et al., 2014). These reactions include oxidation, condensation, and oligomerization of organic molecules, including hydrocarbons, alcohols, aldehydes, and carboxylic acids (Andreae, 2009). OA is typically a complex mixture of hundreds of chemical species, only a small fraction of which can be individually identified. Therefore, various criteria are used to categorize different varieties of OA. Such criteria include volatility, oxidation state, and elemental ratios such as O:C and H:C

One such category, organic aerosol (OOA) is often further divided into low-volatile and semi-volatile oxygenated organic aerosols (LV-OOA, SV-OOA). The main difference between LV-OOA and SV-OOA is the level of volatility and the degree of oxidation, LV-OOA is the more oxidized species (Ng et al., 2010; Zhang et al., 2011). The mole ratio of oxygen to carbon (O:C) can be used to determine whether an aerosol is LV-OOA or SV-OOA (Zhang et al., 2007). The O:C ratio can vary widely due to influence from atmospheric conditions, burning conditions, and photochemical aging (Ng et al., 2010). Kroll et al. (2011) demonstrated that the evolution and formation of OA involves changes to oxidation state (OSc) and carbon number. They define oxidation state as $OSc = (2 \text{ O:C}) - \text{H:C}$, since atmospheric organics are mainly composed of carbon, hydrogen, and reduced oxygen. Their research provides a framework for analyzing the chemistry of

atmospheric organic aerosol using OSc and carbon number. The increase in OSc with atmospheric oxidation implies that organic compounds will favor fragmentation, or the cleavage of C-C bonds (Kroll et al., 2011).

1.3 African Biomass Burning and the Southeast Atlantic

BB in southern Africa accounts for one third (550 TgC/yr) of the Earth's BB emissions (Redemann, 2015). Smoke from southern Africa fires is lofted into the mid-troposphere and transported over the Southeast Atlantic Ocean (SEA). Peak burning in the southern Africa province occurs during the months of August through October, before the wet season begins. The major physical atmospheric and continental processes occurring over the SEA and in the south Africa region are illustrated in Figure 7. BB aerosol is emitted from hundreds of fires (green to red contours=50-300 fires per 1° box) and carried westward by 600 hPa winds (black arrows) over the SEA, where a deck of Sc clouds lie. The transported aerosol (measured by aerosol optical depth) over the SEA is colored by the warm yellow to red contours. The aerosol contours are overlaid with the cloud fraction contours in purple. The inset in the bottom left corner is an altitude (m) (y-axis) by 6°S-17°S latitude (x-axis) slice to show the deepening of the cloud boundary layer with subsiding aerosol immediately above the cloud. This inset figure in the bottom left shows direct aerosol-cloud interactions with altitude (y-axis) and latitude (x-axis). Smoke emitted from African agricultural fires can have competing radiative forcing effects on the Sc cloud deck below. The smoke has the ability to strengthen the low cloud deck with semi-direct effects above cloud to suppress drizzle and rain production, which provides an enhanced cooling effect. Alternatively, smoke can mix with the clouds and cause the semi-direct effect to occur in cloud, causing the

clouds dissipate and produce an enhanced warming effect (see Section 1.3.2) (Zuidema et al., 2015).

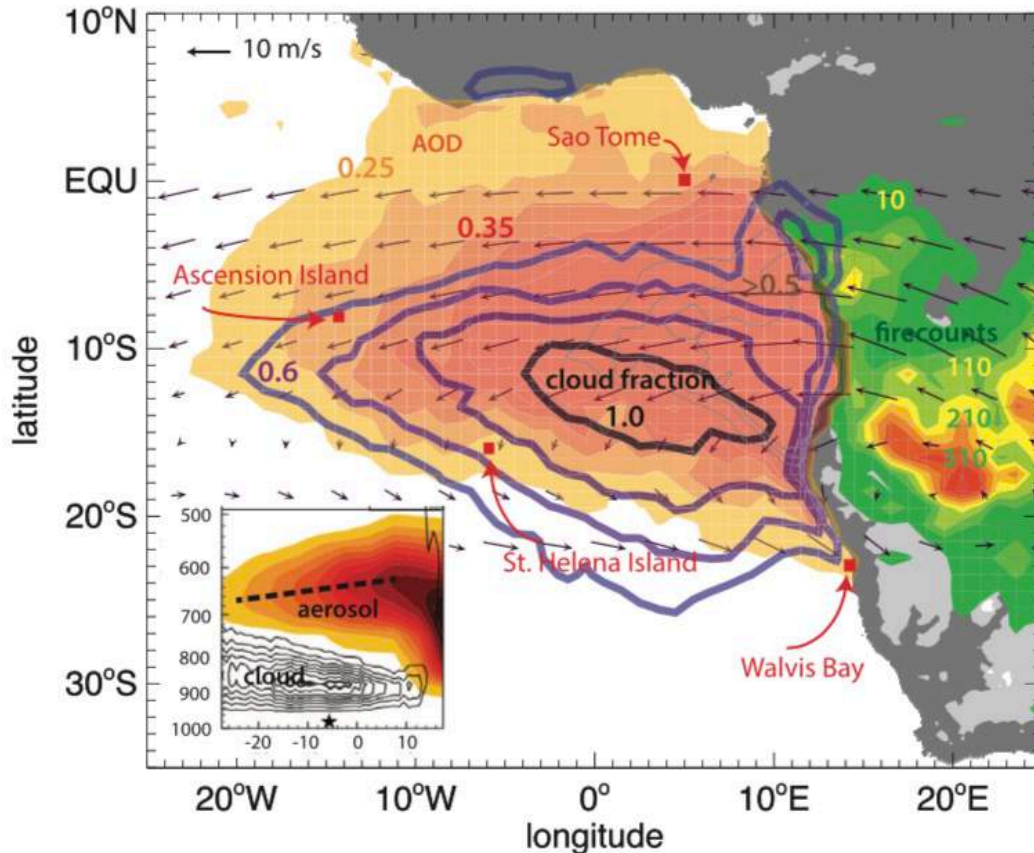


Figure 7. Illustration of African BB and climatological events that occur in the Southeast Atlantic region (Zuidema et al., 2015)

1.3.1 Safari 2000

SAFARI 2000 was a project that focused on aerosol optical and physical properties from southern African BB during the month of September 2000. The project deployed a C-130 (UK Met Office) and a Convair-580 (University of Washington) to sample BB over the SEA and over continental source regions, such as Zambia, Mozambique, Botswana, Namibia, and South Africa. This study provided some of the first data on African BB aerosol (Haywood et al., 2003; Sinha et al., 2003), and characterized the bulk chemical

species of the plume, the vertical distributions, optical properties, and the influence of BB aerosol on clouds. Methods and results from SAFARI 2000 are presented in Section 4.6.

1.3.2 ORACLES

ObseRvations of Aerosols above CLouds and their intEractionS is an ongoing five-year investigation with three seasonal observation periods (September 2016, August 2017, October 2018), designed to study key processes that determine the climate impacts of African BB aerosols (Figure 8). The ORACLES mission consists of measurements and modeling of aerosol direct, semi-direct, and indirect effects on climate. The principal goals of the experiment are:

- 1) Determine the impact of African BB aerosol on cloud properties and the radiation balance over the South Atlantic, using state of the art in situ and remote sensing instruments to generate data sets that can also be used to verify and refine current and future observation methods.
- 2) Acquire a process-level understanding of aerosol-cloud-radiation interactions, and resulting cloud adjustments that can be applied in global models.

Direct effects occur wherever aerosols are above cloud, or clouds are absent. Semi-direct effects are modulated by the vertical location of the aerosols above or within the cloud deck. Indirect effects are expected to happen when the marine boundary layer (MBL) deepens farther offshore, where aerosols become entrained and mixed into the clouds (Redemann, 2015; Zuidema et al., 2016). Determining when and where BB aerosols are entrained into the MBL and how they influence cloud microphysical properties is a critical feature in assessing the magnitude of

indirect effects. Chemical tracers such as carbon monoxide (CO) and BC can be used to observe BB entrained in the MBL. It is also important to know the chemical composition of aerosol in the free troposphere (FT) in order to observe how BB influences the MBL. A summary of the direct, indirect, and semi-direct effects can be found on Table A.1 in Appendix A.

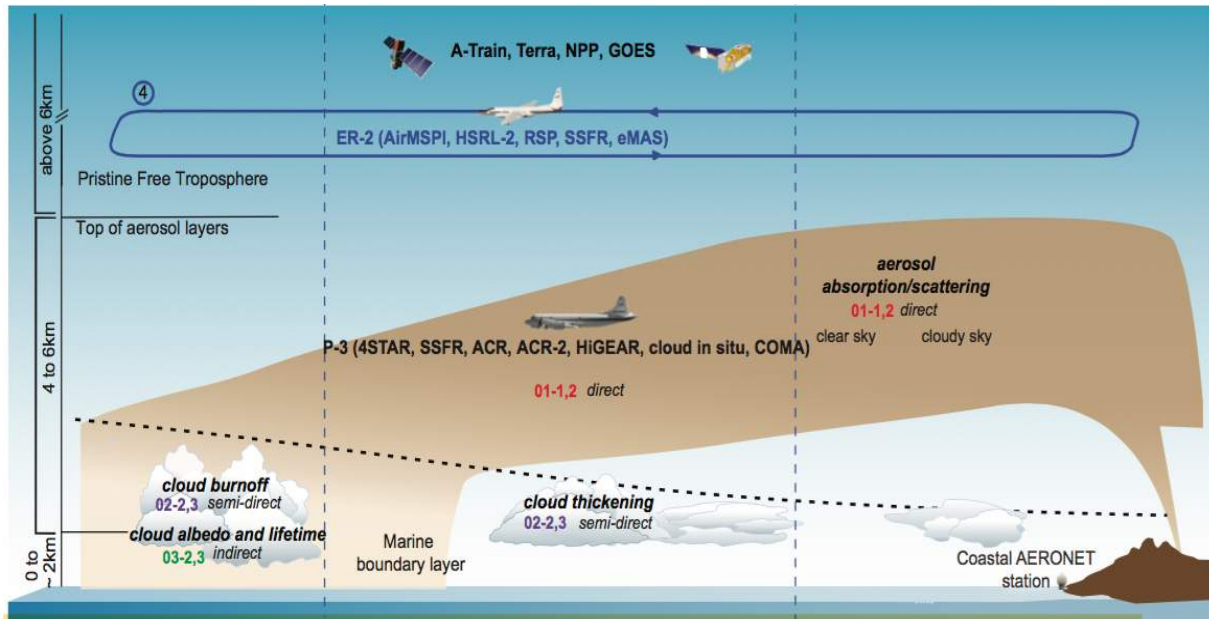


Figure 8. Direct, semi-direct, and indirect aerosol effects on climate over the SE Atlantic (Redemann et al. 2015).

The 2016 ORACLES campaign involved 15 research flights (RF) aboard the NASA P-3B operating out of Walvis Bay, Namibia, over the month of September 2016. Two transit flights, an aborted research flight, six routine flights, and six target of opportunity flights were flown. The routine flight track sampled diagonally to $\sim 10^\circ\text{S}$ regardless of meteorological conditions to ensure unbiased sampling, while the target of opportunity flights varied in sampling path and sampling objectives based upon daily meteorological reports. The campaign also deployed the ER-2, a high altitude aircraft, to provide remote sensing data, essentially acting as a virtual

satellite, but with much higher spatial resolution. The ER-2 flew a total of 10 research flights. Taken together, the campaign had 6 coordinated flights between the ER-2 and the P3-B. On these coordinated flights, the ER-2 would pass over the P-3 while it was immediately above cloud, at a pre-determined location. When practical, these flights were also coordinated with Cloud-Aerosol Lidar and Infrared Pathfinder Satellite Observation (CALIPSO) overpasses. These coordination opportunities were designed as a platform to compare in situ aerosol data to satellite and remote sensing data.

Chapter 2. Methods

The University of Hawaii Group for Environmental Aerosol Research (HIGEAR) sampled on board the NASA P3-B during ORACLES 2016. HIGEAR's instrumentation suite is described below. A summary of all instruments, the measured parameters, and the importance to this study can be found in Table A.2 in Appendix A.

2.1 Sampling Inlet

The Solid Diffuser Inlet (SDI) was used to bring ambient aerosol into the aircraft. During the DC-8 Inlet Characterization Experiment (DICE), McNaughton et al. (2007) found that SDI and ground sample submicron scattering data agreed to within 16%, and that the SDI efficiently samples dust and sea salt particles smaller than 4 μ m in dry diameter. HIGEAR's instruments were housed on four racks on board the P3-B. During the campaign, the sample flow through the tubing and instruments was measured and adjusted to ensure the air velocity through the inlet equaled flight speed (within 5%). This isokinetic sampling minimizes size-dependent sampling biases, though it cannot entirely eliminate them (Huebert et al., 1990). Aerocalc, an online particle loss calculator created by Paul Baron (http://www.tsi.com/uploadedFiles/Product_Information/Literature/Software/Aerocalc2001.xls), was used to select tubing material, length, and diameter to minimize particle loss between the SDI and HIGEAR rack instruments. Calculated losses were negligible, but such calculations are inherently optimistic, unable to account for all features of the hardware and instruments that were used. Conductive tubing was use to minimize

electrophoretic losses. Most tubing was graphite-impregnated silicone tubing, but stainless steel, copper and aluminum tubing were also used. Lines to the mass spectrometer were limited to metal tubing since there is a possibility that organic vapors from silicone could affect OA measurements. Due to differences in flow rates and paths, additional losses may have affected some instruments more than others.

2.2 Instrumentation

2.2.1 Counting Instruments

HIGEAR brought a suite of over a dozen instruments to measure the optical and physical properties of African BB. Among those instruments were two TSI 3010 condensation nuclei (CN) counters operated with a saturator/condenser temperature difference of 22°C to measure concentrations of particles > 10nm. The CN counters operated in parallel, but one of the counters had a thermal denuder at 360°C to count particles that do not volatilize at high temperatures, such as sea salt and soot. The non-heated (CNcold) counter was used to sample all refractory and non-refractory particles.

The Ultrafine Condensation Nucleus counter (UCN) (TSI 3025) was on board to measure particles > 3nm. The difference between the UCN and the CN counter (3nm < d_p < 10nm) yielded particles that are referred to as ultra-fine particles (Clarke et al., 1998), and a class which is representative of recent new particle production.

2.2.2 Sizing instruments

A long differential mobility analyzer (LDMA) (TSI 3934) was used to measure size distributions of aerosol between 10-550nm. The LDMA deployed had modified flow control, electronics, and data acquisition. The LDMA operated in a scanning mode, in

which it up-scanned for 60 seconds, drawing air from the miniature lagged aerosol grab (LAG) chamber (Clarke et al. 1998). The chamber opened for ~20 seconds every 2 minutes. A second differential mobility analyzer was also on board. The Thermal Differential Mobility Analyzer (TDMA) was used to analyze particle mass, surface area, number distribution, and mixing state over the 10nm to 300nm size range.

HIGEAR also deployed an Ultra-High Sensitivity Aerosol spectrometer (UHSAS), manufactured by DMT, to measure a different size range of particles from the TDMA, LDMA, and the UCN. The UHSAS is an optical spectrometer that measures particles from 60nm-1000nm at 1s time resolution. The UHSAS uses a laser to illuminate particles, which then scatter light that is collected on two pairs of optical detectors (Cai et al., 2008). One advantage of the UHSAS is that it sizes aerosol over the entire accumulation mode, which is useful for comparison with composition instruments.

An Aerodynamic Particle Sizer (APS, TSI model 3321) was used to measure larger particles, including dust, and particles with size ranges from 800nm to 10000nm across 50 channels. The size distributions that each instrument measures is illustrated in Figure 9. The dashed purple and red boxes denote the size range that is sampled by the AMS and SP2. A description of these instruments is provided in Section 2.2.4.

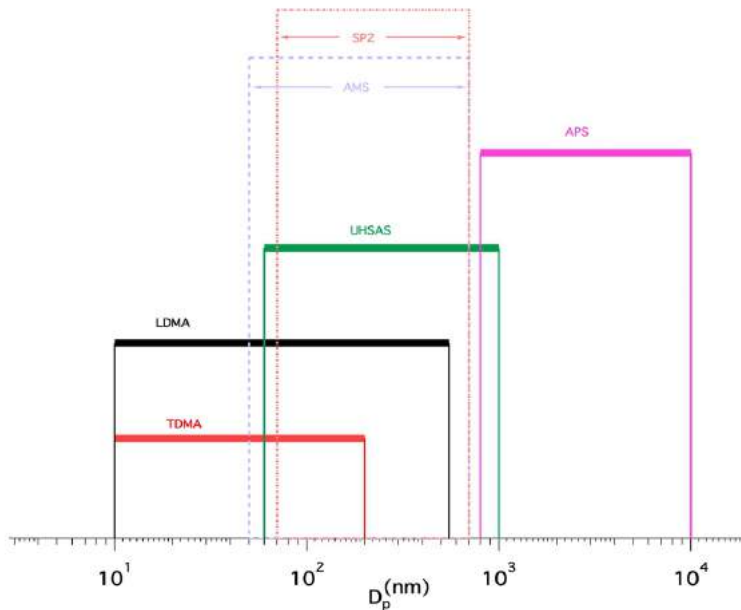


Figure 9. HIGEAR sizing instruments, and the size ranges in which they sample.

2.2.3 Optical Instruments

To study the optical properties of BBaerosol, two TSI nephelometers (model 3563) were used in series to measure total scattering and hemispheric backscattering by particles at red (700nm), green (550nm), and blue (450nm) wavelengths. Measurements were corrected according to Anderson and Ogren (1998). The first TSI nephelometer measured scattering from all particles; the second had an impactor switched in and out of its sampling line to measure all and sub-micrometer particles. Two Radiance Research single wavelength nephelometers (M903) were operated at different humidities (uncontrolled/low and 85%RH) to establish the humidity dependence of light scattering. To complete the suite of optical instruments, two Particle Soot Absorption Photometers (PSAP) (Radiance Research) were used to quantify the spectral light absorption coefficient of the total and submicron aerosol at three wavelengths (470, 530, and 660nm).

2.2.4 Composition Instruments

An Aerodyne High-Resolution Time-of-Flight Aerosol Mass Spectrometer (HR-ToF-AMS, or just AMS) was used to sample the chemical composition of non-refractory, submicron aerosols. A schematic of the AMS can be seen in Figure 10.

The AMS sampled at a rate of $\sim 1.38\text{cm}^3\text{s}^{-1}$, and used an aerodynamic lens to focus $\sim 70\text{nm}$ - 700nm particles onto a 600°C heated surface. Non-refractory particles were evaporated off the heated surface and ionized by 70 eV electron impactation. Soot, some organics, dust, and some salts are not vaporized in AMS. Lastly, the particles are carried through the chamber in either V mode or W mode and then are mass analyzed by the Time of Flight Mass Spectrometer (ToF-MS). V mode and W mode refers to the path that the particles take. V mode is a shorter path, where particles are only deflected once. The path looks like a V in the chamber (grey path in Figure 10). The particle beam in W mode deflects three times, mimicking the shape of a W (blue path in Figure 10).

The AMS was generally operated in the high sensitivity V-mode. Occasionally, during phases of flight where the aircraft stayed in plume at the same altitude for longer than 10 minutes (level leg), the high resolution W-mode was used. W-mode can offer a greater detailed chemical composition analysis, but at the cost of a 50-fold increase in detection limit. The data presented here is strictly V-mode. The concentration of the aerosol was calculated from the focused particle beam as it passed through a chopper, which alternately blocks and unblocks the particle beam. The data presented is the difference between the open sampling periods and the closed sampling periods thus subtracting background noise. For most of the project, the time resolution of the AMS was two seconds in the unblocked position and two seconds in the blocked position,

plus one second for processing, for a total of five seconds per cycle. Section 2.2.5 explains how the time resolution was selected. DeCarlo et al. (2006) provides a more detailed description of the HR-ToF-AMS.

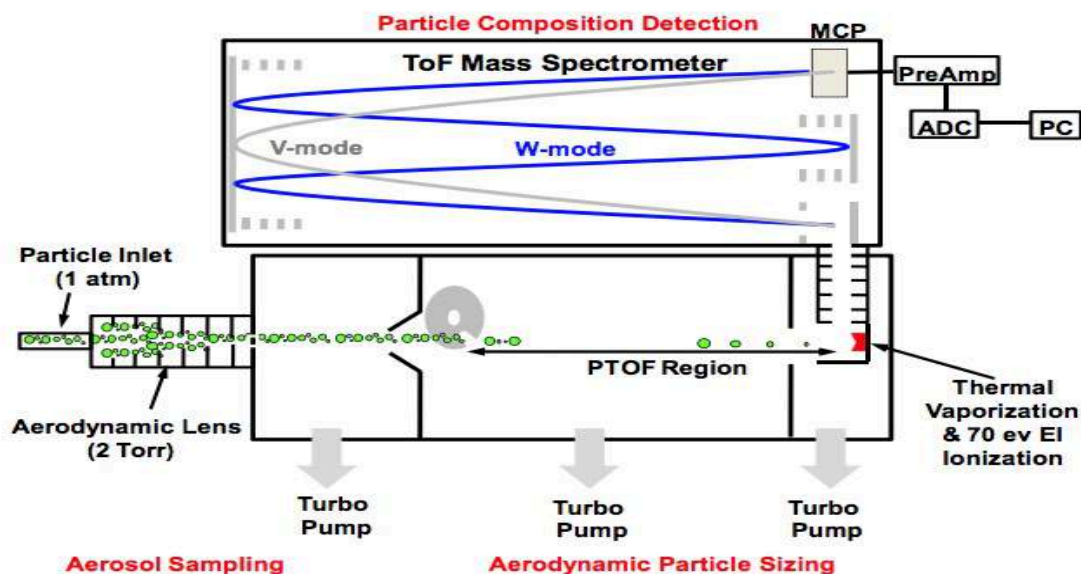


Figure 10. Schematic of the Aerodyne Aerosol Mass Spectrometer (DeCarlo et al., 2006, Sun et al., 2009)

The reported detection limit for ground based one-minute average V-mode data is $<0.04\mu\text{g m}^{-3}$ for all bulk chemical species (DeCarlo et al., 2006). However, aircraft based detection limits are usually 2-5 times higher due to higher background. When operated in an aircraft the AMS has a higher background because the instrument must be turned off each night in between flights. Ideally, the turbo pumps should be run continually, generally without ever needing to be powered down. Shutting down the AMS is not ideal because material builds up inside the vacuum chamber, which gives it the higher background values. Each morning, the AMS was turned on and heated to $\sim 700^{\circ}\text{C}$ at least two hours before flight to burn off the built up material. For some material, typically organics, this process takes several hours. Because of this, the

beginning of the flight had higher organic background, more noise, and a higher detection limit. On average the detection limit for the HIGEAR AMS bulk species was $0.15\mu\text{g}/\text{m}^3$ for organics, $0.04\mu\text{g}/\text{m}^3$ for nitrate, $0.03\mu\text{g}/\text{m}^3$ for sulfate, and $0.01\mu\text{g}/\text{m}^3$ for ammonium. These background values were determined from the noise levels during periods with a filter in the sampling line above 15,000 feet.

AMS data were processed using a data analysis software that was specifically designed for AMS users (SQUIRREL v.1.57I and PIKA v.1.16I, Sueper, 2010). SQUIRREL and PIKA are programs run in Igor Pro, a data processing and analysis package from Wavemetrics, Portland, OR. Version 6.37 was used to process ORACLES 2016 data.

A single particle soot photometer (SP2, Droplet Measurement Technology) was deployed to measure refractory black carbon particles between 70 and 700nm in real time. The SP2 used laser (1064nm) induced incandescence for quantitative detection of BC (Stephens et al., 2003). The SP2 was calibrated using fullerene soot effective density estimates from Gysel et al. (2011). Further details of the of the SP2 can be found in Schwartz et al. (2006).

A schematic HIGEAR instrumentation rack set up is shown in Figure 11. In-between the two HIGEAR racks were two racks used to house a CCN instrument (Georgia Tech, Nenes), a water isotope instrument (Oregon State University, Noone), and a photothermal interferometer (Brookhaven National Lab, Sedlacek). The distance between the HIGEAR front rack and the AMS back rack was approximately 5m, and the front rack was approximately 3m from the inlet. Having the racks so far behind the inlet

was not ideal, but due to aircraft space and needs of other instrument groups, these were the positions where HIGEAR operated.

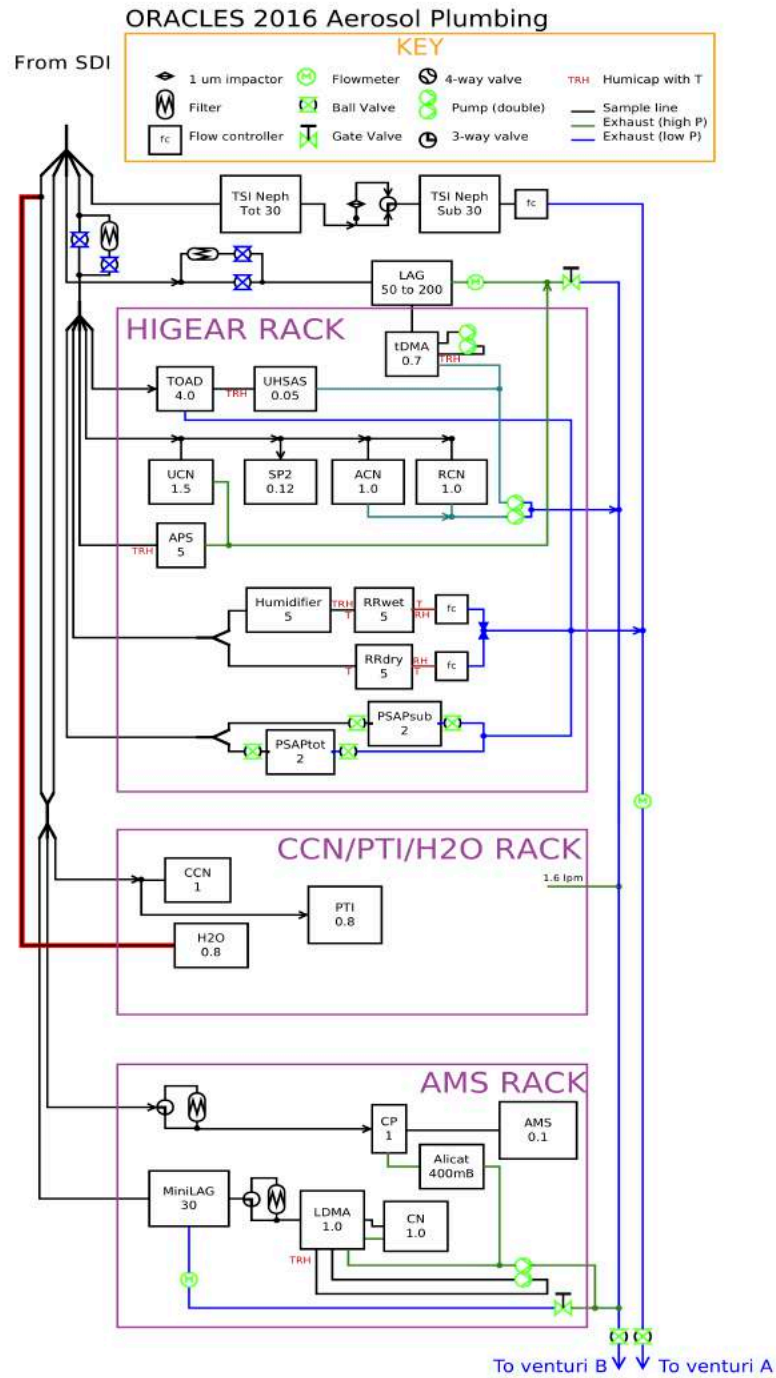


Figure 11. Schematic diagram of the HIGEAR rack set up for ORACLES 2016.

2.2.5 Sampling Issues

Because the AMS racks were ~8m behind the SDI, the potential for particle wall losses was increased. As a precaution, we calculated mass scattering efficiency from the AMS + SP2 (mass total $\mu\text{g}/\text{m}^3$) and the submicron scattering (Mm^{-1}) calculated from the TSI nephelometers (described in Section 2.2.4). We used the nephelometers because they were close to the inlet where we assumed particle losses to be minimal. Accumulation mode aerosol typically has ~5 Mm^{-1} scattering per $\mu\text{g}/\text{m}^3$ for green light (Reid et al., 1998 and Haywood et al., 2003a). This relationship is not exact; it changes with size distributions (and of course assumes that all aerosol mass is measured, which may not be the case with some particularly refractory organics, dust, and sea salt, which were not measured).

To find the mass scattering efficiency we had to make the appropriate corrections to the nephelometer data. Unfortunately, because the second TSI Nephelometer switched between total and sub-micrometer sampling, it spent very little time collecting submicrometer data. Therefore, we looked for a consistent ratio defined here as “subratio”, between total and submicrometer scattering while on level legs. In the free troposphere, the subratio was near 1.02, indicating that there was little coarse aerosol. In the boundary layer, the discrepancy was bigger, at approximately 0.85. Since the two nephelometers were in series, there were particle losses between the two and the second nephelometer consistently measured less scattering than the first, so was judged less reliable. To address this, we multiplied the total scattering from the first nephelometer by the subratio determined from the second to arrive at submicrometer scattering to compare with the composition measurements. At least three different

locations for subratio were selected per flight. Ideally, the selected data were at multiple altitudes. An example of the subratio plotted with OA and total scattering is shown in Figure 12. The red box indicates what an appropriate subratio segment looked like when we were in the plume. The blue box shows a subratio segment when we were not in the plume. The unreasonable values for the subratio in the blue box are due to insufficient aerosol loading that is calculated from values near both instruments' detection limits.

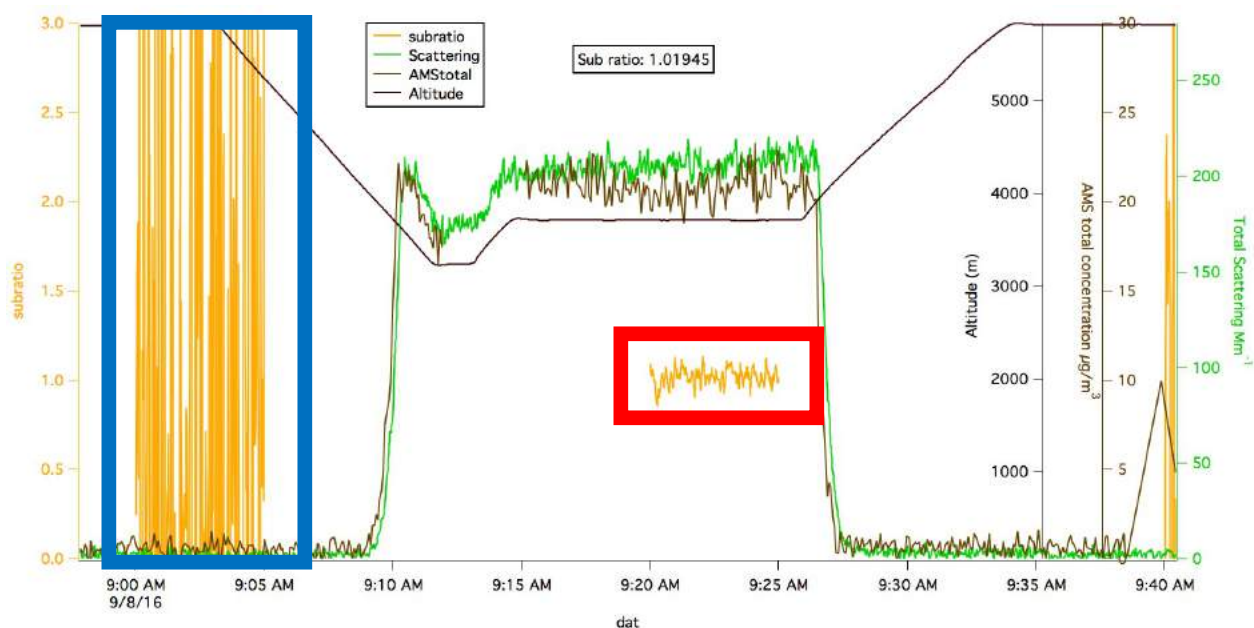


Figure 12. Time series plot of subratio (yellow), AMS total concentration (brown), total scattering (green) and altitude (black). The red box highlights the type of data we were looking for when we had the submicron data available. We were looking for in plume level legs. The blue box represents subratio in the absence of significant aerosol loading.

The values calculated for mass total ($\mu\text{g}/\text{m}^3$) versus submicron scattering (Mm^{-1}) for each flight are presented in Table A.3 in Appendix A. An example segment of the subratio plotted with time is shown in Appendix A, Figure 1. This calculation was done as a quality check to make sure we do not have major losses from the inlet and front

HIGEAR racks to the back AMS rack. We concluded from these calculations that the average mass scattering efficiency was 5.92. Even with varying mass scattering efficiencies between flights, we conclude at most 20% losses for the entire campaign.

In addition to tubing loss concerns, the collection efficiency calibration of the AMS was also a concern. The AMS collection efficiency (CE) for inorganic aerosol is calculated by comparing the molar ratio of NH_4 to SO_4 in order to determine the acidity of the aerosol. The CE for non-acidic sulfate aerosol is a constant 50% if the NH_4/SO_4 ratio is above 1. Liquid aerosol, primarily acidic aerosol such as sulfuric acid, is collected more efficiently than neutralized aerosol because it is less likely to bounce off the heater and escape detection (Huffman et al., 2005, Drewnick et al. 2003).

The AMS was calibrated by an ionization efficiency (IE) calibration using ammonium nitrate (NH_4NO_3). The calibration was carried out in the field twice, using ammonium nitrate particles that were generated from a nebulizer. The aerosol traveled through the LDMA, where a size of 300nm was selected and sent to the AMS for analysis. The IE calibration process used the concentration of nitrate in $\mu\text{g}/\text{m}^3$ detected by the AMS, and the concentration of particles (particle per cm^3) which were detected by the CN counter (described in Section 2.2.1). After collecting at least 4 samples at different concentrations, a program written by Aerodyne Inc. calculated the IE ratio. A properly functioning AMS will have an IE around 1e^{-7} for V mode sampling. We found this to be true for our AMS, with values around 1.31e^{-7} in V mode. The W mode IE calibration can be obtained in the same way.

A proper vaporizer temperature is required for optimal sampling of OA. This is a problem with some AMS instruments, as the thermocouple is on the back of the

vaporizer and may not accurately measure the temperature in the front, or may come loose. On a level leg in the plume during RF03 (09/02/16), we set the temperature of the vaporizer to 500°C, 600°C, and 700°C to observe how the concentration of real time OA changed. The nephelometers and LDMA showed constant aerosol concentrations. The measured concentration peaked at 600°C indicating that 600°C was optimal for this aerosol. Temperatures below 600°C did not efficiently sample OA, meaning the heated surface was not hot enough to evaporate the organic aerosol. Above ~700°C was too hot, and we believe some of the organic aerosol then begins to char on the heated surface and leave a sticky burnt residue behind. Temperatures between 600°C and 650°C were used for the entire campaign. Results from the temperature test can be found in Appendix A, Table A.4.

Another concern was whether or not the OA might evaporate slowing limiting our sampling rate. If evaporation times were comparable to the sampling times, then the closed period would see increased signal and the open period would miss some of the sample, therefore decreasing the measured OA. We tested the time resolution of the AMS to show how efficiently the instrument samples OA. The test demonstrated that even when using different timing, concentrations did not appreciably change, there was less than a 1% difference between a faster sampling rate (two seconds open and two seconds closed) and a slower rate (thirty seconds open and thirty seconds closed) (Figures 2 and 3 in Appendix A). Therefore, we saw either all of the OA or some fraction evaporated with a time constant much longer than 30 seconds. This 30 second time constant was particularly helpful when we were sampling elevated aerosol in long (10-30 min) level legs. We found that operating the chopper at 2 seconds open and 2

seconds closed gave fast and clear enough resolution to sample the aerosol. One second open and one second closed yielded excessively noisy mass spectra. Collecting aerosol with a time resolution greater than 30 seconds total (15 open and 15 closed) did not allow us to sample the changes in the aerosol as the plane ascended and descended through the aerosol layer.

One last thing to note is that the ionization process in the AMS makes it difficult to effectively differentiate between inorganic and organic compounds. Because the harsh ionization fragments molecules, the AMS cannot identify individual compounds. Organic nitrates and sulfates tend to break apart, separating the carbon from the N or the S. Therefore, we cannot effectively determine whether sulfates and nitrates are organic or inorganic. In the AMS community, it is common to denote nitrates and sulfates as NO_3 and SO_4 , rather than NO_3^- and SO_4^{2-} , because the actual compound is unknown.

Chapter 3. Results

ORACLES 2016 operated out of Walvis Bay, Namibia. Information on flight number, type of flight, and a brief summary of the flight are summarized in Table 1, which is also listed in Table B.1 in Appendix B. Flight number will be referenced throughout the following sections in order to present the data. Each flight track from the campaign is shown in Figure 13. The flights in red are routine flights; the remainder were target of opportunity flights (TOO). The symbols (circles) in Figure 13 are sized by

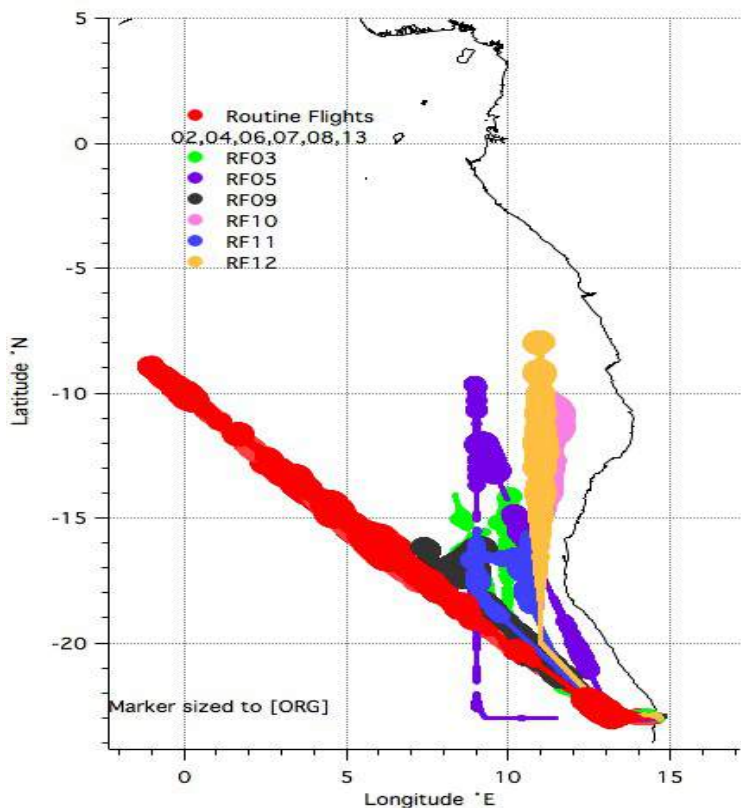


Figure 13. Map of ORACLES 2016 Flight tracks. Marker is sized to size of OA to illustrate where the plume was found.

the concentration of OA in order to illustrate where the BB air masses were located.

Routine flights were flown diagonally from -23° to -10° N, and between -1 to 15° E. TOO flight paths were more variable than routine flight paths, they were flown between -23° and -7.5° N, and 7° to 14° E. TOO flights were typically closer to the fire source because they were flown closer to the West

coast of Africa, while the routine flights sampled further west over the Atlantic.

Table 1. Table of date of flight, flight number, and a short description of the flight.

Date	Research Flight #	P-3B short description
08/31/16	02	Full routine towards 10S and 0E
09/02/16	03	TOO, mostly North along 10E
09/04/16	04	Full routine towards 10S and 0E
09/06/16	05	TOO, mixing survey
09/08/16	06	Full routine towards 10S and 0E
09/10/16	07	Routine(ish) flight to 10S and 0E
09/12/16	08	Routine(ish) flight to 10S and 0E
09/14/16	09	TOO, radiation near aerosol gradient
09/18/16	10	TOO, plume mapping
09/20/16	11	TOO, radiation fork and coordination
09/24/16	12	TOO
09/25/16	13	Routine flight to 10S and 0E

3.1 Plume Structure and Chemical Composition

African BB over the SEA had an intriguing chemical signature and structure. The concentrations of the bulk aerosol averaged over 1500m to 1000m intervals can be found in Table B.2 in Appendix B. The differences in mass spectra between clean FT (~6000m) air and polluted FT air (~3500m) are displayed in Figures 14a-b. The organic peaks (in green) dominate the polluted mass spectra (log scale on the y-axis), while the clean mass spectra have fewer organic peaks above the noise of the instrument (height of the black peaks), illustrating the low values of organic mass, near the detection limit of the instrument.

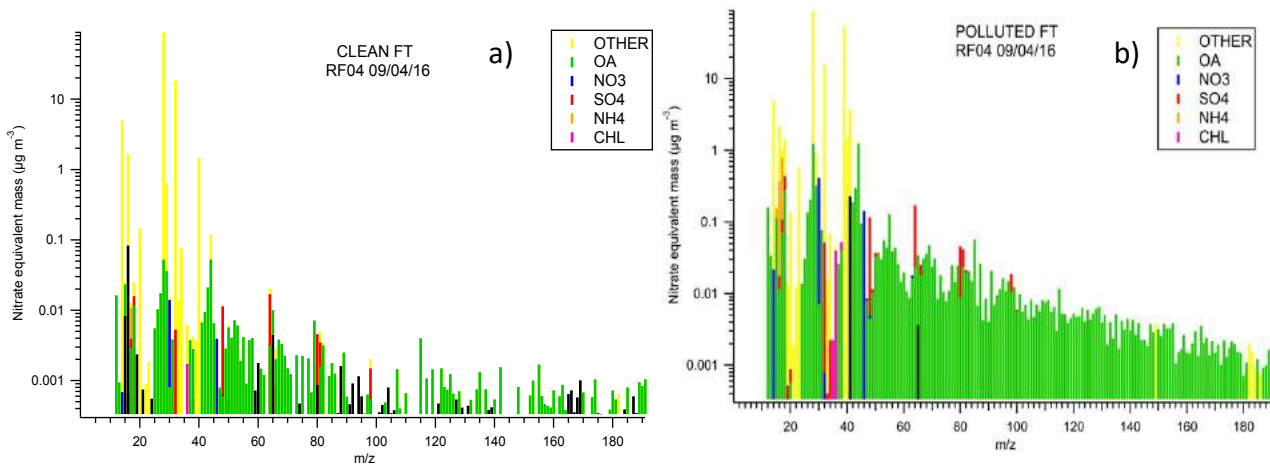


Figure 14 a) Average mass spectra results from clean (Routine Flight 4, 4 November 2016, 12:40-13:10 UTC) and **b)** polluted periods (Routine Flight 4, 4 November 2016, 08:07-09:03 UTC). Green, red, orange, blue, and pink peaks represent masses attributed to OA, NO₃, NH₄, SO₄, and Chl by the fragmentation table in SQUIRREL. Black peaks indicate negative ion fragments and reflect instrument noise. Yellow peaks represent peaks found as artifacts of the AMS such as tungsten, potassium, along with the dominating air peaks.

The majority of the plume was found between 1500m and 5500m; within the main plume, multiple aerosol layers were present. The lower layer was between 1500m and 3500m, while the upper plume layer was between 3500m and 5500m, with the greatest abundance of aerosol between 3500m and 4500m. For this study we are primarily focusing on BB aerosol in the FT, where there is little to no influence from aerosol mixing up from the MBL. We are using 1500m as a proxy for the top of the mixed layer 1`=because the mixed layer was almost always below this. Boxplots of OA, nitrate (NO₃), sulfate (SO₄), ammonium (NH₄), black carbon (BC), and delta carbon monoxide (Δ CO) (Figure 15) allow visualization of patterns of aerosol distribution. Δ CO is the difference between background concentrations of CO and elevated in plume concentrations. A more in depth description of how Δ CO is calculated can be found in Section 4.2.

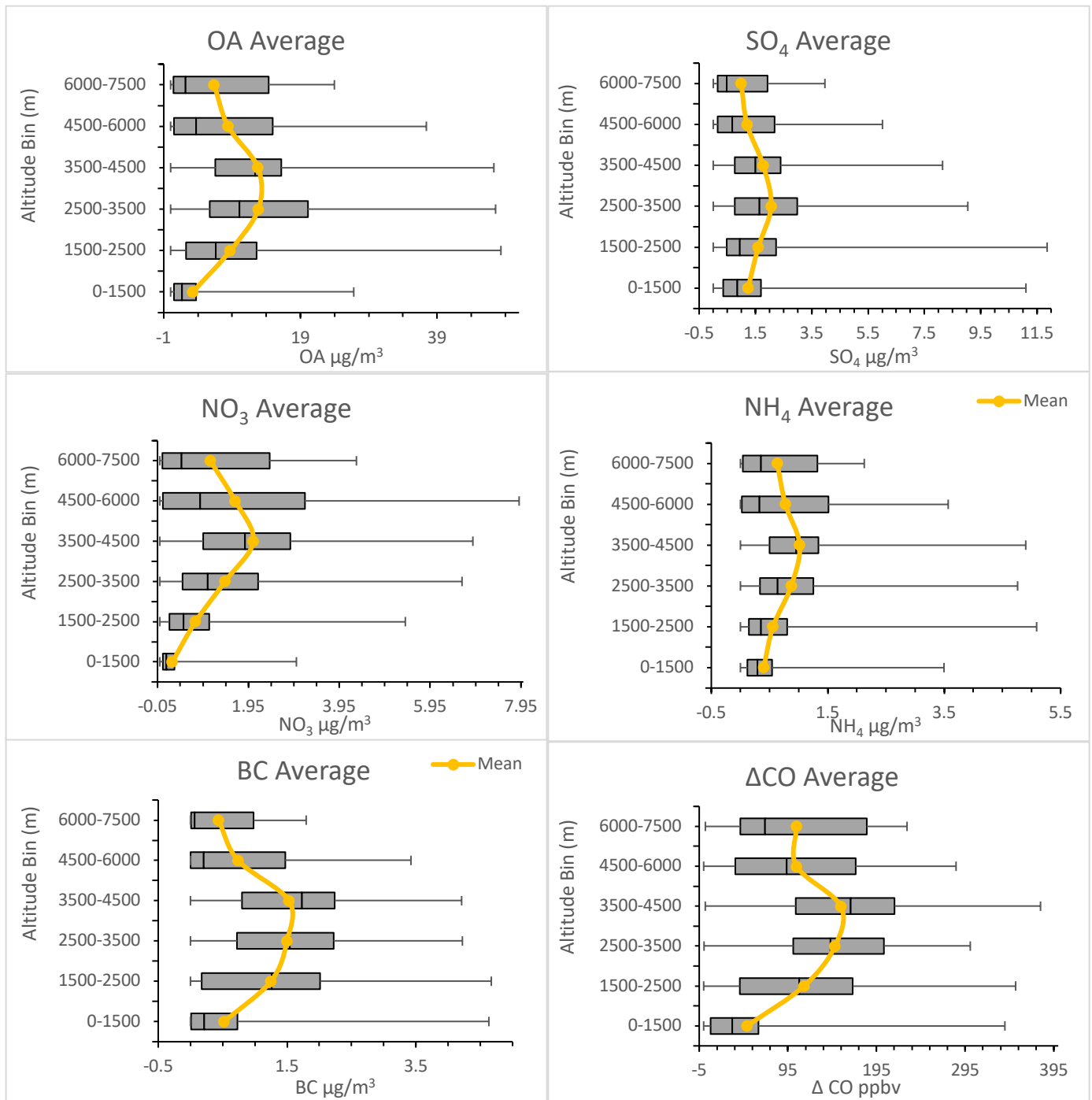


Figure 15. Box plots of Altitude and bulk species (ΔCO , BC, NO_3 , SO_4 , ORG, NH_4) to illustrate the vertical structure of the plume. Averaged data are from the entire 2016 campaign. The top of the box represents the 75th percentile, while the bottom of the box represents the 25th percentile. The upper whisker indicates the max value in the data set, while the bottom whisker is the minimum value in the data set. The solid line drawn in the box is the median value of the data, and the yellow marker indicates the mean value of the data.

One of the most noticeable chemical differences between the upper (3500m-5500m) and lower plume (1500m-3500m) was the ratio of NO_3 to OA. In the upper plume NO_3 :OA yielded a ratio of $\sim 1:6$. The lower plume ratio was $\sim 1:9$. Other chemical differences observed include the ratio between SO_4 and OA and between SO_4 and NH_4 . These relationships are the opposite of the NO_3 :OA relationship. The lower plume had a ratio of $\sim 1:5$ SO_4 :OA, while the upper plume had a ratio of $\sim 1:7$. ΔCO and BC followed the same trends as OA, but the concentrations of BC and CO dropped more rapidly than OA, NH_4 , SO_4 , NO_3 above 4500m. Between 4500m and 5500m ΔCO dropped 35% relative to ΔCO at 3500m-4500m. Black carbon followed that same trend. Black carbon dropped 48% over those same altitudes. However, OA, NH_4 , NO_3 , and SO_4 decreased less than 28%. Data for the ratios presented can be found in Table B.3 in Appendix B.

The vertical structure of the plume also varied by longitude and latitude. Across the study region, these altitude dependent trends between chemical species were surprisingly consistent. An altitude versus latitude plot for RF12 demonstrated how consistent the NO_3 :OA ratio was across an entire flight (Figure 16a). The red oval highlights the vertical profile that is shown in Figure 16b. The mass weight percent pie charts to illustrate the bulk chemical differences between the upper and lower plume are shown in Figures 16c and 16d. The trend shown in Figure 16a was consistent between flights regardless of the type of flight. Altitude versus latitude plots for all of the flights can be found in Appendix B, Figures 1-12. These plots provide a general depiction of the location of the plume on each flight of this study. Identically to Figure 16a, the markers are sized to OA, and then colored by the NO_3 :OA ratio to demonstrate the consistent layering between flights.

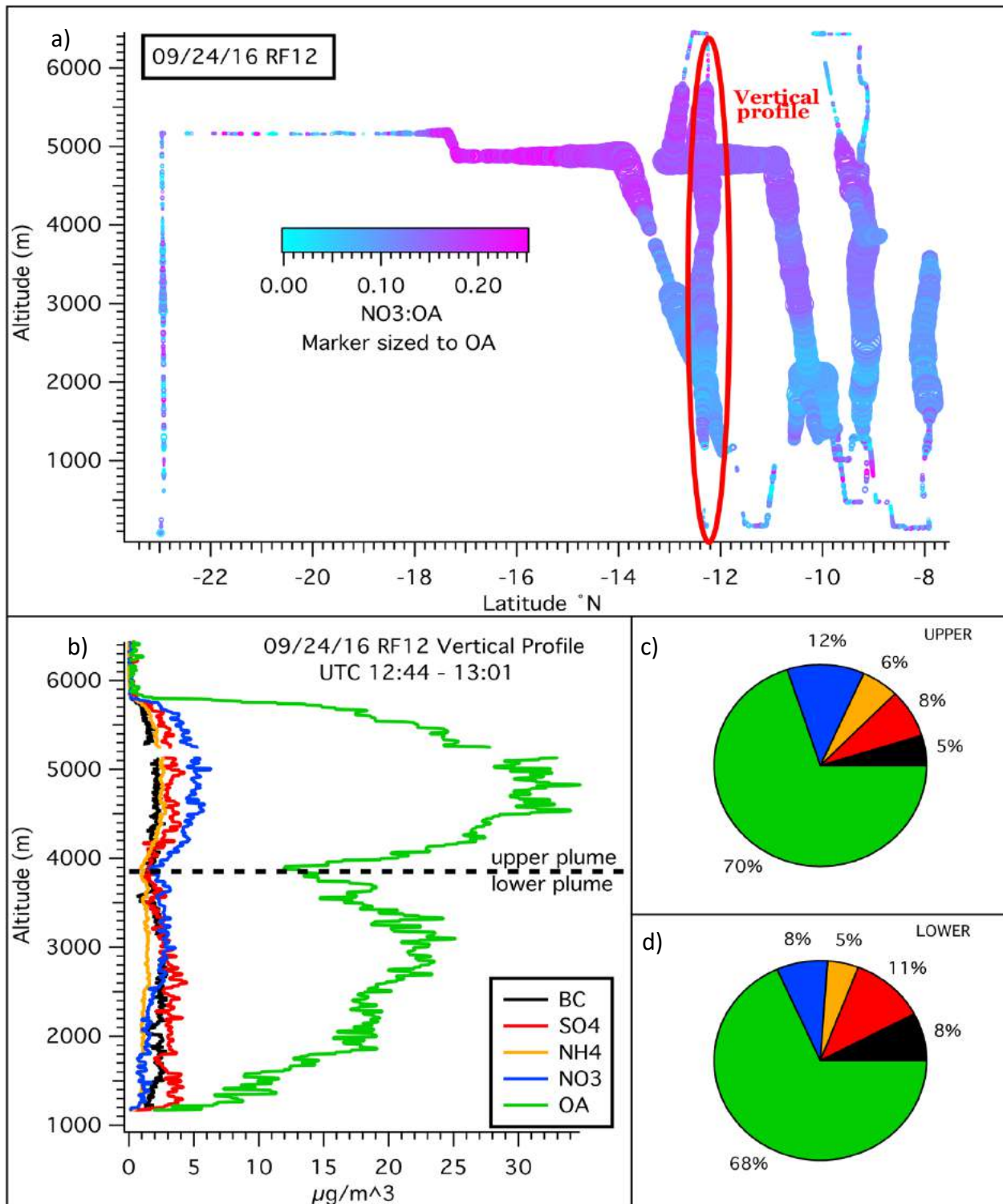


Figure 16 a) Plot of Altitude versus latitude illustrating where the plume was located spatially. The markers are sized to the concentration of OA. The markers are then colored by the NO₃:OA ratio to illustrate the upper and lower layers of the plume. The red oval indicates the data plotted for Figure 15b. **b)** vertical profile of the bulk chemical species. This plot illustrates the “gap” we often saw between plume layers. **Figures c and d** show the chemical differences found in this plume between the upper and lower layer. The most notable change is the NO₃ between the upper and lower layer, where the percentage shifts from 12% in the upper plume to 8% in the lower plume.

The plume also displayed changing aerosol characteristics as it was sampled between -23°N and -7.5°N . The way in which the TOO flights differed from the routine flights between these latitudes is shown in Figure 17 which displays the average concentration of OA with respect to latitude binned by altitude (0-7500m). As a rule of thumb, the TOO flights were the more eastern flights, while the routine flights were the more western flights. The location of the plume between 1500m and 5500m shifted more northerly during the eastern (TOO) flights, while the western (routine) flights encountered the plume further south (Figure 17). Between 1500m-5500m the highest OA mean concentrations were $8\text{-}20\mu\text{g}/\text{m}^3$ for the routine flights were located along 18° and 12°S . The highest mean OA concentrations were $10\text{-}25\mu\text{g}/\text{m}^3$ between 14° and 10°S . These features are due to the direction and strength of wind carrying the aerosol off the continent and over the SEA. The WRF-AAM forecast at 700hPa on 08/31/16 for winds (knots) and CO (ppb) in this region is shown in Figure 18. Because of the land based anti-cyclone over southern Africa, we usually observed the smoke coming off the West coast of Africa, traveling in a recirculating motion, carrying the aerosol west and south over the SEA and then back over the African continent (Zuidema et al., 2016). Therefore, the more western routine flights encountered the plume further south than the eastern TOO flights.

Overall, the plume structure described above was consistent from flight to flight. There were not substantial chemical differences between eastern flights versus western flights, nor were there strong chemical differences between northern and southern flights. The higher $\text{NO}_3\text{:OA}$ ratio in the upper layer, and a lower $\text{NO}_3\text{:OA}$ ratio in the

lower layer appeared in over 90% of the plumes that were analyzed (Appendix B, Figures 1-12)

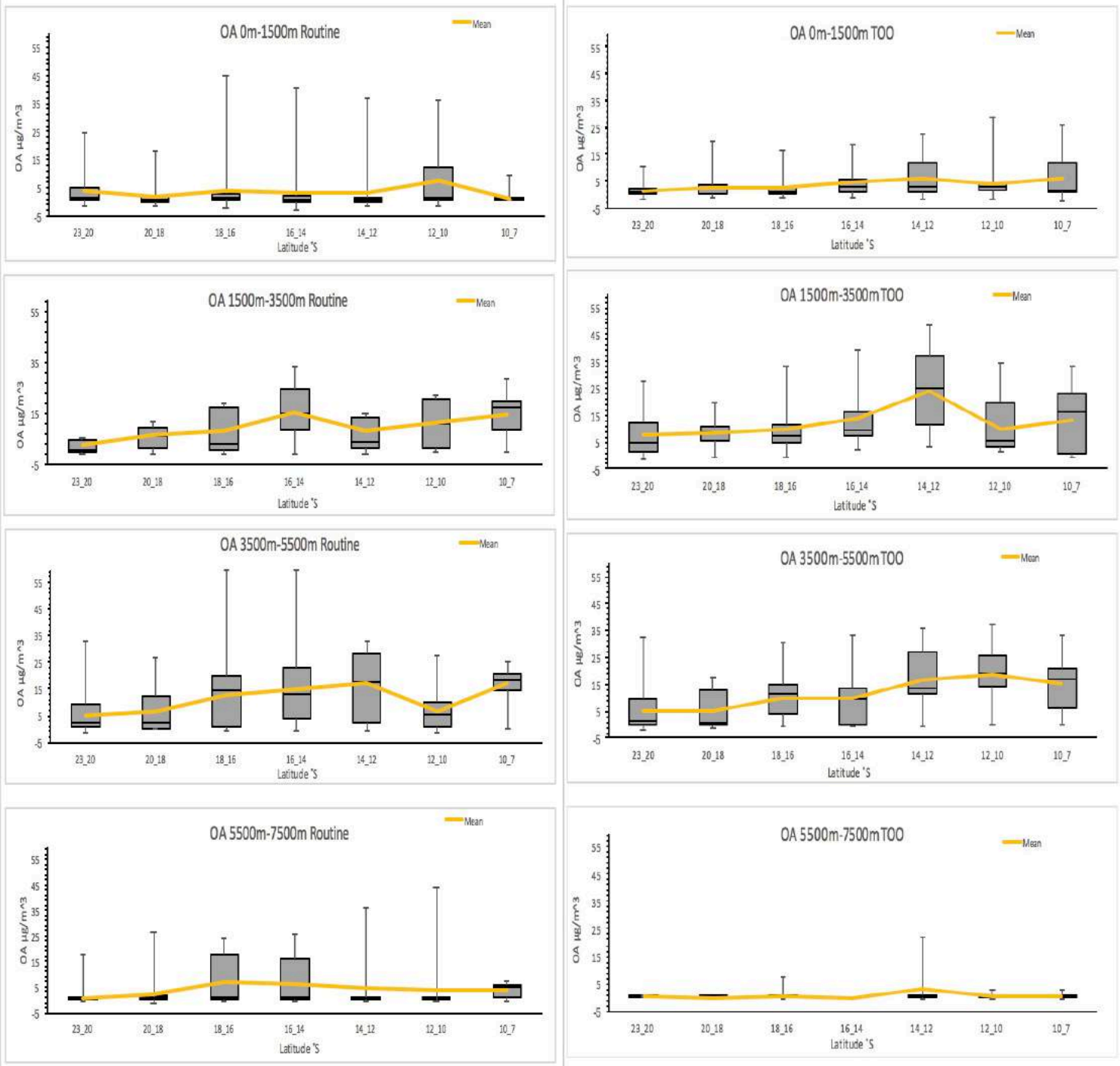


Figure 17. Box plots of Latitude and OA illustrate the location of the plume.

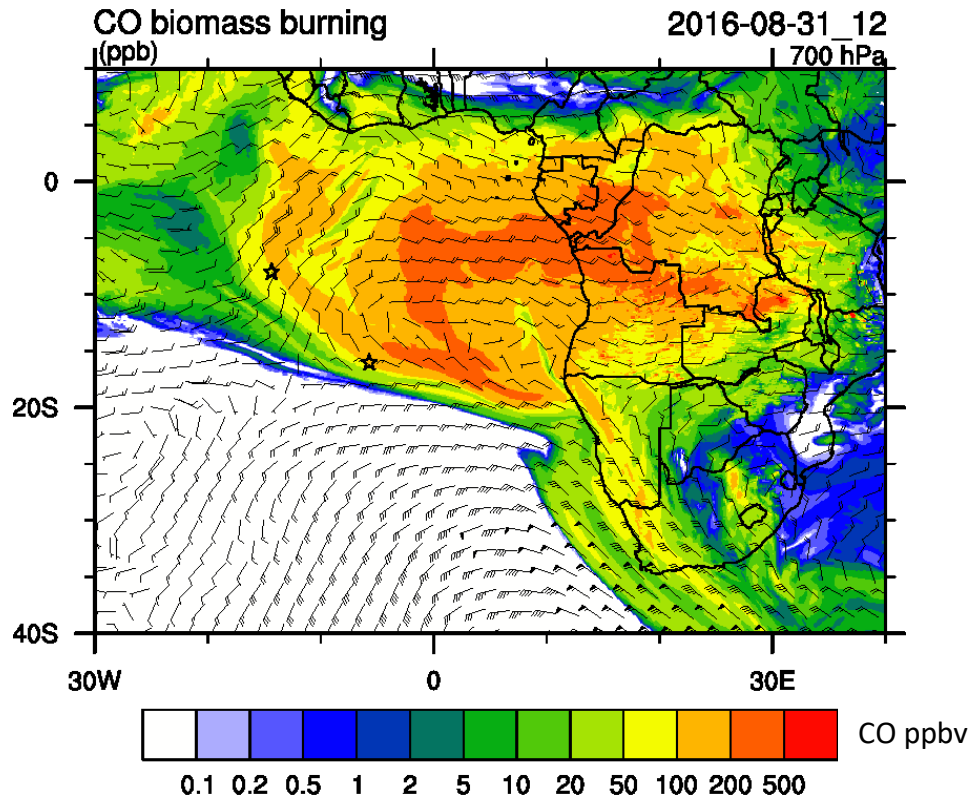


Figure 18. WRF-AAM CO (ppb) and wind forecast at 700mb vectors for RF02 (08/31/16). Color contour on map represents CO (ppbv).

Another observed structural characteristic of the plume we observed was aerosol touching cloud in ~60% of our profiles, while the other ~40% had at least a 100m gap between cloud top and plume bottom. As mentioned above in Section 1.1.5, aerosol cloud interactions are very important for semi-direct and indirect effects on marine Sc clouds. When aerosol comes into contact with clouds, there is the opportunity for aerosol to mix into the MBL. During the aerosol touching cloud interactions it was not uncommon to see BB pollution in the marine boundary layer. Elevated CO and BC in the MBL are much better tracers to use in the MBL instead of the tracers characterized by the AMS, such as OA and SO₄, because CO and BC are not produced by marine sources. OA and SO₄ cannot strictly be attributed to BB in the MBL because there is

organic matter and sulfate production from marine organisms. Due to the ionization efficiency of the AMS, we are unable to distinguish between OA and SO₄ production in BB and in marine sources. An example of aerosol right above cloud and a polluted MBL is shown in Appendix B, Figure 13. The height of the plume, along with its layering chemical features, were consistently observed at this height. There were some variations in gap location, plume top, and plume bottom all within a few hundred meters, when comparing individual flights and plumes.

Chapter 4. Discussion

In this chapter I will use standard high resolution data to describe organic aerosol (OA) characteristics. For this I will use work by Aiken et al. (2008), Cubison et al. (2011), and Kroll et al. (2012) to explain the differences and similarities between our African BB compared to other aerosols produced by BB. The variables f60, f44, O:C, and H:C used to interpret OA oxidation/aging processes are illustrated in Figure 19, OA aging parameters are summarized in Table 2. We can interpret from the aging parameters (f60, f44, OSc, OM:OC, O:C, and H:C), calculated with ORACLES OA data that the BB aerosol we observed is much more aged/oxidized than the aerosol Cubison et al. (2011), Kroll et al. (2012), and Aiken et al. (2008) observed. I will also compare ORACLES OA data, to a Weather Research Forecasting Chemical Model (WRF-Chem) to show how model observations and in situ data compare. This work with OA and modeled age tells us how we can use aging parameters, such as f44, to qualitatively track how OA changes with long exposure in the atmosphere. Observed chemical changes with age will then be applied to explain the structural changes we addressed in Chapter 3. Aside from the OA analysis, I will also describe the results of inorganic nitrate, ammonium, and sulfate acid base reactions. Using methods described by Zhang et al. (2014) with trace gases (CO and CO₂), I will discuss how source dependency does not appear to be a prominent characteristic of BB aerosol studied in this project. Lastly, this chapter will elaborate on the work done by Formenti et al. (2003), Haywood et al. (2003), and Sinha et al. (2003), to compare the results presented above with results from a previous study done in the same region, SAFARI 2000.

Table 2. Summary of BBOA age indicators described in Chapter 4.

BBOA Age Indicator	Aged (value of indicator)	Fresh (value of indicator)
H:C (Aiken et al., 2008)	1.5-1	1.5-2.5
O:C (Aiken et al., 2008)	0.6-1.2	0.25-0.6
Oxidation State (OSc) (Kroll et al., 2011)	0-(+1)	0-(-1)
OM:OC (Aiken et al., 2008)	2-3	1-2
f60 (Cubison et al., 2010)	0.003-0.01	0.01-0.05
f44 (Cubison et al., 2010)	0.15-0.28	0-0.15

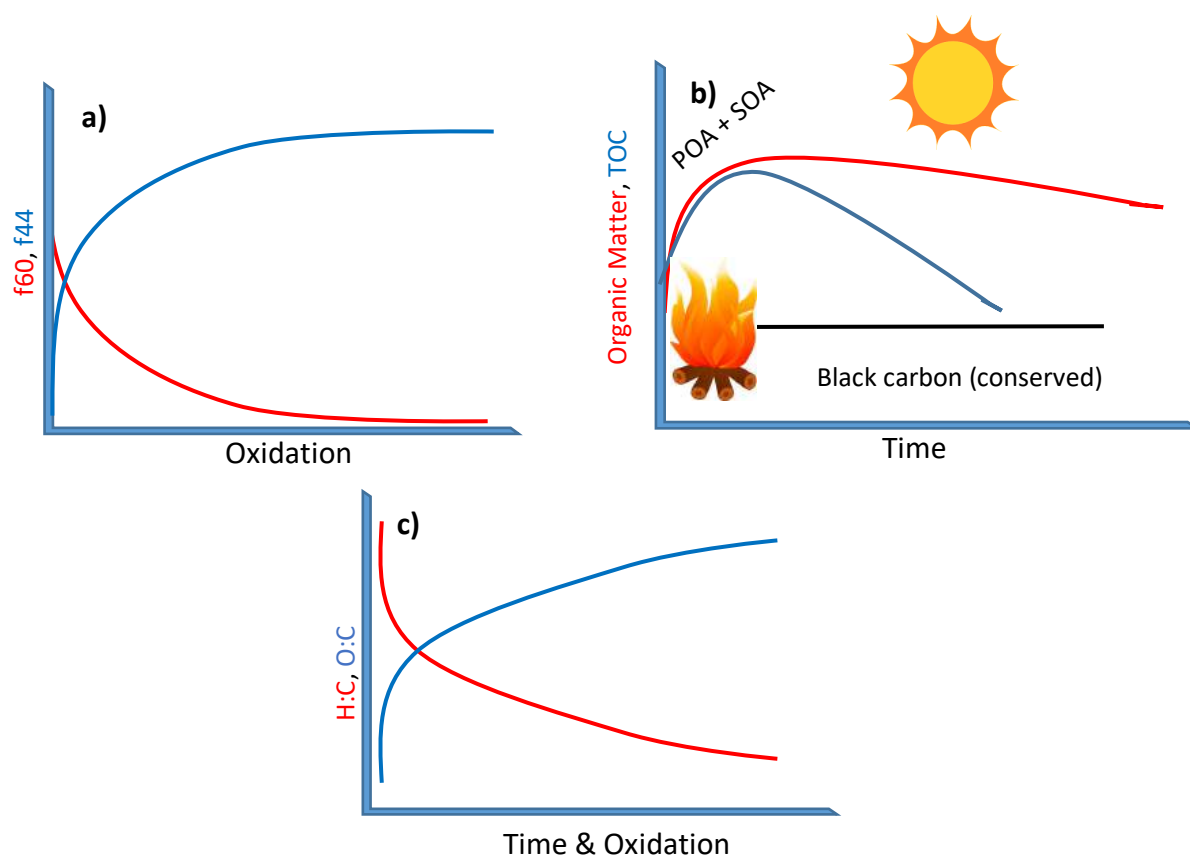


Figure 19. Effects of aging on OA, assuming no deposition losses **a)** The relationships of f44 (blue) and f60 (red) as oxidation occurs. Typically, f44 increases while f60 decreases. **b)** Schematic of how total organic carbon (blue), organic matter (red), and black carbon (black) react in the atmosphere. POA is formed from the fire and SOA is added as organic vapors oxidize and oligomerize. Eventually photooxidation reduces OA. TOC experiences loss faster than OM. Black carbon is conserved, assuming no washout is occurring. **c)** Schematically shows how H:C (red) and O:C (blue) react with time and oxidation. From an arbitrary starting point (based on source), H:C typically decreases as O:C increases, indicative of the aging processes.

4.1 Organic Aerosol

Using analysis techniques developed by Aiken et al. (2008) we are able to use high resolution AMS data from PIKA to plot organic aerosol results, on a Van Krevelen diagram. Van Krevelen diagrams allows us to cross plot the hydrogen to carbon ratio with the oxygen to carbon ratio (Aiken et al., 2008, Heald et al., 2010). The results of H:C versus O:C are typically characterized by a slope of -1. As aerosol volatilizes, oxidizes, and mixes in the atmosphere, the composition of hydrogen and oxygen change. As atmospheric aging or oxidation occurs, the H:C and O:C values move further down this slope from an arbitrary starting point. An example Van Krevelen diagram without data to illustrate the way in which reactions of organics affect the H:C and O:C values from an arbitrary starting point is illustrated in Figure 20a (Heald et al., 2010). The differences in O:C and H:C based on different starting materials is illustrated in Figure 20b. We expect BB starting material to be a combination of cellulose, levoglucosan, and lignin. These three starting materials are shown with black triangles in Figure 20b. O:C and H:C ratios on the Van Krevelen diagram do not account for nitrogen and sulfur containing compounds, we do not expect much influence on the O:C and H:C ratios from organic nitrogen and sulfur containing materials, because we believe these species are present in the inorganic form (see Section 4.6).

Previous AMS studies find high H:C and low O:C values indicate fresher, primary organic aerosol, while high values of O:C and low values of H:C are from aged, oxidized aerosol (Aiken et al., 2008). As aerosol oxidizes, it tends to lose two hydrogen molecules and gain an oxygen molecule. H rich aerosol typically indicates fresh OA, while O₂ rich aerosol indicates aged OA (Aiken et al., 2008, Heald et al., 2010).

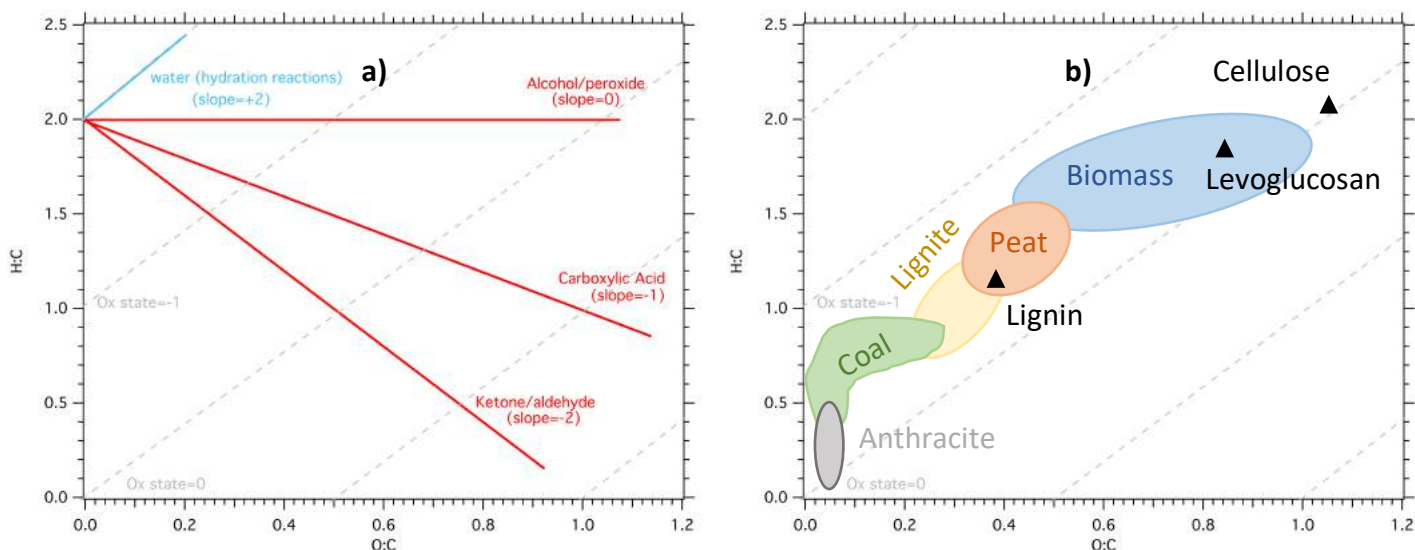


Figure 20. a) Van Krevelen diagram adapted from Aiken et al. (2008) and Heald et al. (2010). Red and blue lines represent the addition of a functional group. Dashed grey lines represent carbon oxidation state. **b)** Schematic Van Krevelen diagram fuels adapted from Van Loo and Koppejan (2007) illustrates where different types of fuels lie on the diagram. Fuels illustrated range from coal (grey, green, and yellow) to various types of biomass such as peat (orange) and the overarching blue circle represents other forms of biomass fuels.

AMS data from ORACLES 2016 (Figure 21) has been filtered to only include OA $> 12 \mu\text{g}/\text{m}^3$. This concentration ensures we are in the BB plume. The symbols on the graph are sized to indicate OA concentrations greater $12 \mu\text{g}/\text{m}^3$. What is immediately obvious is that there are two distinct groupings of flights. Research flights 2,4,7, and 11 (red) have lower O:C and H:C ratios, while the remaining flights (in blue: 3,5,6,8,9,10,12,13) have higher H:C and O:C ratios. An orthogonal distance regression (ODR) was used to calculate the slopes for the different groups. We found that the slopes are not significantly different. The differences in the H:C and O:C positions of the

two flight groups could be a result of different starting material (source), variability in fire conditions, or different aging processes.

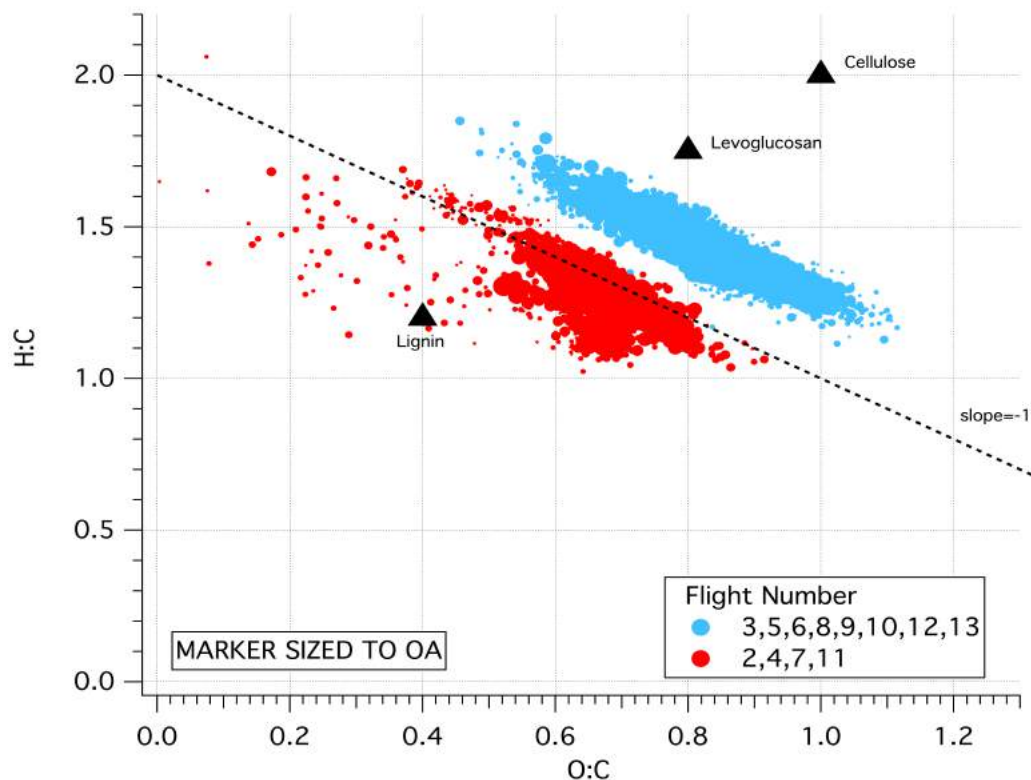


Figure 21. ORACLES 2016 Van Krevelen diagram for all flights. Two distinct flight groups (blue and red) lie between the expected starting materials, and slightly deviate from the -1 line.

The wide range of H:C and O:C ratios observed within the plume (Figure 21) are intriguing, it might indicate a range of ages or age differences within the plume. This range of ratios can also result from different burning conditions at the source. When burning occurs, not every particle released has experienced the same burning conditions. Some material may have been burned in a hotter region of the fire, or where oxygen was limited. We also notice that our two flight groups are in an intermediate position between the expected starting materials, meaning that our sources were most likely a combination of cellulose, levoglucosan, and lignin (Figure 20). Such a

discrepancy can be seen in the Van Krevelen Diagram. The variability of H:C versus O:C for each flight can be seen in Van Krevelen diagrams in Appendix C, Figures 1-12. In some flights a wide range of ratios are observed, while others, such as RF03, a very narrow range of H:C versus O:C is observed.

Figure 22 illustrates a variety of OA sources on the Van Krevelen diagram. Contrasting data from a number of laboratory and field studies from a number of different locations (Figure 22) allows us to compare ORACLES 2016 BB results with current studies. Data from LA urban pollution (SOAR-1) is represented in solid dark blue circles. Amazon BB(AMAZE-08) during the wet season is presented in light blue solid circles. A mixture of BB and urban pollution data from MILAGRO (2006) is present in red solid circles. The black, green, yellow, and purple diamonds are data points from various chamber (lab) studies. The blue and red lines superimposed on this graph represent the hearts of the two flight groups shown in Figure 21. The results from MILAGRO for aged OA sampled in the aircraft agree best with our O:C and H:C ratios. The tight clustering of data in Figure 22 illustrates that despite different methods, locations, and types of burned material, OA aging processes, as represented by the relationship between H:C and O:C do not appear to differ widely.

Heald et al. (2014) observed that data from laboratory and in situ studies typically exhibit a slope near -1 (Figure 22). Deviation from this line can result from different sources or starting material, burning conditions, and physical processes in the atmosphere. Another thing to note is that the data in Figure 22 falls on the $H:C=2-O:C$ line despite the wide range of sources. Evidently combustion and atmospheric processes have a strong tendency toward limited regions of the Van Krevelen Diagram.

The ORACLES OA data is consistent with an intermediately aged aerosol that is also consistent with oxidized organic aerosol. Although the data fall in two distinct flight groups, both only slightly deviate from the -1 line.

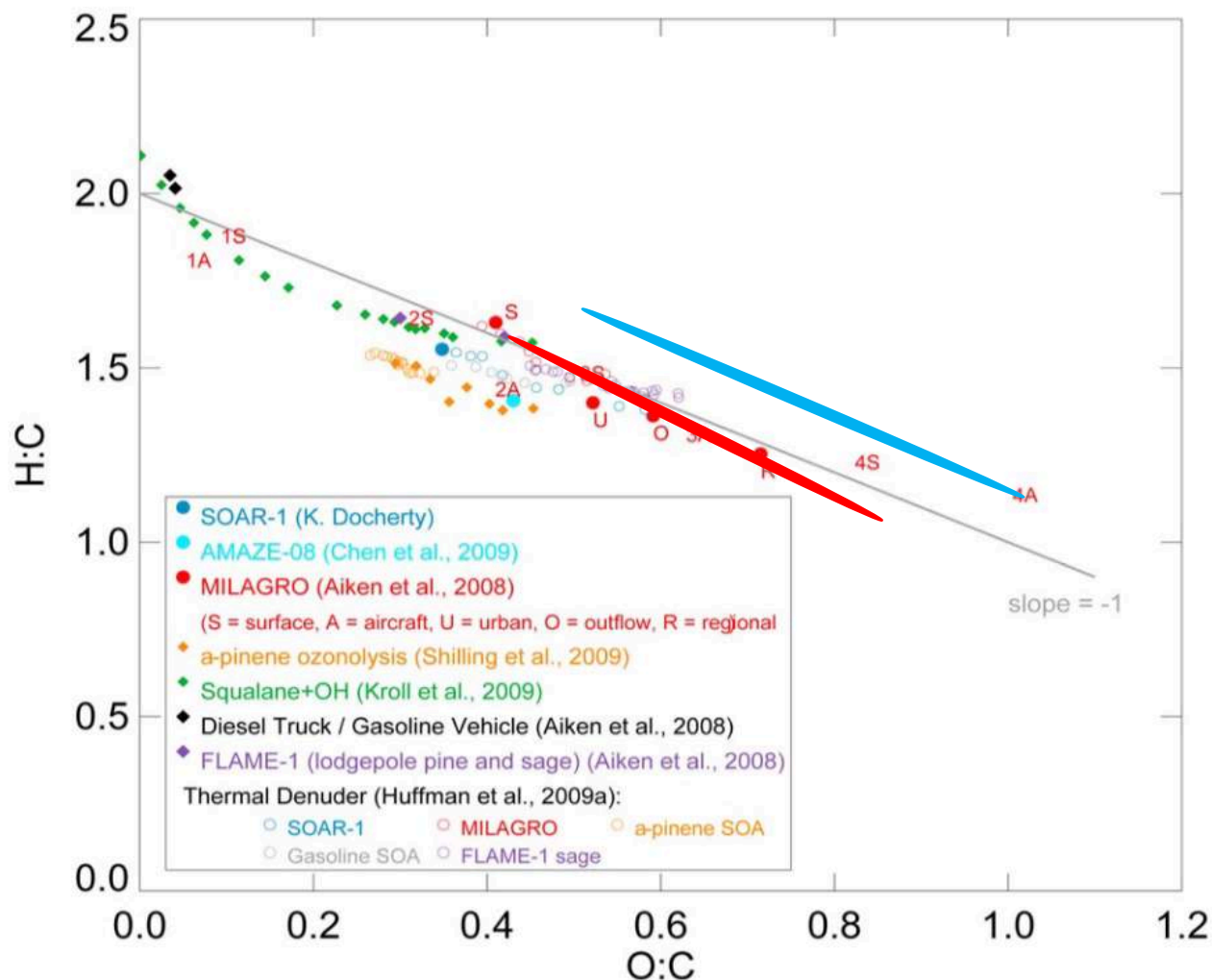


Figure 22. Van Krevelen diagram adapted from Heald et al., 2014. Solid circles indicate data from field studies, while diamonds represent data from laboratory studies. Open circles and open diamonds indicate thermal denuder experiments. Red and blue lines are meant to indicate where the heart of the ORACLES 2016 O:C and H:C would lie compared to other lab and field experiments.

Another method used to analyze the H:C and O:C data involves calculating oxidation state (OSc) (Kroll et al., 2011). The equation for OSc is given above in Section 1.2.1. Oxidation states calculated from a variety of BB studies are presented in Kroll et al. (2011). The reported OSc for each study can be found in Table 3, along with data from ORACLES 2016. The ORACLES 2016 data are also shown in Figure 23. Each circle in Figure 23 represents the average OSc for periods within each flight when OA > 12 $\mu\text{g}/\text{m}^3$, the colored dashed lines in Figure 23 represent various types of OA based upon ranges of OSc reported by Kroll et al. (2011) (Table 3). All results in the table were calculated using data from an HR-ToF-AMS. The wide range of oxidation states results from the variation in H:C and O:C ratios, as seen above in the Van Krevelen diagrams (Figure 21). These results further support our contention that ORACLES sampled an aged oxygenated aerosol plume. All flights observed aerosols that are more oxidized than the range of BB aerosol reported by Aiken et al. (2008). Our data indicates we are well into the aged regime, which implies long exposure in the atmosphere.

Table 3. Average oxidation state values reported for different studies and different aerosol types. Data from Table 3 is presented in Kroll et al. (2011).

Study / Type	Osc	Extent of Oxidation
Urban/Anthropogenic (Mexico City)	-1.6 to +0.1	N/A
(Amazonian rainforest)	-0.9 to -0.2	Fresh
Aged (Whistler Mountain)	-0.6 to +0.6	Oxidized
Hydrocarbon-like OA (HOA)	-1.7 to -1.6	Fresh
SVOOA	-0.5 to 0.0	Oxidized
LVOOA	+0.5 to +0.9	Extremely Oxidized
Vehicle exhaust	-2.0 to -1.9	N/A
BB(Aiken et al 2006)	-1.0 to -0.7	Moderately Oxidized
Alkane/Alkene (photo-oxidized aerosol)	-0.7 to -0.4	Oxidized
ORACLES 2016*	-1 to +0.41	Extremely Oxidized

*Not presented in Kroll et al. (2011)

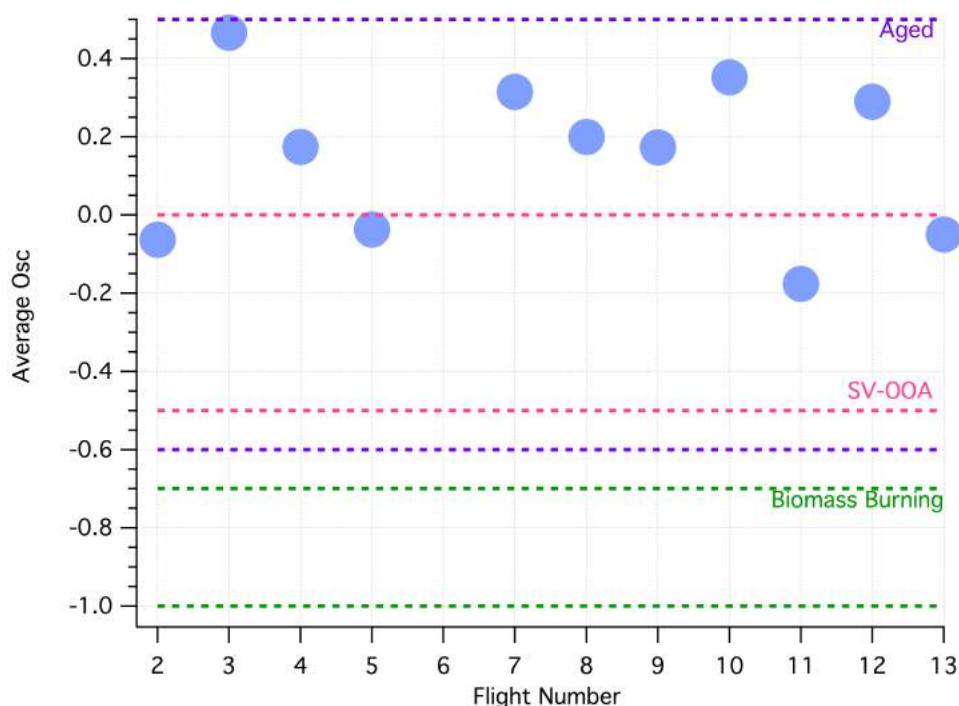


Figure 23. Average OSc for each flight during ORACLES 2016 for OA > 12 $\mu\text{g}/\text{m}^3$. Green lines indicate OSc range for biomass burning, pink lines represent SVOOA OSc range, and purple lines represent the OSc range for aged aerosol. The ranges of OSc listed are from Kroll et al. (2011). Average OSc data used to construct this figure can be found in Table C.1 in Appendix C.

One of the most prominent tracers of BB is the organic compound levoglucosan. Levoglucosan is formed during the pyrolysis of cellulose (Simoneit et al., 1998). Lee et al. (2010) found that the AMS peak at m/z 60 ($C_2H_4O_2$) is a fragment that results from the breakdown of levoglucosan and other anhydrosugars, including mannosan, galactosan, arabinosan, and xylosan. Lee et al. (2010) conclude $C_2H_4O_2$ is an even better indication of BB than levoglucosan itself.

Applying the high resolution data analysis and elemental analysis package for the AMS (Aiken et al., 2008), to ORACLES 2016 data revealed the concentration of $C_2H_4O_2$ was present at very low quantities, but was the dominating peak at m/z 60. For this report m/z 60, is considered equivalent to $C_2H_4O_2$. This fragment is usually found to be 3 to 5% of the total organic aerosol concentration in freshly emitted BB (Aiken et al. 2008, Cubison et al., 2011). As aerosol ages in the atmosphere, $C_2H_4O_2$ decreases. The amount of $C_2H_4O_2$ is also dependent on the type of fire and burning process (Collier et al., 2014). For example, smoldering fires release relatively higher amounts of m/z 60 (Collier et al., 2014; Jolleys et al., 2014; Zhou et al., 2018)

Another way to look at the m/z data is to plot the parameter f_{60} , which is the ratio of m/z 60 to OA, versus the parameter f_{44} , the ratio of m/z 44 as a function to OA. The presence of f_{44} typically indicates carboxylic acid groups, while f_{60} mainly indicates $C_2H_4O_2$. Higher fractions of f_{44} and lower fractions of f_{60} are characteristic of more oxidized organic aerosol. f_{60} of non-BB plumes is typically $\sim 0.3\% \pm 0.06\%$ (Cubison et al., 2011). Cubison et al. (2011) present these results for a number of field measurements (Figure 24). This figure illustrates the contrast between fresh, less

oxidized BBOA and highly oxidized BBOA. The data in the upper left corner (green and yellow symbols) with values of f_{44} between 0.15 and 0.24 and f_{60} values less than 0.01, are from long range transport of Siberian biomass burning. As one can see, this

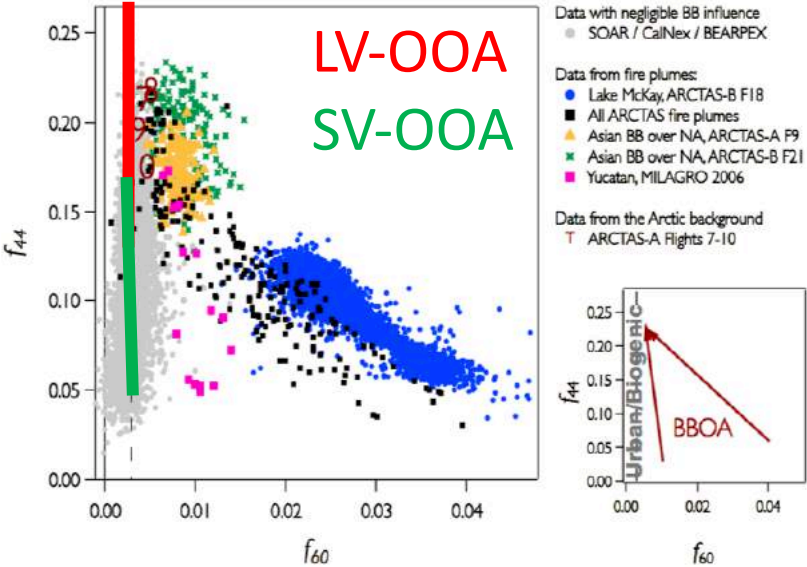


Figure 24. The relationship of f_{44} vs f_{60} from a number of aerosol studies. As aerosol undergoes photo-oxidation the value of f_{44} is expected to increase while f_{60} is expected to decrease. Adapted from Cubison et al. (2011).

aerosol has a very high f_{44} , and very low f_{60} . The data points in blue are from freshly emitted wild fires from the ARCTAS campaign. This aerosol has a much lower f_{44} and higher f_{60} . Fresh BBOA data points in pink from the Yucatan peninsula follow this trend, showing lower values of f_{44} , but also low

values of f_{60} . We observe a similar pattern for ORACLES 2016 data in Figure 25b.

Cubison et al. (2011) also highlight aerosol with f_{44} values over 0.15 can be categorized as LV-OOA, and values below 0.15 are categorized as SV-OOA. A value of 0.27 for f_{44} seems to be the upper limit for BBOA and non BB organic aerosol. Pure oxalic acid, essentially the most oxidized organic compound in aerosol show that the maximum value for f_{44} is actually 0.34. As far as ORACLES data and the data from Cubison et al. (2011) show the upper limit does not exceed 0.27. The inset figure in the bottom right of Figure 24 shows how f_{44} and f_{60} can also be used to interpret whether or not the aerosol is biogenic or urban based on the f_{44} values.

A plot of ORACLES 2016 f44 vs f60 for RF05 (09/06/2016) is shown in Figure 25a. Plots for each flight can be found in Appendix C, Figures 13-24. The data is filtered to include only values of f44 and f60 that have concentrations of OA greater than $12\mu\text{g}/\text{m}^3$. The symbols are then sized to $\text{OA} > 12\mu\text{g}/\text{m}^3$. The average f44 versus f60 values for each flight is shown in Figure 25b. In flight RF05 we mostly observe high f44 values (> 0.18) and low f60 values (< 0.012). These results are consistent with aged oxidized OA as in Cubison et al. (2011). Although Figure 25a only presents data from one flight, the other flights during the campaign displayed a similar pattern. The plots in Appendix C show how little variability there was in the range of f44 and f60 for the entire campaign. The data presented in Figure 25b can be found in Table C.2 in Appendix C. The flight to flight average of f44 and f60 values presented in Figure 25b fall within in the upper limits of f44 with low f60 values. These values of $\text{f44} > 0.15$ and $\text{f60} < 0.01$ indicate that the BB aerosol sampled in ORACLES 2016 is mostly oxidized BBOA. Despite slight differences between flights, Figure 25b shows that the BB studied in ORACLES agrees with observations from Cubison et al. (2010) for biogenic, low volatility oxygenated organic aerosol (Figure 24).

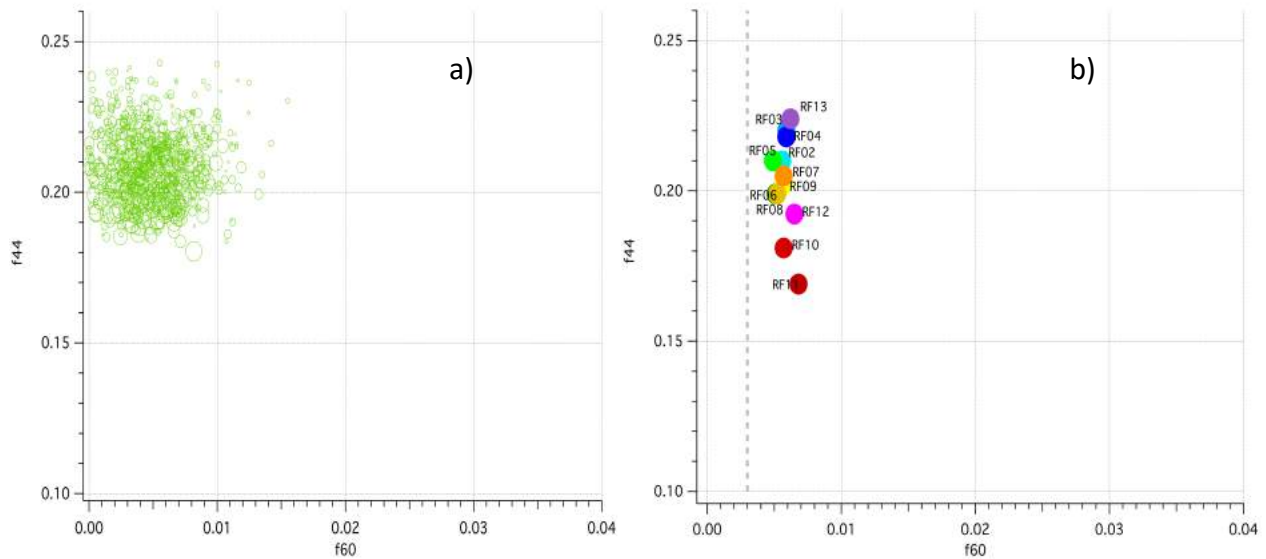


Figure 25 a.) f44 vs f60 for RF05 09/06/16 including OA > 12 $\mu\text{g}/\text{m}^3$ **b.)** ORACLES data from all flights. Data clusters in top left corner of graph indicating aged, oxidized aerosol. Grey dashed line indicates f60 observed in urban, non-biomass burning aerosol (Cubison et al., 2011).

4.2 Other Chemical Tracers of Biomass Burning

Aside from chemical tracers analyzed with the AMS, we can look at BC, CO and CO₂ to help us identify pollution sources and pathways through the troposphere, as well as burning efficiency. CO and CO₂ can be used to calculate the modified combustion efficiency (MCE). The MCE is a unitless molar ratio defined as $\text{MCE} = \Delta\text{CO}_2 / (\Delta\text{CO} + \Delta\text{CO}_2)$ where ΔCO and ΔCO_2 are measured concentrations of these species relative to background concentrations. The relationship between emitted OA from smoldering and flaming fires and MCE is presented schematically in Figure 26 (Collier et al., 2014). MCE increases as fire type shifts from high emission smoldering fires towards low emission flaming fires. An MCE below 0.9 is indicative of smoldering fires, while an

MCE above 0.9 indicates flaming fire conditions. Throughout the campaign we observed MCEs between 0.97 and 1, suggesting that we observed aerosol that derived from very efficient flaming fires for the entirety of the campaign. The average MCE observed per

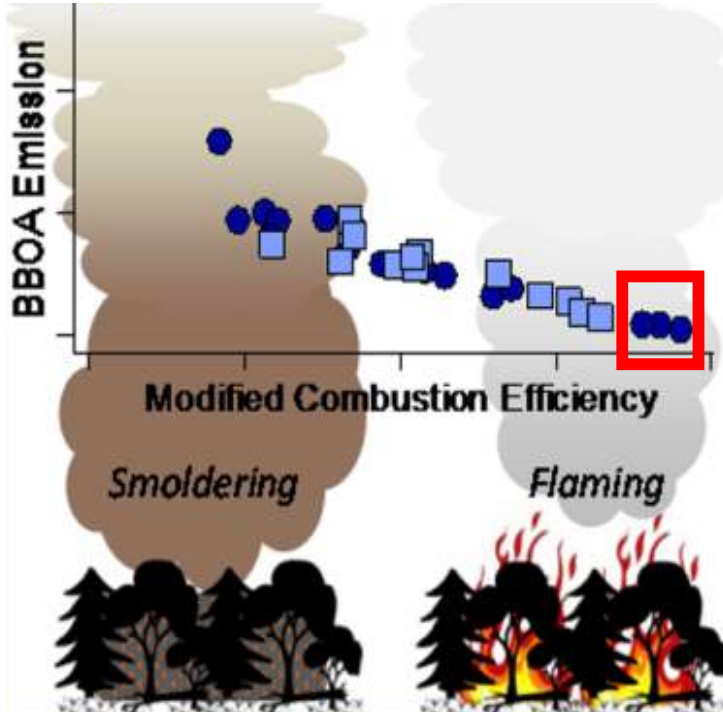


Figure 26. Illustration from Collier et al. (2014) modified to show approximately where ORACLES 2016 data lie (red box) .

each flight for OA > 12µg/m³ is summarized in Table D.1 in Appendix D. Care must be taken when using ΔCO and ΔCO₂, because we did not fly upwind of the fires to measure background values. Instead we estimated background values as follows. The background average adopted for CO is 65 ppbv and for CO₂ is 397 ppmv.

These values were observed at free troposphere altitudes above the plume (~7000m). Collier et al. (2014) provide a modified equation to calculate MCE if background values are not known. The modified equation $MCE = 1 / (1 + dCO / dCO_2)$ allowed us to find a linear relationship between CO and CO₂ where the slope is dCO / dCO₂, and the intercept represents the background value. We did this analysis for several plumes, and the results agreed well with our assumed values. This analysis suggests that variations in background CO and CO₂ were small compared with the observed enhancements in the observed plume, so the errors in calculating MCE are correspondingly small, even though background concentrations are estimated only.

CO and CO₂ can also be used as chemical tracers because they are preserved throughout atmospheric processing. CO has a lifetime of over 30 days in the atmosphere. Plotting CO versus other tracers, such as OA or BC, can provide information on source because the ratios of CO with OA and BC depend both on sources, and how the sources are being burned (efficiently or inefficiently). The relationship between CO and BC for target of opportunity flights and routine flights is shown in Figures 27a and 27b. As mentioned before, black carbon is also valuable as a tracer, because while CO and CO₂ are very robust BB tracers that are preserved through almost any atmospheric process, BC is a better tracer for BB aerosol. Because it is an aerosol, it shares the same physical loss mechanisms (wash out) as the rest of the BB aerosol tracers.

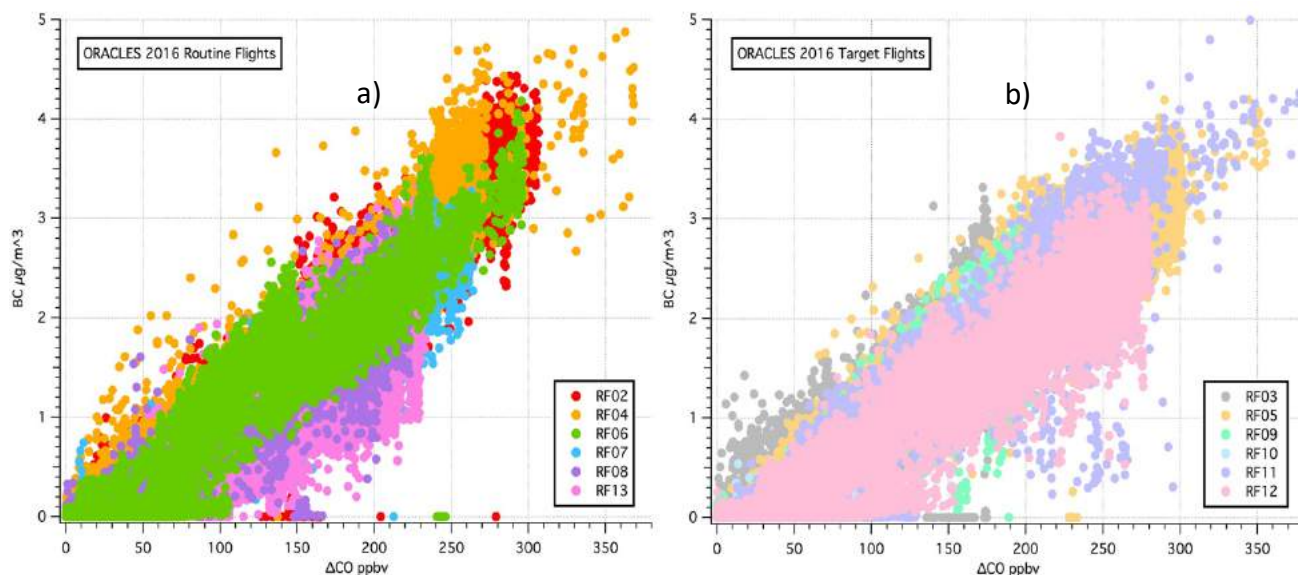


Figure 27. a) BC $\mu\text{g}/\text{m}^3$ vs $\Delta\text{CO}(\text{ppbv})$ for the routine flights. Markers are colored by flight number. **b)** rBC $\mu\text{g}/\text{m}^3$ vs $\Delta\text{CO}(\text{ppbv})$ for the target of opportunity flights. Markers are colored by flight number.

The consistency of the slopes/ratios between black carbon and CO indicate that there were little to no significant source differences in aerosol sampled in ORACLES 2016, nor were there significant removal processes. This is not particularly surprising

given the nearly uniform high MCE and the lack of rain during the dry season, when the ORACLES campaign was conducted. These observations run counter to expectations that different fuels might have affected the ratio. Slopes ranged between 0.0097 and 0.0134 on different flights and can be found in Table D.2 in Appendix D.

Plotting CO versus OA can also provide insight into source variation, and can potentially reveal changes in composition as the aerosol ages. The ratio between $\Delta\text{OA}/\Delta\text{CO}$ is known as an enhancement ratio (ER). ER is usually presented in terms of $\Delta\text{X}/\Delta\text{CO}$, which allows compounds from individual sources (ΔX) to be fingerprinted by unique ratios to their reference tracer (Formenti et al., 2003). Plots of OA versus ΔCO (Figure 28) show a little more variation between flights compared to plots of BC versus CO (Figure 27), indicating that there may be chemical changes occurring in the OA. It also appears that routine flights have a higher OA:CO ratio than most of the TOO flights. The slopes for these plots can be found in Appendix D in Table D.3. These plots of BC versus OA can also show differences between source or atmospheric processes. Plots of OA versus BC (Figure 29) illustrate that there is some variation between flights, which is most likely attributed to changes in OA. The BC:OA relationship for each flight can be found in Appendix D, Table D.4.

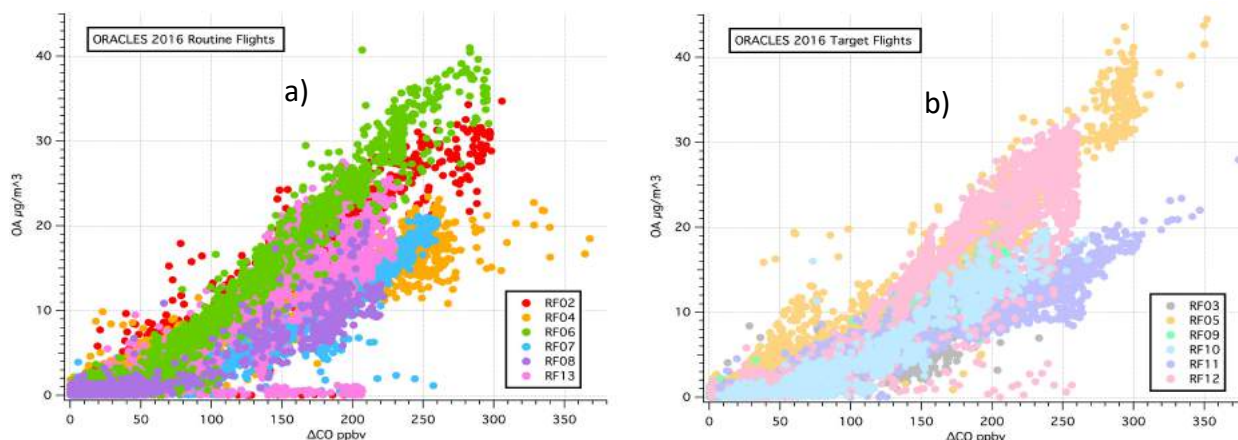


Figure 28. a) OA $\mu\text{g}/\text{m}^3$ vs ΔCO (ppbv) for routine flights. number. **b)** OA $\mu\text{g}/\text{m}^3$ vs ΔCO (ppbv) for TOO flights. Symbols are colored by flight number.

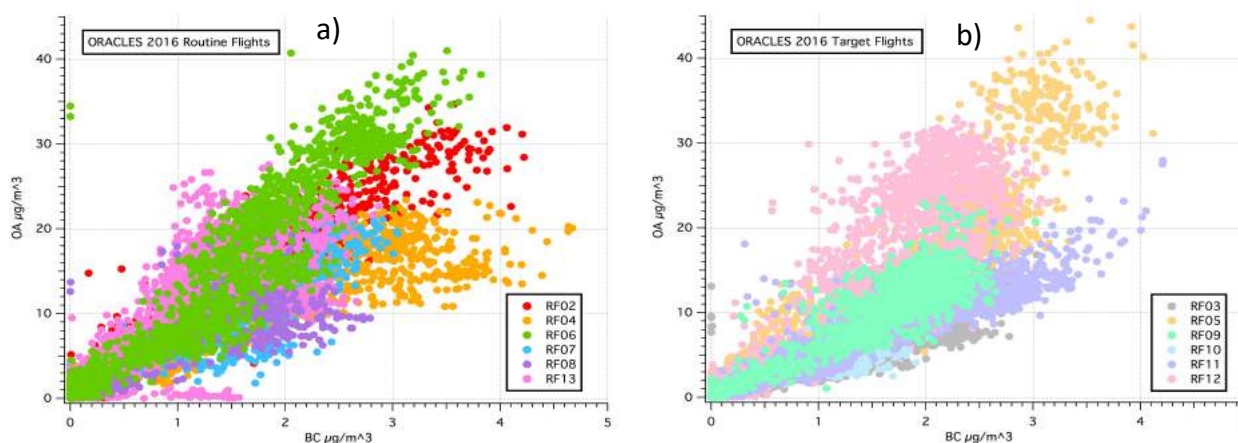


Figure 29. a) OA ($\mu\text{g}/\text{m}^3$) versus BC ($\mu\text{g}/\text{m}^3$) for routine flights and TOO flights. **b)** OA ($\mu\text{g}/\text{m}^3$) versus BC ($\mu\text{g}/\text{m}^3$) for TOO flights. Symbols are colored by flight number.

4.3 Aerosol acid/base balance

Ammonia plays a unique role in the troposphere. It is the only common base (carbonates in dust and the weak alkalinity of seawater are the main exceptions), and it has a very high vapor pressure. This means that aerosols are essentially never alkaline. If the pH rises, the equilibrium $\text{NH}_3 + \text{H}_2\text{O} \rightleftharpoons \text{NH}_4^+ + \text{OH}^-$ shifts to the left, and NH_3 evaporates. If there are acids present, NH_3 diffuses into them to form salts.

There are many more acids present in the troposphere, the most important of which are sulfuric, nitric, and various carboxylic acids. In a manner analogous to ammonia, if aerosols become too acidic, volatile acids can be driven into the gas phase. Since nitric acid is relatively weak and volatile, NO_3^- cannot exist in particles with insufficient ammonium to neutralize sulfate. The same is true of volatile carboxylates such as formate and acetate, which are found only on weakly acidic particles. Less volatile carboxylates can remain in their acid form on acidic particles.

The BB plume in ORACLES 2016 had two distinct layers (see Section 3.1). The upper layer had higher a $\text{NO}_3:\text{OA}$ ratio and a lower $\text{SO}_4:\text{OA}$ ratio, relative to the plume, which had a higher $\text{SO}_4:\text{OA}$ ratio and a lower $\text{NO}_3:\text{OA}$ ratio. In the upper and lower plume the $\text{NH}_4:\text{OA}$ ratio remained fairly constant. We can use the acid/base balance to explain some of these trends. We are able to calculate molar ratios with NH_4 , SO_4 , and NO_3 to provide insight into the chemical changes that are occurring between plume layers.

Aerosol is almost never basic, and NH_4^+ is the only significant base. So, when plotting molar equivalents of acids against bases (Figure 30) all points ought to be below the 1:1 line. This fails spectacularly when NO_3^- is neglected (shown in blue markers), indicating that there is often enough NH_4^+ to neutralize all of the SO_4^{2-} , as well as some nitric acid. Since we did not measure carboxylic acids, they could not be included. If there were significant quantities of any unmeasured acids neutralized by NH_4 , they would appear on these plots as points above the 1:1 line. Flights 4,7,9,11,13 have some values above the 1:1 line, indicating some carboxylic acid has been

neutralized by NH_4 . The plots of NH_4 versus ($2 \cdot \text{SO}_4 + \text{NO}_3$) for the entire campaign can be found in Appendix E, Figures 1-12.

Lacking measurements of vapor phase acids (nitric and some carboxylic acids), we cannot establish whether the upper and lower plumes have different total nitrate or carboxylate concentrations. The lower plume must have had either more SO_2 in the source fires, SO_2 from cities or power plants, or more of the SO_2 had time to oxidize to H_2SO_4 . This was one of the first indications of age differences between the upper and lower plume. The lower plume, having more time for SO_2 to react, could indicate that it has spent more time in the atmosphere undergoing oxidation, while the upper plume is younger, thus not having enough time to oxidize more SO_2 .

It should be noted that we are presenting the NH_4 , SO_4 , and NO_3 reactions for aerosol in the free troposphere (above 1500m). In a clean MBL, the aerosol is much more acidic because there is so much sulfuric acid production via DMS, and very little nitrate and ammonia sources to balance this reaction.

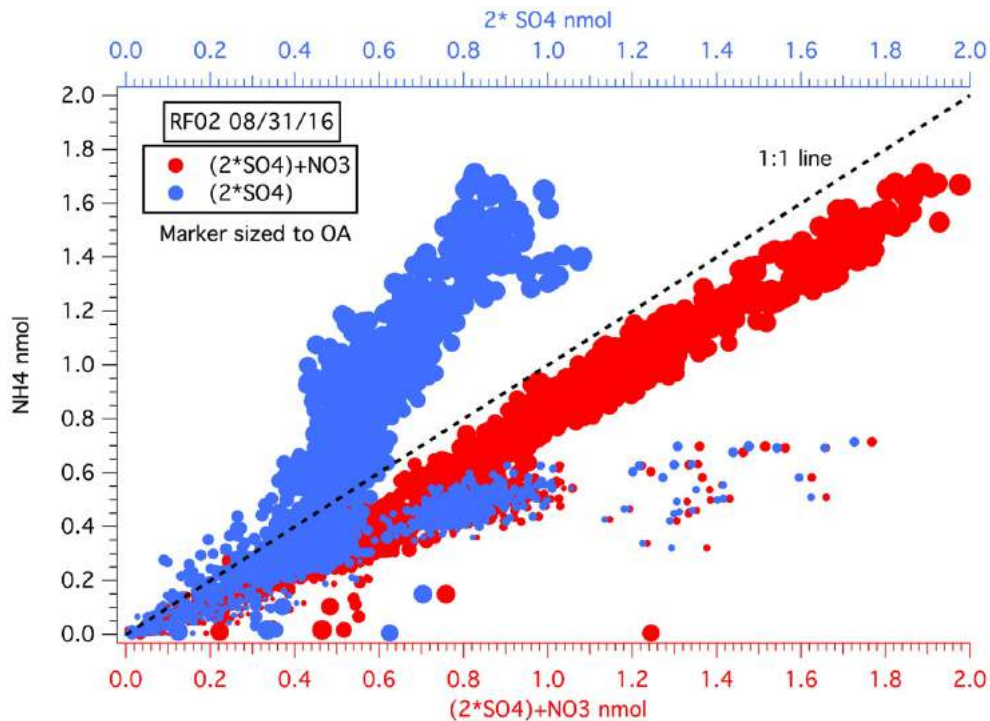


Figure 30. Molar ratio plot of NH_4 (y-axis) versus $(2 \cdot \text{SO}_4 + \text{NO}_3)$ (bottom x-axis) in red, and $2 \cdot \text{SO}_4$ in blue (top x-axis). The dashed 1:1 line indicates a neutral aerosol.

4.4 Back Trajectories and Modeling Observations.

Seven-day Air Mass Back Trajectories (AMBTs) for ORACLES 2016 were performed using the National Oceanic and Atmospheric Administration's (NOAA) Hybrid Single-Particle Lagrangian Integrated Trajectory (HYSPLIT) model (Draxler et al., 1993, 2003, Stein et al., 2015). The model is available to the public via <http://www.arl.noaa.gov/ready/hysplit4.html>. Using methods from Freitag et al. (2104), we ran the trajectories with Global Data Assimilation System (GDAS) 0.5° data every 10 seconds along the flight path for up to -168 hours. Running thousands of trajectories grouped together gives us confidence in the accuracy of the trajectory path when groups of trajectories follow similar patterns. When a consistent pattern between nearby trajectories is observed in the absence of convection, it is likely that the trajectories are

reliable. Trajectories are unreliable when extensive mixing happens, however, nor are they are not trustworthy for boundary layer or convective systems. For more information about errors and assumptions associated with AMBT modeled data versus in situ aircraft data see Freitag et al. (2014).

These trajectories indicate that the aerosol did not originate one specific region in Africa. The trajectories indicate that the smoke is coming from a variety of regions, and spending days over the African continent, before being lofted over the SEA. The consistency in the AMS data and other chemical tracers (CO, CO₂, and BC) described previously, supports the idea of uniform plume being transported of the SEA. The absence of a specific relationship between chemical signature and flight type, location, or time, supports the idea that the BB represents a mixture of aerosol originating from multiple locations. Seven day back trajectories from flight RF05 (09/06/2016) (Figure 31a) shows that fires from a wide range of south African regions could have influenced the air we sampled. The calculated trajectories pass over the Gabon region, the Angola region, and the Mozambique region. The chemical analysis of aerosol sampled during this flight was relatively uniform with respect to the chemical tracers that would indicate different burning regions. A MODIS fire image from 09/06/16 (RF05) shows the number of accumulated fires within 24 hours (Figure 31b). Because the AMBT show the aerosol tracing back to multiple locations within the region, and in such a slow manner, we can confidently say that we are not seeing a single source fire in the aerosol analyzed during any of our flights. The air is retained for a sufficiently long time over land that amasses BB aerosol from hundreds of fires.

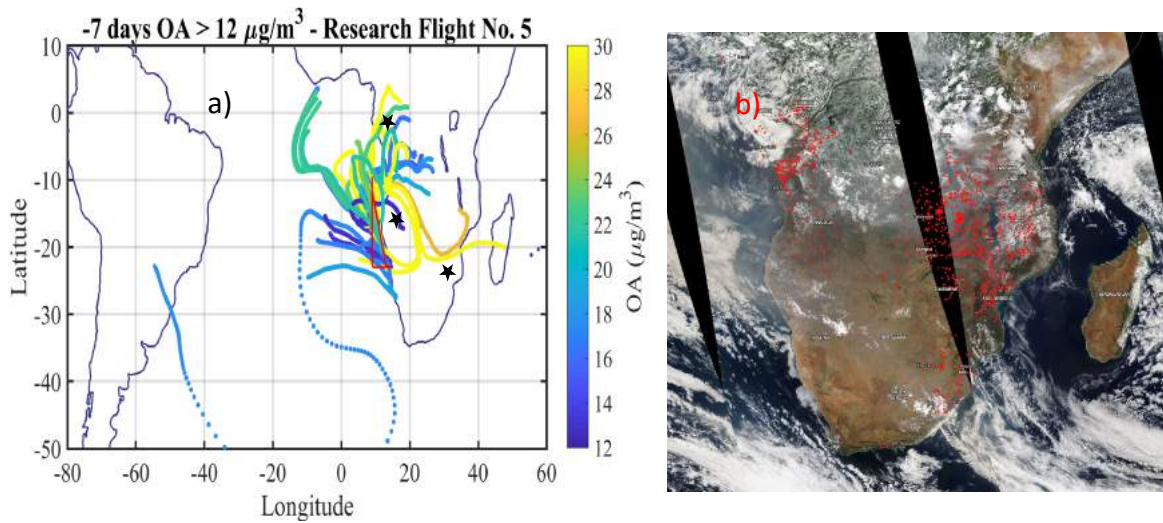


Figure 31 a) Back trajectories for RF05 (09/06/16). The trajectories were done every 10 seconds along the flight path. Only every tenth trajectory is plotted here. The trajectories are colored by the OA concentration observed in plume for $OA > 12 \mu\text{g}/\text{m}^3$. Stars indicate Gabon, Angola, and Mozambique regions **b)** 5km resolution Modis fire image for 09/06/16. Red dots indicate fire detected within a 24-hour period (<https://worldview.earthdata.nasa.gov/>).

The HYSPLIT data also includes mixed layer depth, so we show plotted back trajectories with the mixed layer depth (continental and marine) in Figure 32. Five trajectories at different altitudes (1000m, 2000m, 3000m, 4000m, 5000m) from RF12 can be used to illustrate how the air masses traveled over the continent. The first symbol indicates the aerosol that was sampled by the P-3B on 09/24/12. Each subsequent symbol represents a one-day trajectory path. The mixed layer depth is shown in grey. The continental mixed layer is present from 09/18/16 through 09/23/16. On 09/23/16 the air masses are lofted over the SEA, where the height of the marine mixed layer depth is significantly lower than that over the continent. It appears that the lower altitude (1000m-3000m) air masses have been influenced by the continental boundary layer over a 5-day period. The continental boundary layer increases in height

each day, indicating stronger convection. The intersection of the lower plume layer (~1000m-3000m) with the continental mixed layer implies that it is injected with BB aerosol for multiple days over the continent. In contrast, the upper plume (4000m-5000m) experienced injection only on the last day before the air was carried over the SEA. This implies that the upper layer of the plume is actually younger in age because it has been influenced by BB only on the last day over land perhaps by the strongest convection. Whereas the lower plume amassed BB aerosol for 4-5 days. These are difficult claims to confirm due to uncertainties associated with HYSPLIT modeling (Freitag et al., 2014).

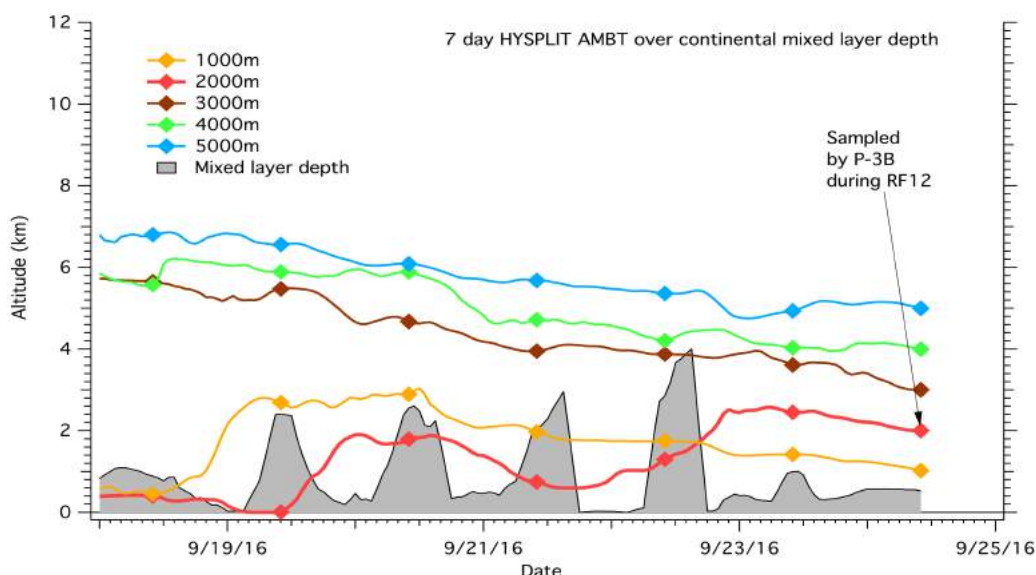


Figure 32. Seven-day HYSPLIT AMBT and mixed layer depth. Each symbol is representative of 1 day trajectories. Symbols start on RF12 09/24/16. The lower plume (orange, red, and maroon) interact with the mixed layer depth for five days, whereas the higher plume (blue and green) do not interact with the mixed layer until 1 day prior to being carried over the SEA.

We noticed these aerosol aging patterns using the Weather Research and Forecasting Chemical model (WRF-Chem), which simulates emission, turbulent mixing, transport, transformation, and fate of trace gases and aerosols. The modeling capabilities of WRF-Chem include, but are not limited to, photochemistry, particulate

matter, optical properties, radiative forcing, aerosol radiation and cloud chemistry feedback, and aerosol cloud interactions (Grell et al., 2005; Wang et al., 2015). Aerosol age (days) models are calculated by using 15 tracers, each tagged to one day of BB emissions. We observed variation in f44 along flight paths, sometimes up to a 6% change (Figure 33). We did not witness these changes with f60. In half of the flights, we observed a small dependence of f44 with altitude. Model observations using the WRF-Chem allowed us to plot changes in f44 along the flight track against modeled cross section curtains for aerosol age in this region.

Altitude versus latitude data colored by f44, superimposed upon the WRF-Chem model curtain from RF 12 (09/24/16), is displayed in Figure 33. This flight is optimal for comparison with the model because the cross section from the model is along 10°E, and target of opportunity flight RF12 was flown up the coast along 10°E to -8°N. The changing values of f44 align exceedingly well with the colored contours from the model. We do not observe a consistent relationship between f44 and other reliable chemical tracers, nor did we see a relationship between f44 and flight parameters such as longitude or latitude because the physical and chemical properties of the plume varied each day with respect to meteorological conditions. The f44 markers are colored by light blue (less f44) to pink (more f44), while the aerosol age contours are colored by blue (younger) to dark green (older). Where the f44 transitions from blue to pink, the WRF-Chem contours shift from blue to green.

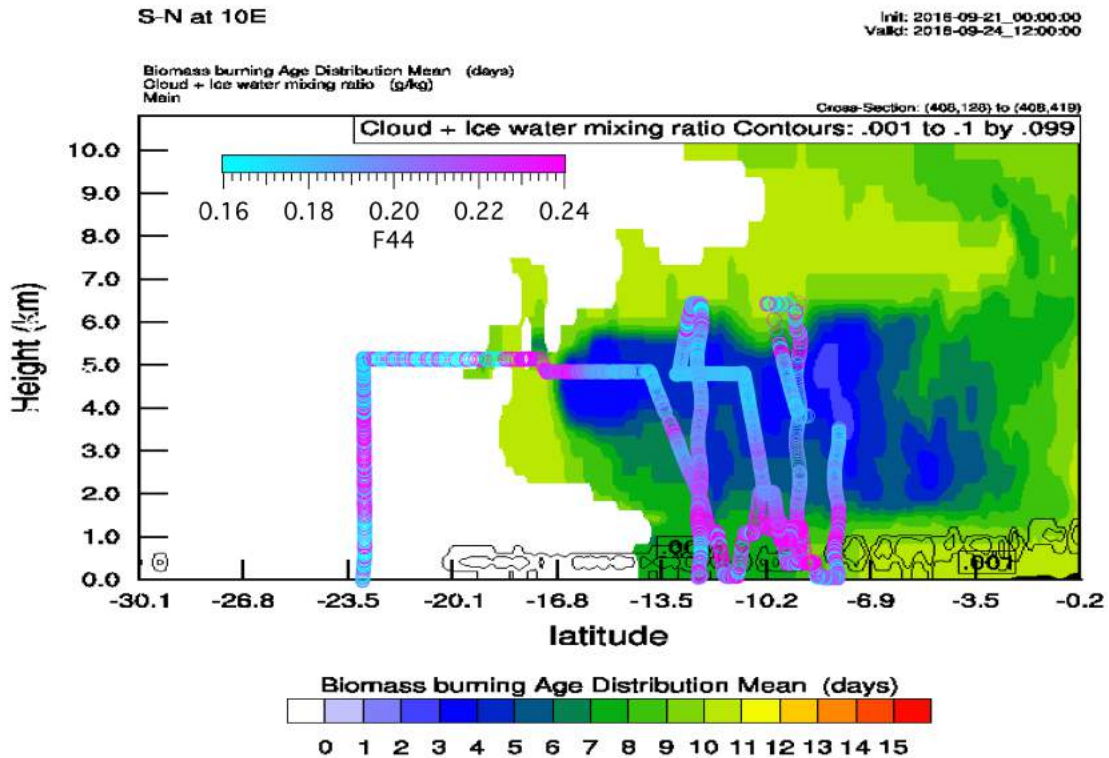


Figure 33. Altitude vs Latitude plot of biomass burning age (blue to green contours) (RF12) traveling S to N along 10 °E with the flight track colored by f44 (light blue to pink) super imposed on top. Coherence of these metrics suggest that f44 can be potentially used as a qualitative indicator of age.

The observations in changing f44 with modeled age gives us confidence in using f44 as a tracer for BB age as opposed to the changes being related to significant differences in burning sources. These results also provide positive feedback for the WRF-Chem model. The absence of a coherent pattern of f60 with age, suggests that f60 is a tracer for BB only for shorter periods. The aerosol from this region is ideal for studying aerosol aging processes because we see a wide range of age (48 hours to over 216 hours), and the plume has not been contaminated by other non-BB air masses due to the absence of major chemical changes between plumes (Figures 27-29 in Section 4.2).

4.5 Comprehensive Studies.

The Biomass Burning Observation Project (BBOP), a ground based and aircraft project studied BB in the western United States (Collier et al., 2016; Zhou et al., 2018). This study looked at fresh, over fire aerosol on the G-1 aircraft, and aged aerosol air on the order of 12 hours at Mount Bachelor, Oregon (Collier et al., 2014; Zhou, et al., 2018). Unfortunately, at their ground location they reported contamination from downwind urban/city sources, and in their aircraft study they were only able to follow individual plumes for a few hours before picking up chemical signatures from other aerosol sources. Aerosol aging studies have also been performed in chambers to prevent outside aerosol contamination. The FLAME III study done at the Missoula Fire lab (Missoula, MT) showed that aerosol oxidation occurred on a time scale on the order of three hours (Hennigan et al., 2011). Creating chamber conditions that mimic actual atmospheric conditions is tricky, however, and it is often difficult to use UV light and O_3 as methods to oxidize the aerosol at rates comparable actual atmospheric oxidation.

The ORACLES study region was ideal because aged and fresh BB aerosol were coming from very similar sources from the same region. With this range (48 hours to 216+ hours) of BB aerosol age, we can observe f44 versus total organic carbon (TOC) to very crudely quantify OA lifetime in the atmosphere. Cubison et al. (2010), Hennigan et al. (2011), Jolleys et al. (2014), Forrister et al. (2015), and Hodzic et al. (2016) show that after an unknown amount of time in the atmosphere, on the range of hours to days, the concentrations of OA begins to decrease due to fragmentation, volatilization, and evaporation. A trend of decreasing TOC with age can be seen with ORACLES RF12 data (Figure 34). As mean age (from WRF-Chem) increases, TOC/BC decreases, which

is what we would expect after a certain amount of time has elapsed. To ensure that the observed correlation of TOC:BC with age is not an artifact of decreasing aerosol concentrations in the plume, or potentially different burning conditions, we have plotted only data points where the BC:CO ratio is between 0.0095 and 0.00105, since BC and CO are conserved tracers. We divide TOC by BC to remove the effects of dilution with background air. The symbols in Figure 34 are colored by f44 to show that OA is removed as f44 increases.

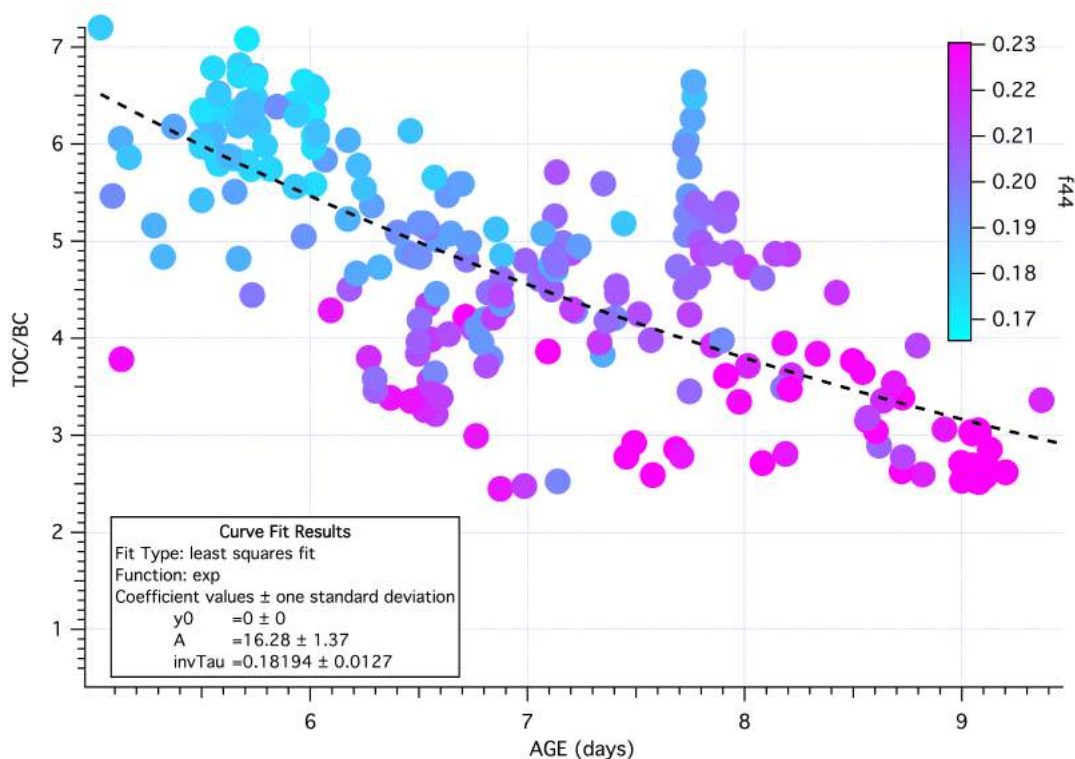


Figure 34. Age (days) versus TOC/BC. Symbols are colored by f44. An exponential fit (dashed black line) is calculated to show the relationship between age and TOC/BC. ($f(x) = y_0 + Ae^{(-x \cdot \text{invTau})}$)

The observed loss of TOC with WRF-Chem mean age are preliminary, but show promise for contributing greatly to the aerosol community. The results presented here show that f44 has a longer lifetime in the atmosphere (over 48 hours) than most studies report (Cubison et al., 2010; Hennigan et al., 2011; Jolleys et al., 2014; Forrister et al.,

2015; Hodzic et al., 2016). Loss of TOC begins after 5 days in the atmosphere (x-axis). We did not see a relationship with TOC and age before 5 days for this set of data. We can estimate half-life of TOC to be around 3.5 days using the relationship between TOC/BC and age presented in Figure 34. The mechanisms behind TOC loss are still uncertain, but we propose two possibilities. TOC loss could have occurred before day five, but SOA production overshadowed TOC loss because of this, SOA was replaced the mass that was being lost. After day five SOA may have diminished sufficiently for loss of TOC to become more evident. An alternative mechanism may be driven the chemical components of OA. Initial TOC losses could have occurred within the first 48 hours of burning, before the plume was sampled. In the subsequent three days in the atmosphere, a second oxidation process occurs. This aerosol is chemically more stable, resides for longer periods of time in the atmosphere. Additional data is required to test either of these hypotheses.

If our estimates of TOC loss with age proves robust, it could explain the chemical structure of the plume. Our results of TOC loss with age suggest a young upper plume, and an aged lower plume. The ratio of BC:OA (see Chapter 3) is higher in the lower plume, which is consistent with loss of TOC; while BC remains constant and OA is lost, the ratio of BC:OA increases in the lower plume. The BC:OA results have implications for SSA and optical properties research being done by other ORACLES researchers. The ability to quantify TOC loss over time to explain the optical and chemical properties of African BB would contribute greatly not only to the science objectives and goals of ORACLES, but to the aerosol community as a whole. The ability to make independent estimates of age using f_{44} , would also help modelers improve the parameterizations of

chemical and optical properties of aerosol in global models, a factor critical to radiative forcing calculations.

4.6 SAFARI 2000 Comparison

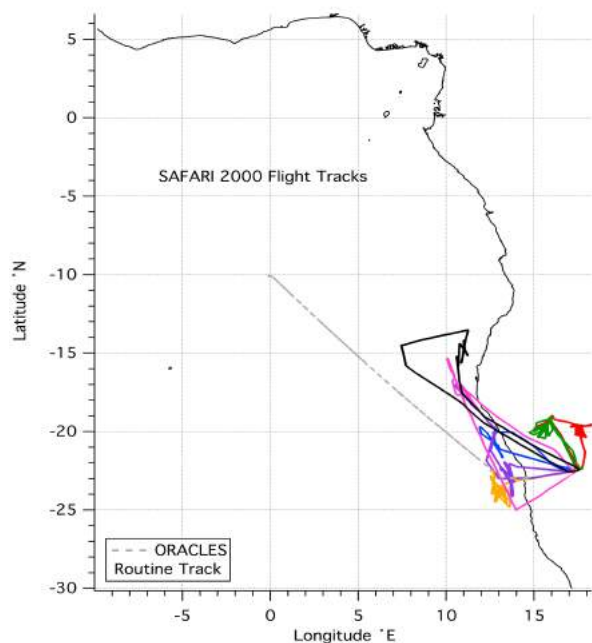


Figure 35. Flight tracks from SAFARI 2000. ORACLES 2016 routine flight track is for perspective (grey dashed line). SAFARI 2000 data from https://daac.ornl.gov/cgi-bin/dsviewer.pl?ds_id=720

The UK Met Office, participated on the SAFARI 2000 campaign, basing their C-130 out of Windhoek, Namibia (Formenti et al., 2003; Haywood et al., 2003). Flights were typically flown over the SEA and along the west coast of Africa. Their research was conducted closer to shore than ORACLES flights (Figure 35).

Aerosol was collected on 20-30-minute level legs with a stacked filter system, described by Formenti et al. (2003). Level legs are designed to ensure sufficient

loading on the filter samples. Concentration of water extractable ions (Cl^- , NO_3^- , SO_4^{2-} , NH_4^+) was determined using ion chromatography, and conductivity detection and total carbon ($\text{TC} = \text{EC} + \text{OC}$) was collected on quartz filters. The quartz filters were analyzed using thermo-optical techniques. It should be noted that BC was not measured optically for “blackness”, but instead for the refractory part of the carbon, assuming that EC volatilizes at a higher temperature in an oxidizing atmosphere. CO was measured with a fast response fluorescence instrument that was built for the C-130 (Haywood et al., 2003, Formenti et al., 2003). These researchers were able to characterize the bulk

chemical species of the plume, their vertical distributions, and the influence of biomass rich aerosol interactions with cloud conditions, as well as under cloud-free conditions.

The group calculated enhancement ratios (ER) of various gaseous and particulate tracers as a proxy for age and type of emissions. Due to the different instrumentation and data sets collected, the ER using O₃ was the only comparison we could make with ORACLES data. Formenti et al. (2003) report an ER for O₃ relative to CO of 0.26±0.03 in the SAFARI 2000 plume. ORACLES plume data filtered to OA > 12µg/m³ displayed a range of ER values: the lowest ER calculated was 0.32 from flight 4 (09/04/16), while the highest ER of 0.65 on RF13 (09/25/16). In both studies, the ER indicates that significant photochemical production of O₃ has occurred (Formenti et al., 2003). Formenti et al. (2003) report an ER 0.26 as being very aged aerosol; and we did not observe an ER in plume below 0.32. The ER results of ORACLES can be found in Table F.1 in Appendix F. The ORACLES ER for O₃ is much higher than the ER reported for SAFARI 2000. The elevated ORACLES ER is likely due to higher ozone production. On average in the plume, ΔO₃ values between ~100-120ppbv were observed, and SAFARI 2000 observed O₃ values between ~70-100ppbv.

The chemical ratios of OA, BC, SO₄, and NO₃ from ORACLES and SAFARI 2000 are represented in Figure 36a and Figure 36b. The ORACLES data was taken from the average concentration of the species between 1500m and 3500m, the lower layer of the plume. Concentrations and ratios from SAFARI 2000 compared to ORACLES can be found in Table F.2 in Appendix F. Because the NO₃, SO₄, and NH₄ data from SAFARI 2000 were analyzed using ion chromatography techniques, only the inorganic form of these ions were detected (Formenti et al., 2003). While, the AMS does not effectively

differentiate organic versus inorganic sulfates and nitrates this chemical similarity between SAFARI 2000 and ORACLES 2016, strongly suggests that NO_3 , SO_4 , and NH_4 are largely inorganic in ORACLES too.

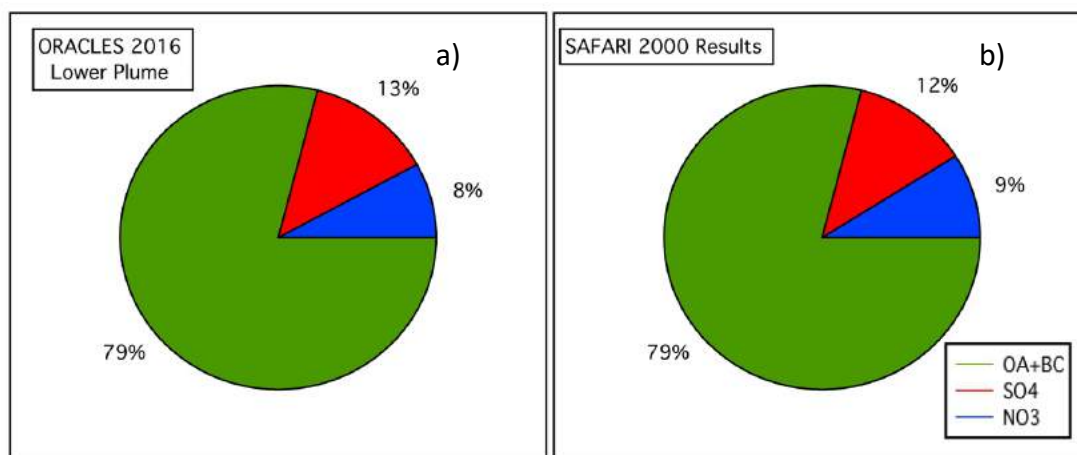


Figure 36. a) Pie chart of ORACLES chemical ratios averaged over 1500m-3500m. b) Pie chart of average values reported by Formenti et al. (2003) for SAFARI 2000.

Another chemical similarity observed between ORACLES and SAFARI 2000 was in the organic matter (OM) to organic carbon (OM/OC) ratio. Because of the thermo-optical analysis techniques used, the calculated OC is actually in terms of total carbon (TC). To convert TC into OC, a factor of 2.6 was applied (Formenti et al., 2003). The AMS analysis calculates this ratio as well, and the average value for ORACLES in plume data was 2.45. Typically for fresh aerosol, the OM/OC ratio is ~1.4 (Russell, 2003). In aged aerosol, as the amount of oxygen increases the OM/OC ratio increases. Data for both SAFARI 2000 and ORACLES 2016 are characterized by a high OM/OC ratio.

Comparable to the ORACLES results, the SAFARI 2000 results revealed a layered plume structure. Vertical profiles from Haywood et al. (2003) using CO, scattering, and PCASP concentrations show this stratified plume structure (Figure 37).

The main aerosol layer occurs between 3000m and 5000m (Haywood et al., 2003), with a second elevated layer present down to 2000m above sea level. Studies from SAFARI 2000 also report a gap between cloud top and aerosol haze layer. In ORACLES we witnessed this gap ~60% of the time. For comparison, a vertical profile from ORACLES can be found in Figure 16a in Section 3.1.

A comparison of optical properties between SAFARI 2000 and ORACLES 2016 revealed some interesting overlap. In Section 2.2.5 we discussed mass scattering efficiency in ORACLES 2016 data, for which a campaign average was 5.9. Formenti et al. (2003) report a value of 4.2. Both studies used a nephelometer to measure submicron scattering. Formenti et al. (2003) also reported a single scattering albedo (SSA) of 0.93. The ORACLES SSA is reported to be ~0.85. The lower SSA in ORACLES indicates presence of a more absorbing aerosol. Both the lower SSA and higher mass scattering efficiency observed in ORACLES could be due to aerosol size and composition differences between the two studies.

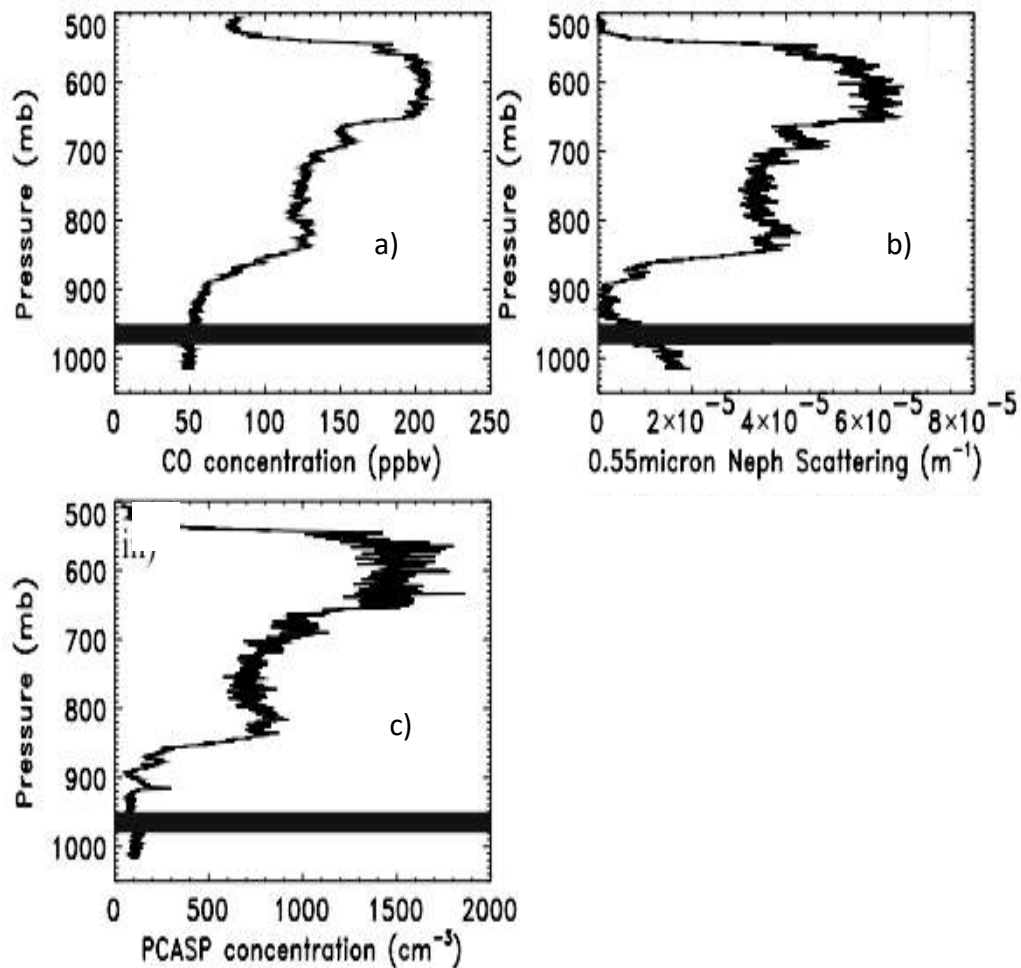


Figure 37. Adapted from Haywood et al. (2003). The vertical structure of the plume revealed by **a)** CO (ppbv), **b)** scattering(Mm^{-1}), and **c)** PCASP concentration. Thick black line indicates cloud top.

The University of Washington Convair-580 also participated on SAFARI 2000. This aircraft sampled fresh BB from five different continental regions: Zambia, Botswana, Mozambique, South Africa, and Namibia (Sinha et al., 2003). With similar instrumentation as the C-130, they were able to provide a chemical analysis of the over fire plumes as opposed to the haze sampled over the SEA. Their results are consistent with those observed by the C-130, and they also provide supplemental and supporting results for ORACLES 2016 (Formenti et al., 2003; Haywood et al., 2003; Sinha et al.,

2003). The chemical comparison between the Convair-580 and the ORACLES P-3B can be found in Table F.2 in Appendix F. When we compare our plume composition to their five sites, it appears that our data resembles the Botswana region most closely, as shown in Figure 38. The data presented by Sinha et al. (2003) reflects freshly emitted BB because they were able to fly directly over fire sources. The chemical differences observed in their BB aerosol results are most likely due to their sampling of individual plumes, as contrasted with the amassed plume sampled in ORACLES 2016. However, their description of methods for averaging data are unclear (Sinha et al., 2003), and for some sites the number of samples is insufficient samples to provide a robust argument for an average (e.g., some sites only had one or two data points).

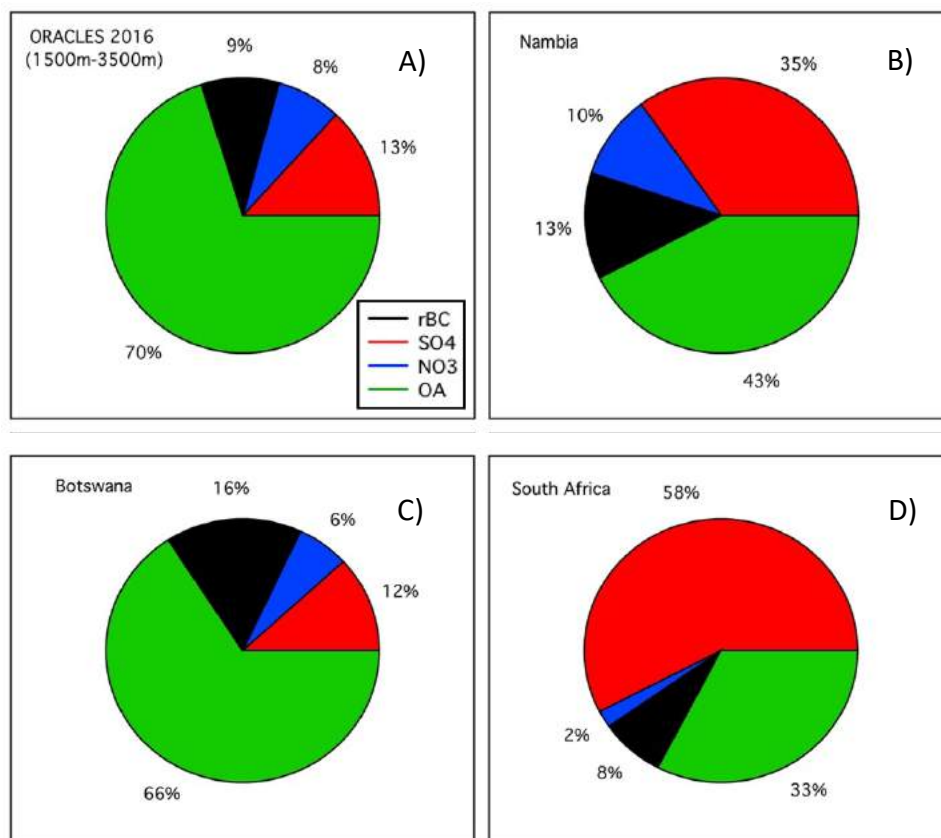


Figure 38. Pie charts based on the data presented in Sinha et al. (2003), who report the average concentration for the bulk chemical species (OA, BC, SO₄, and NO₃) in Namibia (B), Botswana (C) and South Africa (D). The average chemical composition from ORACLES for the 1500m-3500m plume is presented for comparison (A).

Overall, the comparison of results from SAFARI 2000 and ORACLES 2016 was similar. Although instrumentation and techniques were different, similar chemical ratios, plume structures and aerosol interactions with clouded and cloud free conditions were observed in both studies. Arguably the most important results were the similarities in chemical composition. This coherence of results between the two studies provides support for our claim that the concentrations of NO_3 , SO_4 , and NH_4 observed during ORACLES are mainly inorganic. The OM/OC ratio for aged OA between SAFARI 2000 (Formenti et al., 2003) and ORACLES were also similar with values around 2.5. Slight variation in optical properties of the aerosol, that can most likely be attributed to size and slight composition differences in aerosol sampled between the two studies. ORACLES was able to provide data at higher time resolutions, more optical property measurements, and better cloud sensing data.

Using HYSPLIT, Sinha et al. (2003) ran five day AMBT for the plumes they observed. Figure 39 shows a very robust analysis of where they believe their aerosol originated. Their research methods were described above in Section 4.4. The black ovals on the map indicate their five study regions. Their analysis quantifies how much aerosol is coming from a specific region. As was observed in ORACLES, appears that the source of the BB sampled during SAFARI 2000 derives from the general southern region of Africa. The violet arrows below indicate back trajectories calculated for the aerosol they studied in the Namibian region (Figure 39). They report 50% of their back trajectories passing through the Angola region. We also saw this pattern of high aerosol concentration source coming from the Angola region. The aerosol most likely came from fires in the Angola region, or other nearby regions, but the air mass spent quite a bit of

time over the continent before being lofted over the ocean. Lastly, they report 14% of the AMBTs come from the Botswana region. We also saw aerosol trajectories coming from the southeastern region of Africa.

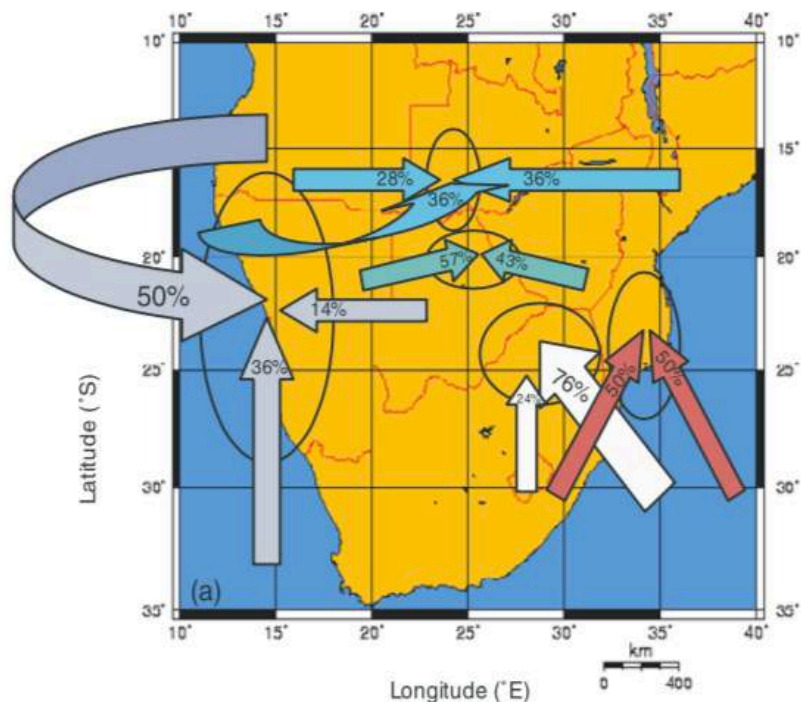


Figure 39. From Sinha et al (2003). Different colored arrows indicate which region the aerosol samples were collected from. Violet=Namibia, Red=Mozambique, White=South Africa, Blue=Zambia. The arrows are then labeled with the percentage of aerosol originating from the HYSPLIT predicted region.

Chapter 5. Conclusions

The 2016 ORACLES campaign flew 14 successful research flights during the month of September over the Southeast Atlantic Ocean to sample seasonal African BB aerosol. Using in situ data from a suite of instruments, we report on the chemical structure and composition of the BB plume. Overall, the plume composition was very consistent throughout the campaign. The relationships of BC:CO and MCE show that there were not significant removal mechanisms, nor were there indications of significant source differences. The relationships between OA:BC and OA:CO were more variable, but were still pretty consistent across flights. These slight variations can be attributed to changes in OA. One of the most noticeable features of the plume was the consistent layering structure. We continuously saw two distinct aerosol plumes; the upper plume was generally found between 3500m and 5500m, while the lower plume was found between 1500m and 3500m. The upper layer had higher NO₃:OA ratios, and lower values of f₄₄, while the lower plume had lower NO₃:OA ratios and higher values of f₄₄. Using standard analysis techniques, we were able to determine that the two plumes were most likely from similar sources, but had undergone different chemical reactions. Due to the uniformity of the plume based on conserved species such as BC, CO, and CO₂, we are confident that aerosol in these two layers do not derive from different sources. We can best explain the layering structure of the plume with aerosol aging and photooxidation reactions.

First, the chemical differences observed for SO₄, NO₃, and NH₄ between the two plumes are due to ammonium reactions with sulfate and nitrate, but can also be linked to plume age. We predict the lower plume to be older, and that can be supported by the

higher SO₄:OA ratios. With an older, more oxidized lower plume, the SO₂ has more time to react to form H₂SO₄, which gets preferentially neutralized by the ammonium, thus increasing the concentration of SO₄ in the lower plume. The upper plume on the other hand has had less time to react, thus lower concentrations of sulfuric acid, and more nitric acid can be neutralized which contributes to the higher NO₃:OA ratio (Figure 30).

The second explanation for plume structure, particularly OA, is due to aerosol aging and loss over time. Based on initial OA analysis, we thought we were seeing mainly aged BBOA, and very little fresh BBOA indicated by a high O:C ratio, a low H:C ratio, high oxidation states, lack of f60, and elevated levels of f44. Changes in those variables across flights could not be explained by changes in source, longitude, latitude, or altitude. We chose to use f44 as a chemical tracer for BB age based on research done by Aiken et al. (2008), Cubison et al. (2010), Jolleys et al. (2015). However, their research quantified the lifetime of f44 to be on the order of 3 hours to 48 hours. We were initially convinced that the changes we were seeing were insignificant because we could not find a relationship between f44 and another reliable chemical tracer. We also thought our aerosol was much older than 48 hours, which is longer than the predicted lifetime of aerosol age indicators. We thought the variation in O:C, and f44 were just differences between old, and older aerosol, and that the lifetime of these tracers would not be able to show us aerosol aging mechanisms.

Using WRF-Chem models and HYSPLIT back trajectories we were able to compare f44 with predicted aerosol age, and to determine age differences between the upper and lower plume. The results from HYSPLIT showed the lower plume mixed with the continental boundary layer for 5 days, whereas the upper plume interacted with the

continental boundary layer only on the last day before being transported over the SEA (Figure 32).

Preliminary results using WRF-Chem reveal a relationship between f44 and mean age (Figure 33). We were also able to demonstrate TOC loss with age. Results show that as the mean age predicted by WRF-Chem increased, TOC/BC decreased after 5 days (Figure 34). However, there remain large uncertainties associated with quantifying loss, and with the chemical reaction mechanism driving the loss of TOC. By combining both results from HYSPLIT and from WRF-Chem we can conclude that losses are occurring in the lower plume because it is the older plume. The losses in the lower plume are believed to be driving the chemical differences between OA and BC. With TOC being lost, and BC conserved, the ratio of BC:OA increases in the lower plume. These results are particularly important for researchers who study the optical properties of biomass burning, because aerosol optical properties can be largely influence by chemical properties.

Overall, we believe aerosol age to be the driving mechanism between the upper and lower plume. An older, more oxidized lower plume is supported by higher SO_4 :OA ratios, HYSPLIT mixed layer depth, high values of f44, and the loss of TOC. The idea of a younger upper plume is supported by low values of f44, high NO_3 :OA ratios.

Although the ORACLES project was conducted 16 years after SAFARI 2000, general chemical plume characteristics and plume structure were surprisingly similar, especially considering the different sampling techniques used in the two studies. By comparing ORACLES chemical composition data to SAFARI 2000 composition data, we

were able to strengthen our hypothesis that the observed species of nitrate, sulfate, and ammonium are inorganic.

The chemical properties and spatial structure of the plume contribute greatly to the overarching science objectives of ORACLES. Using these analysis techniques for the 2016, 2017, and the 2018 campaigns, we will be able to determine the nature and magnitude of the seasonal variability of chemical species in aerosol produced by African biomass burning. These results will either verify or help improve local and global climate models, such as the WRF-Chem model. Knowing how the aerosol reacts, and quantifying the lifetime of OA in the atmosphere, will also contribute to radiative forcing research. Previous reports show OA loss within the first two days, but if those results overestimate the rate at which OA is lost, the implications on radiative forcing could be biased towards a radiative cooling effect. In contrast, our results suggest that OA may have a longer lifetime in the atmosphere, which could in turn bias results towards a warming effect. The results presented here will have a positive impact on the aerosol and atmospheric science communities.

Future work will include using the same analysis techniques on the ORACLES August 2017 and October 2018 data to observe seasonal changes within the chemical species. The results presented for f44 and the WRF-Chem model are still preliminary, and we would like to be able to confidently quantify TOC loss with age.

Appendix A.

Appendix A includes figures and tables from Chapter 1, Introduction and Chapter 2, Methods.

Table A.1: Direct, indirect, and semi-direct effects on climate over the SEA

Table A.2: Summary of HIGEAR instruments, their measured parameter, and importance to this study.

Table A.3 Calculated mass total ($\mu\text{g}/\text{m}^3$) versus submicron scattering (Mm^{-1}) values for 3 different altitudes per flight.

Figure 1. Example of the calculated mass total Calculated mass total ($\mu\text{g}/\text{m}^3$) versus submicron scattering (Mm^{-1})

Table A.4 Vaporizer test results

Figure 2. Results of timing test I

Figure 3. Results of timing test II

Table A.1. Direct, indirect, and semi-direct effects on climate over the SEA

Climate over SEA	Direct, Indirect, Semi-Direct	Warming (+) or Cooling (-)
Cloud burn off (aerosol cloud interaction)	Semi-Direct	+
Cloud Albedo & Lifetime	Indirect	-
Aerosol above cloud/ Absorption/scattering	Direct	+ or -
Cloud thickening	Semi-Direct	-

Table A.2. Summary of HIGEAR instruments, their measured parameter, and importance to this study.

Instrument	Measured Parameter	Importance to this Study
Aerosol Mass Spec (AMS)	Bulk Aerosol Composition	Indicators of BB influence, composition
Single particle soot photometer (SP2)	Black Carbon Mass Concentration	Indicator of BB, contributes to total carbon concentrations
Particle Soot Absorption Photometer (PSAP)	Absorption	Absorption Angstrom Exponent (AAE)
Nephelometer	Scattering (total and submicron)	Aerosol property
CN counters	Concentration of particles	Measures concentration of particles in different size ranges
UHSAS	Particles between 60nm-1000nm	Sizes particles in the accumulation mode
APS	Particles between 800nm to 10000nm	Measures large particles such as dust
TDMA	Particles between 10-300nm	Size distributions, particle mass, surface area, number distribution
LDMA	Particles between 10-550nm	Size distributions

Table A.3 Calculated mass total ($\mu\text{g}/\text{m}^3$) versus submicron scattering (Mm^{-1}) values for 3 different altitudes per flight.

Research Flight #	Altitude 1	Altitude 2	MBL	Average
02	5.24	5.09	3.57	4.634 ± 0.93
04	7.36	7.06	8.21	7.544 ± 0.59
06	4.38	3.53	3.64	3.85 ± 0.47
07	3.21	3.93	na	3.57 ± 0.51
08	7.25	6.44	9.10	7.60 ± 1.3
09	4.83	6.18	5.24	5.42 ± 0.69
11	9.16	8.66	14.33	10.72 ± 3.1
12	4.61	5.69	3.05	4.45 ± 1.3

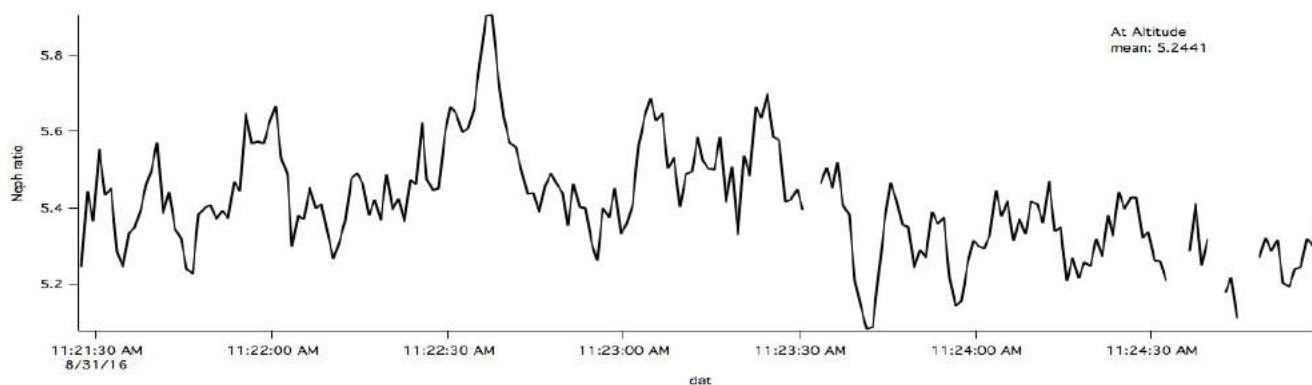


Figure 1. Example of the calculated mass total ($\mu\text{g}/\text{m}^3$) versus submicron scattering (Mm^{-1}) (called Neph ratio) versus time from RF02 08/31/16. This particular segment is an average of the ratio above 2000m.

Table A.4 Vaporizer test results

Temperature ($^{\circ}\text{C}$)	OA ($\mu\text{g}/\text{m}^3$)	Scattering (Mm^{-1}) 550nm	LDMA (p/cm^3)
700	+400 to -400	90	318
600	35	95	333.4
500	10	95-100	300

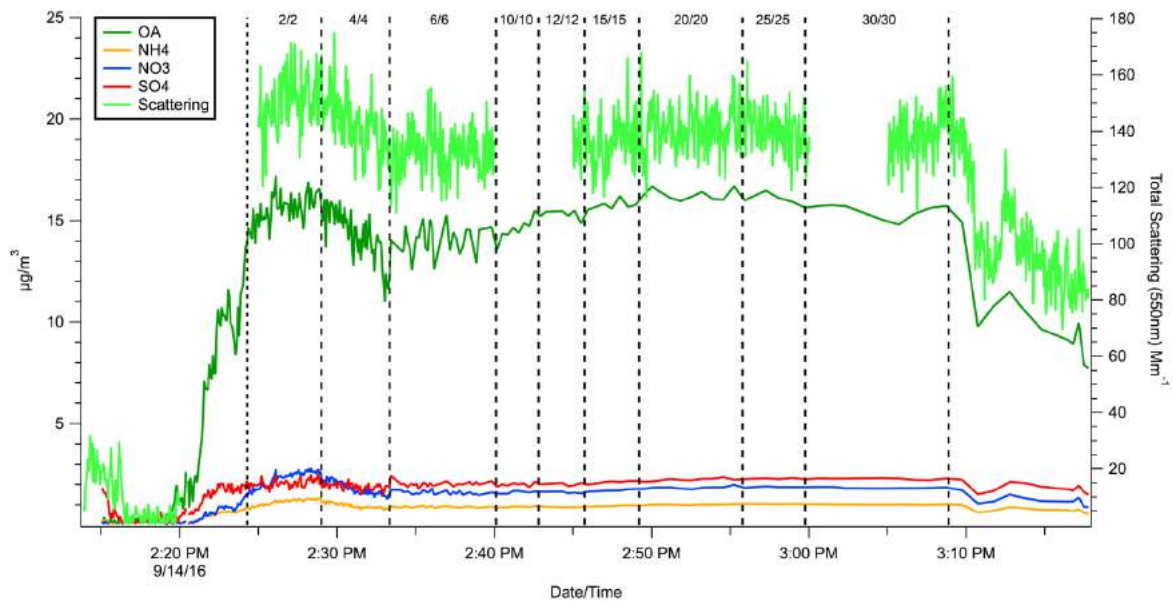


Figure 2. Results of the timing test. Black dashed lines indicate the different timing segments (open/closed). The left axis is aerosol concentration in $\mu\text{g}/\text{m}^3$, and the right axis is 550nm (green) total scattering.

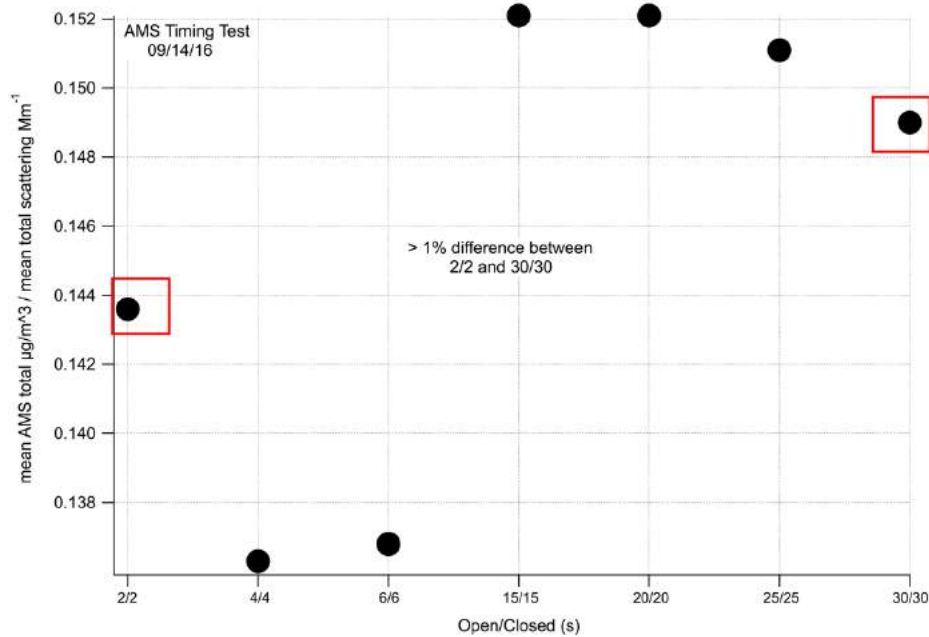


Figure 3. AMS mean concentration ($\mu\text{g}/\text{m}^3$) / mean total scattering versus the timing sequences displayed in Appendix A, Figure 2. Shows that there is no significant dependence of concentration with time resolution. Between 2/2 and 30/30 there is less than a 1% difference.

Appendix B

Appendix B includes figures and tables from Chapter 3, Results.

Table B.1: Table of date of flight, flight number, and short description

Table B.2: Concentrations of the bulk aerosol averaged over 1500m to 1000m intervals

Table B.3 Ratios of the bulk aerosol averaged over 1500m to 1000m intervals

Figures 1-12: Altitude vs Latitude plots for all flights. Marker is sized to OA ($\mu\text{g}/\text{m}^3$) and colored by the NO_3 :OA ratio. Brighter pink colors indicate higher NO_3 relative to OA.

Figure 13: Example of aerosol right above cloud from RF05 09/06/16

Table B.1. Table of date of flight, flight number, and a short description of the flight.

Date	Research Flight #	P-3B short description
08/31/16	02	Full routine towards 10S and 0E
09/02/16	03	TOO, mostly North along 10E
09/04/16	04	Full routine towards 10S and 0E
09/06/16	05	TOO, mixing survey
09/08/16	06	Full routine towards 10S and 0E
09/10/16	07	Routine(ish) flight to 10S and 0E
09/12/16	08	Routine(ish) flight to 10S and 0E
09/14/16	09	TOO, radiation near aerosol gradient
09/18/16	10	TOO, plume mapping
09/20/16	11	TOO, radiation fork and coordination
09/24/16	12	TOO
09/25/16	13	Routine flight to 10S and 0E

Table B.2. Concentrations of the bulk aerosol averaged over 1500m to 1000m intervals

Species	OA $\mu\text{g}/\text{m}^3$	NO₃ $\mu\text{g}/\text{m}^3$	SO₄ $\mu\text{g}/\text{m}^3$	NH₄ $\mu\text{g}/\text{m}^3$	BC $\mu\text{g}/\text{m}^3$	ΔCO ppbv
0-1500m	3.64±6.05	0.23±0.35	1.29±1.36	0.30±0.35	0.43±0.65	44.85±52.89
1500-3500m	10.22±9.49	1.11±1.14	1.91±1.69	0.71±0.65	1.34±0.96	125.46±76.98
3500-4500m	10.53±8.74	1.79±1.76	1.62±1.60	0.89±0.78	1.40±1.03	145.44±73.97
4500-5000m	7.40±8.70	1.33±1.63	1.05±1.10	0.68±0.81	0.72±0.89	94.11±71.98
5500-6500m	3.27±6.96	0.35±1.03	0.45±0.83	0.20±0.55	0.14±.41	50.59±49.40
6500-7500m	2.48±4.39	0.30±.68	0.44±0.63	0.15±0.38	0.12±0.27	69.59±41.27

Table B.3. Ratios of bulk aerosol averaged over 1500m to 1000m intervals

Ratio	NO ₃ :OA	SO ₄ :OA	BC:OA	NH ₄ :OA	NH ₄ :SO ₄	BC:CO
0-1500m	0.0632	0.3544	0.1181	0.0824	0.2326	0.0096
1500-3500m	0.1086	0.1869	0.1311	0.0695	0.3717	0.0107
3500-4500m	0.1700	0.1538	0.1330	0.0845	0.5494	0.0096
4500-5000m	0.1797	0.1419	0.0973	0.0919	0.6476	0.0077
5500-6500m	0.1070	0.1376	0.0428	0.0612	0.4444	0.0028
6500-7500m	0.1210	0.1774	0.0484	0.0605	0.3409	0.0017

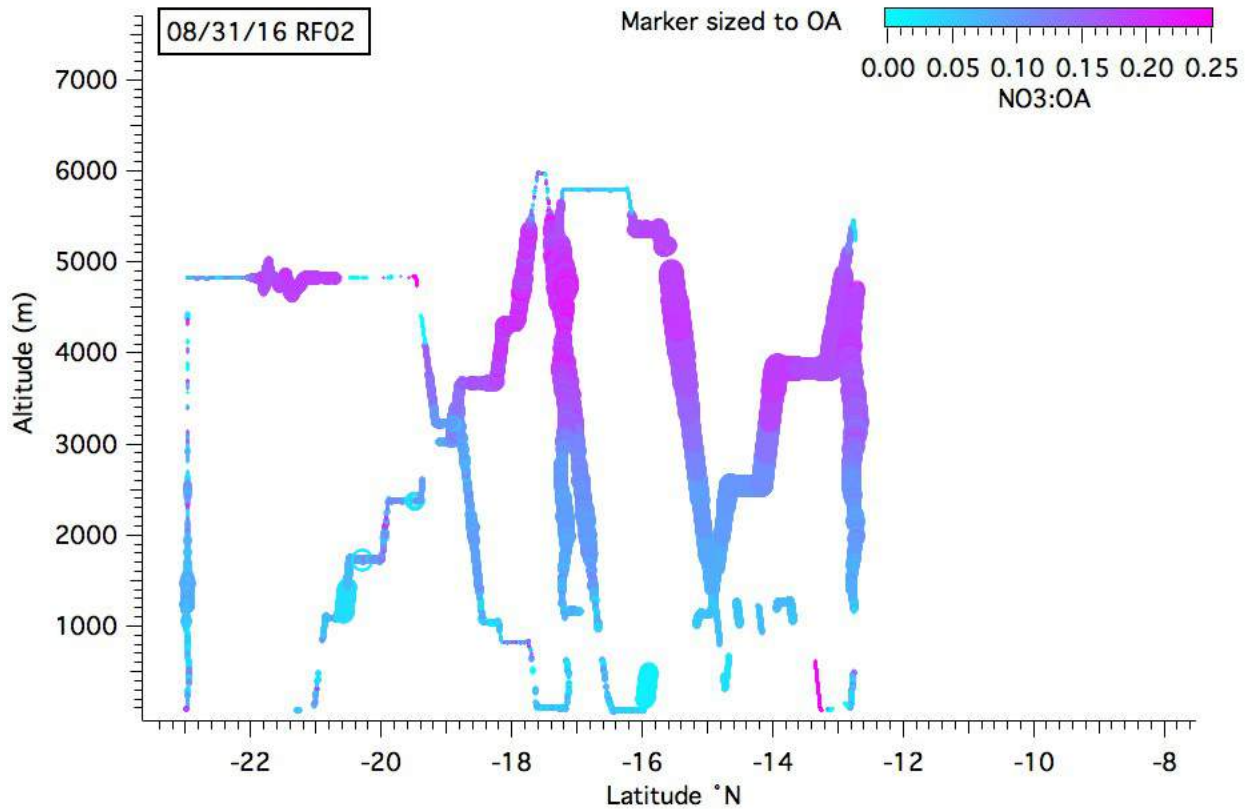


Figure 1. RF02 08/31/16

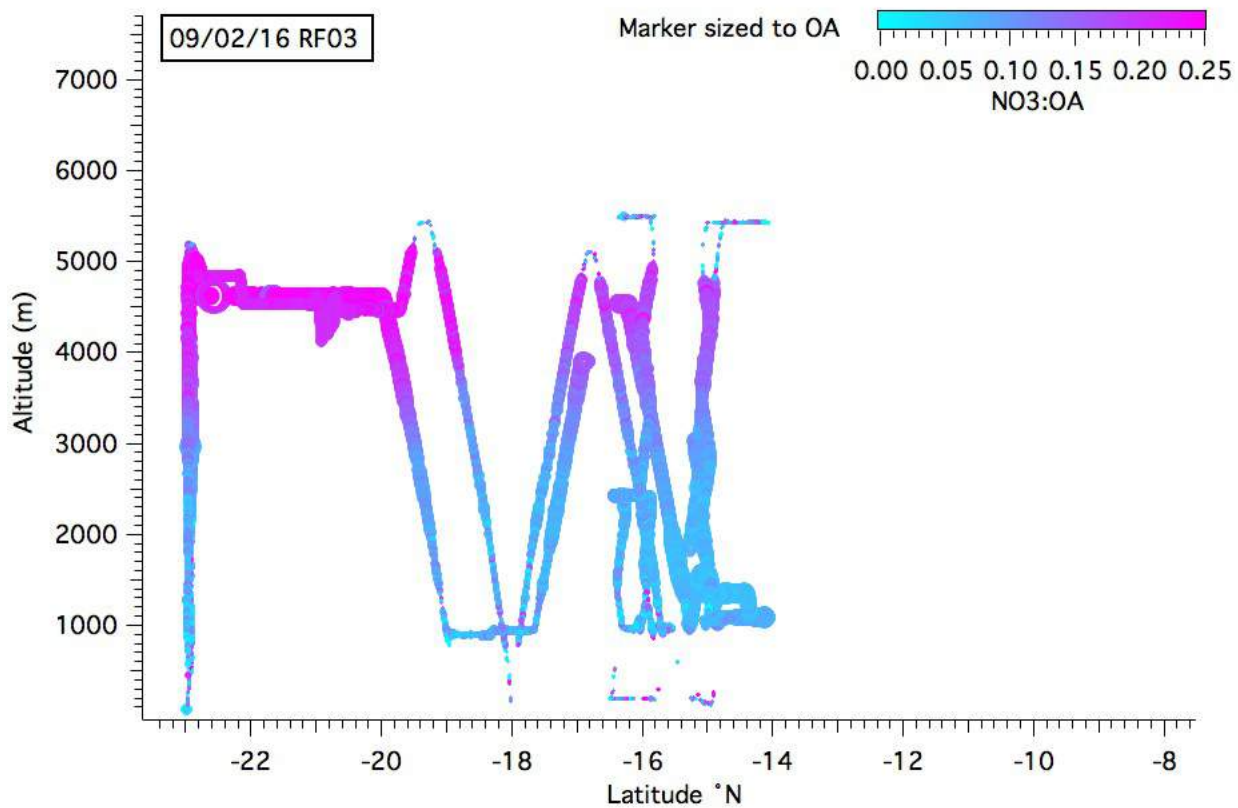


Figure 2. RF03 09/02/16

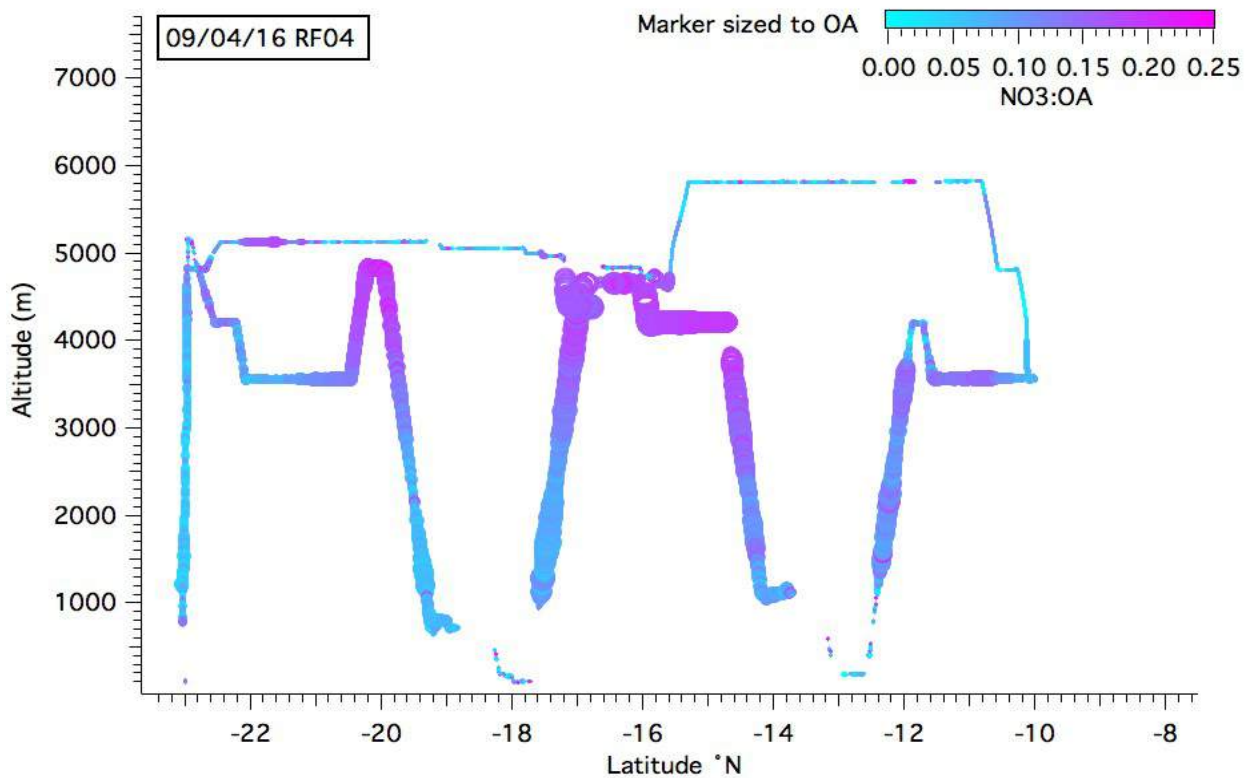


Figure 3. RF04 09/04/16

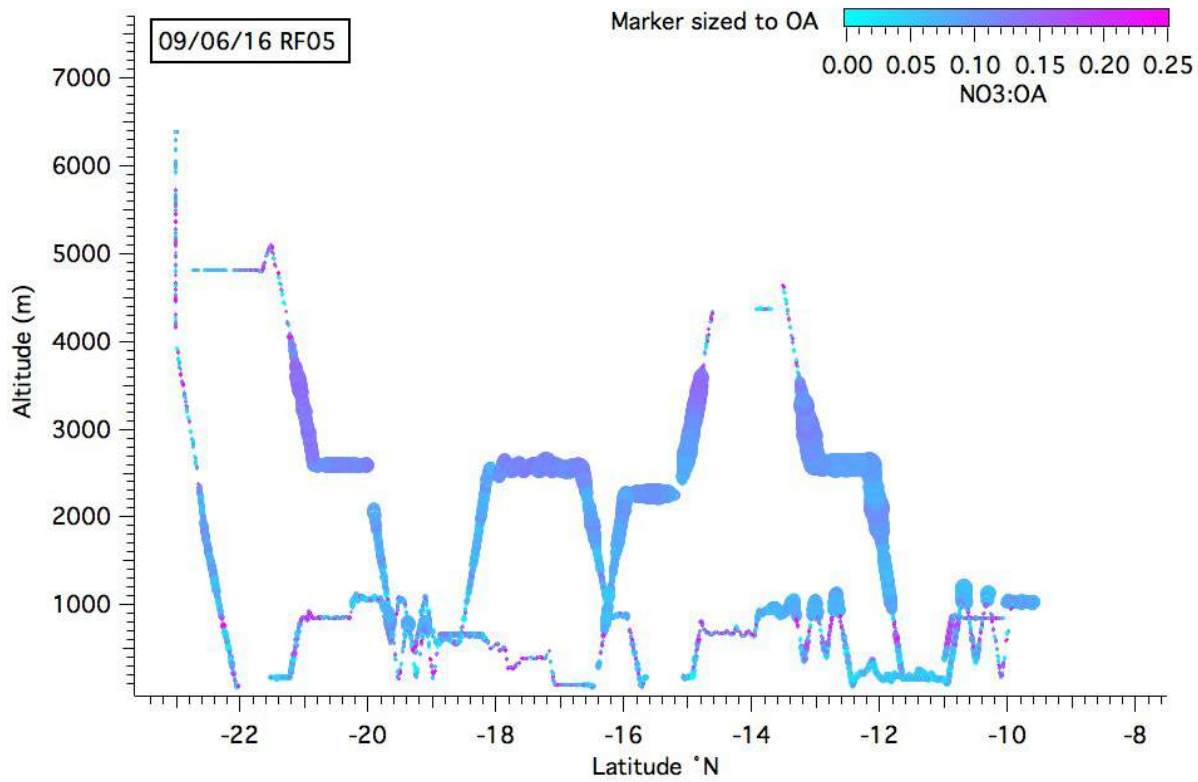


Figure 4. RF05 09/06/116

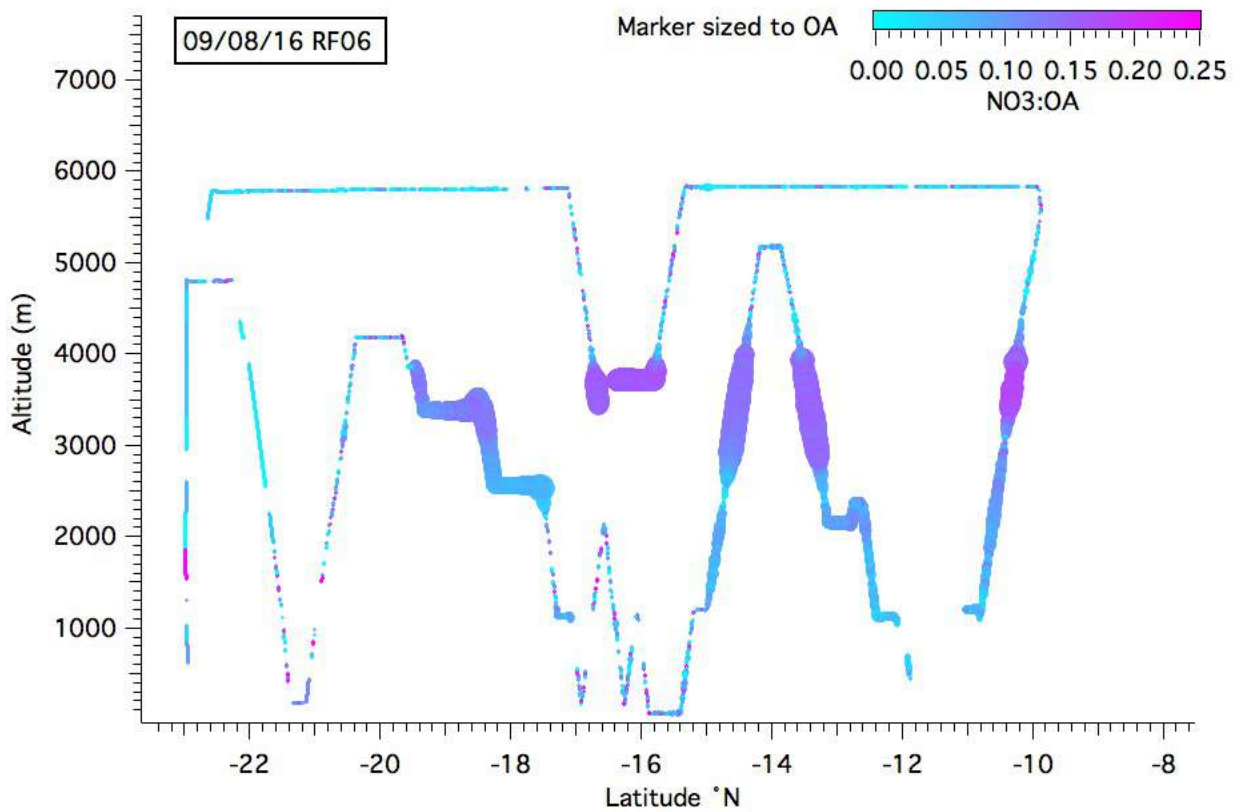


Figure 5. RF06 09/08/16

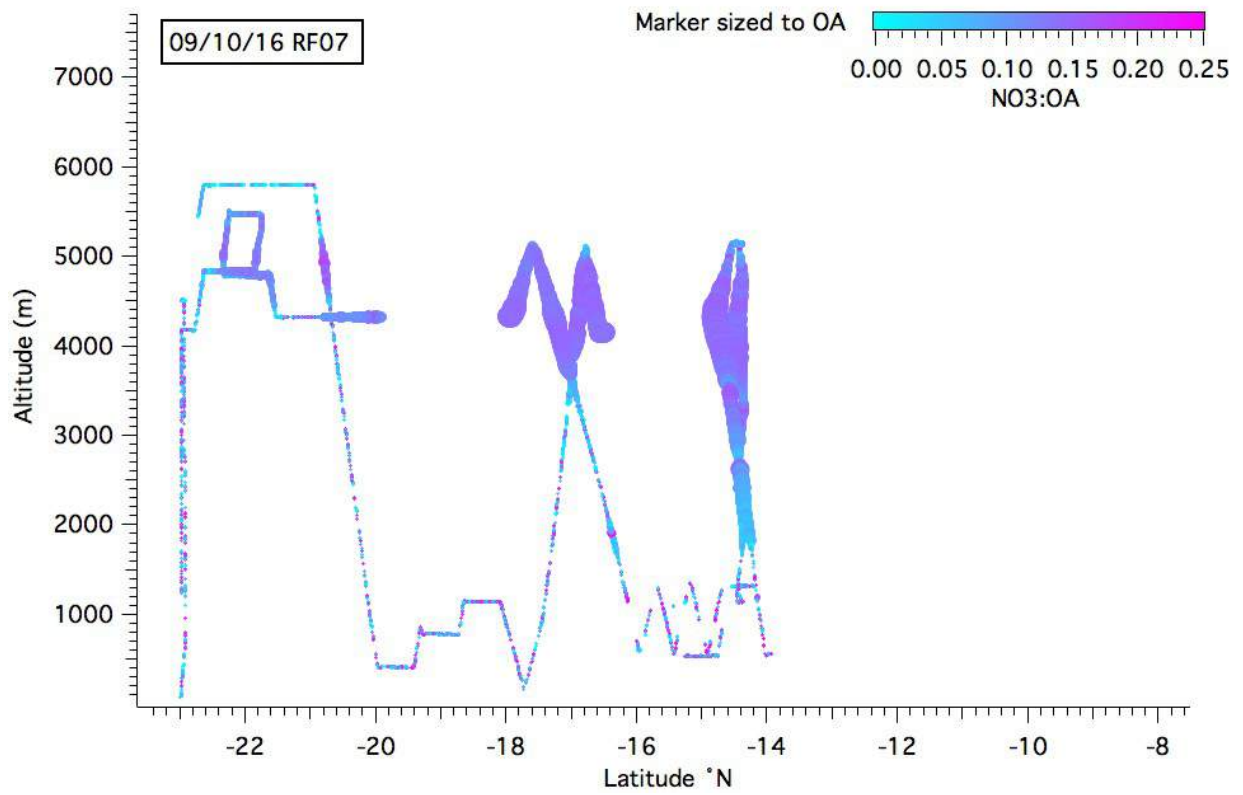


Figure 6. RF07 09/10/16

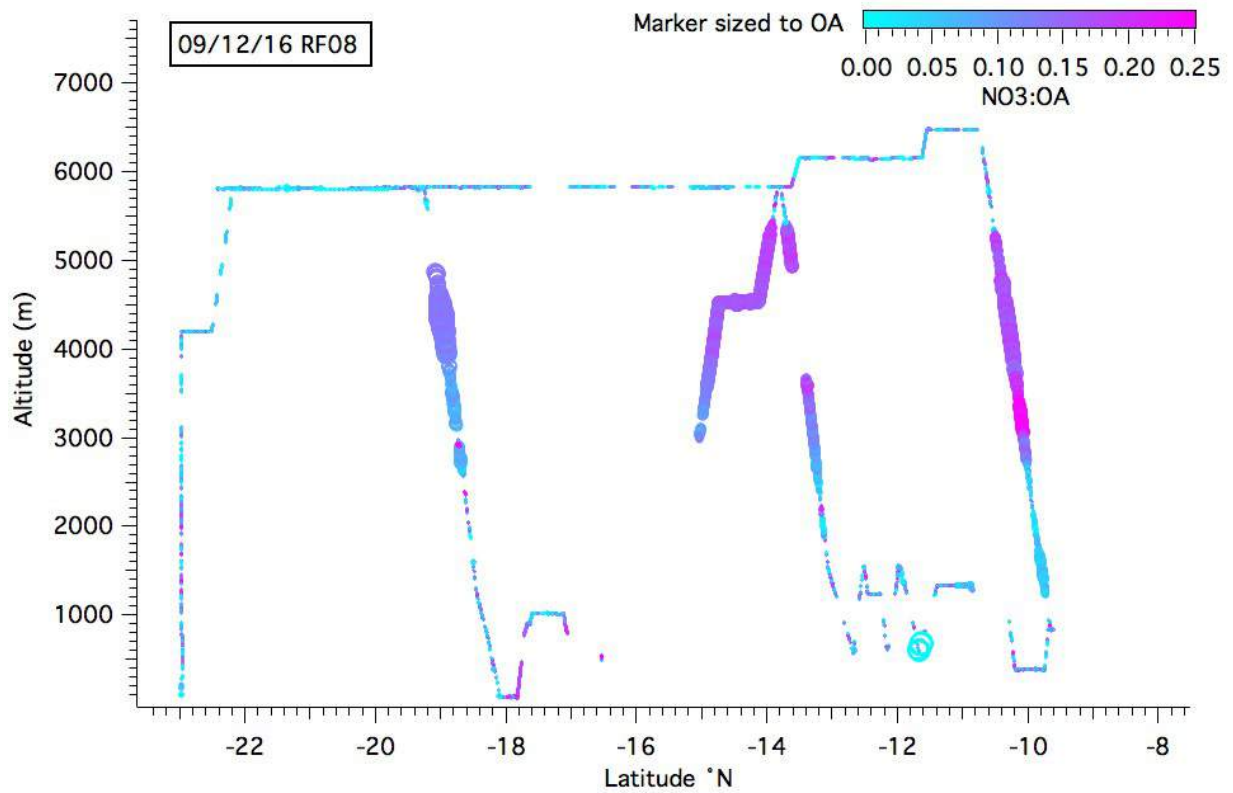


Figure 7. RF08 09/12/16

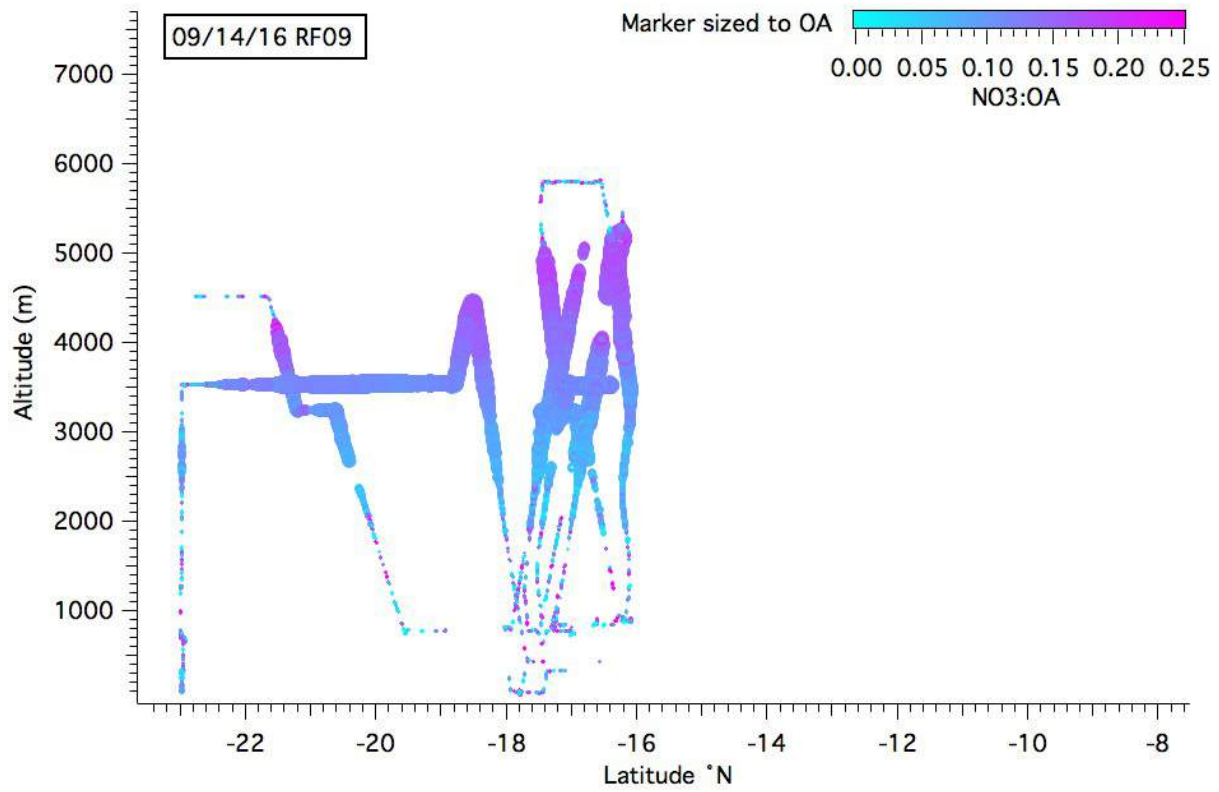


Figure 8. RF09 09/14/16

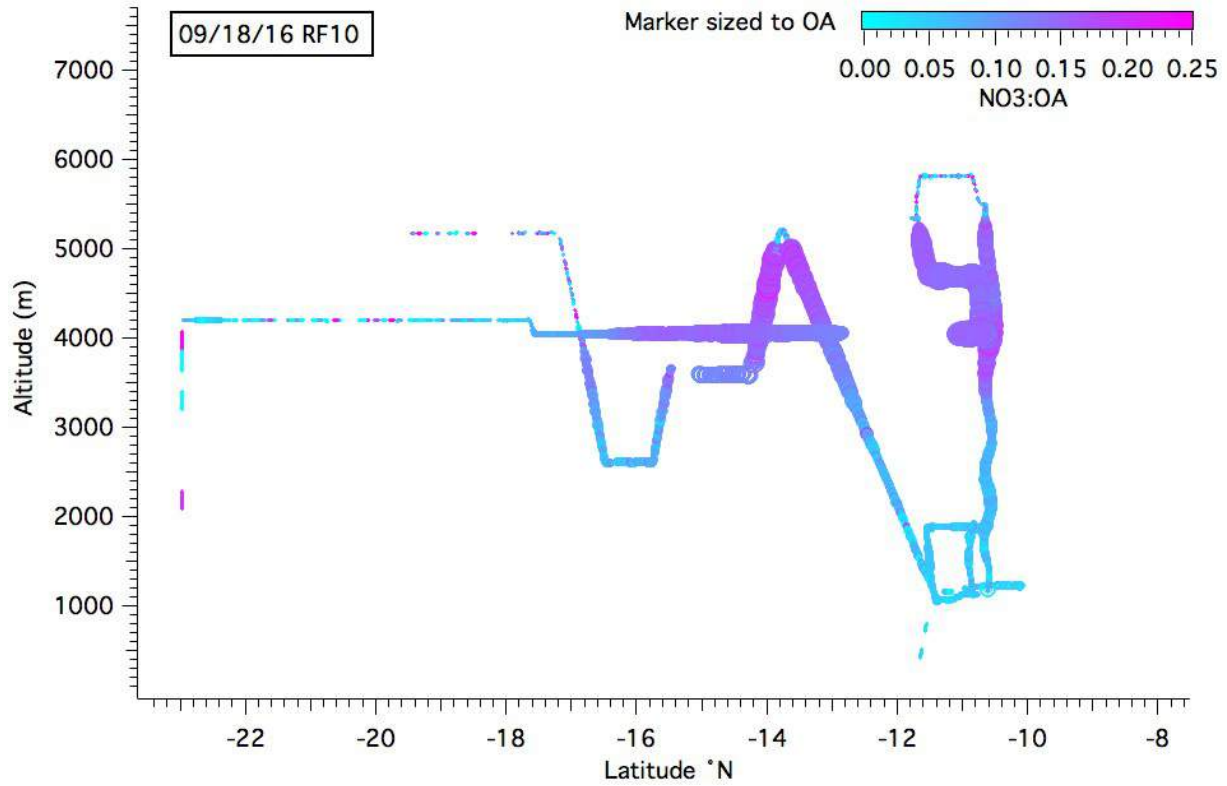


Figure 9. RF10 09/18/16

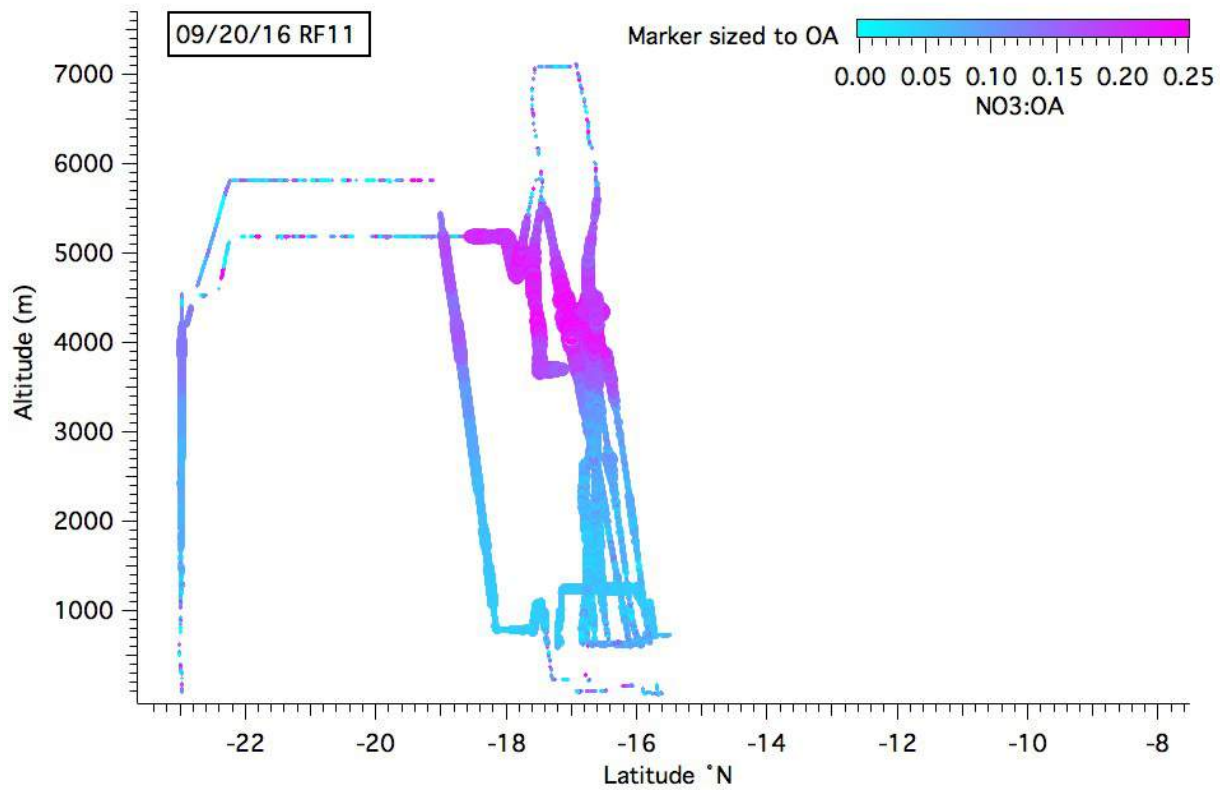


Figure 10. RF11 09/20/16

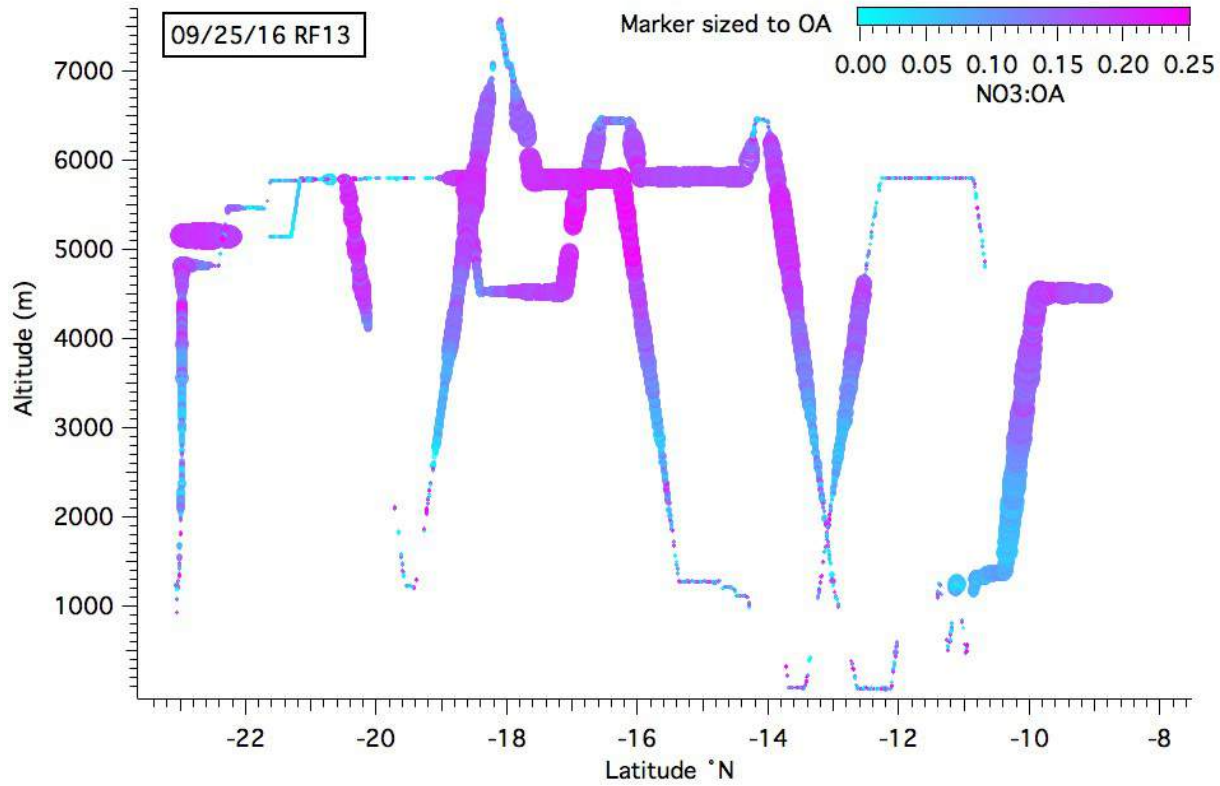


Figure 11. RF12 09/24/16

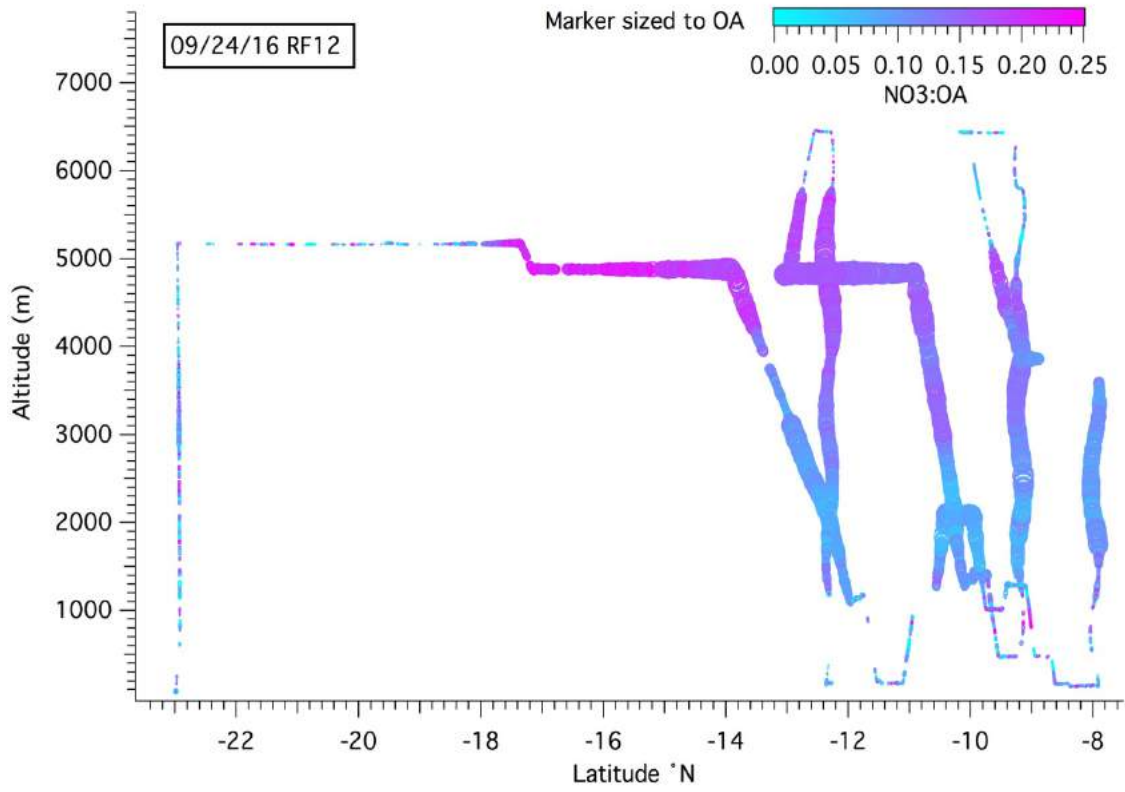


Figure 12. R13 09/25/16

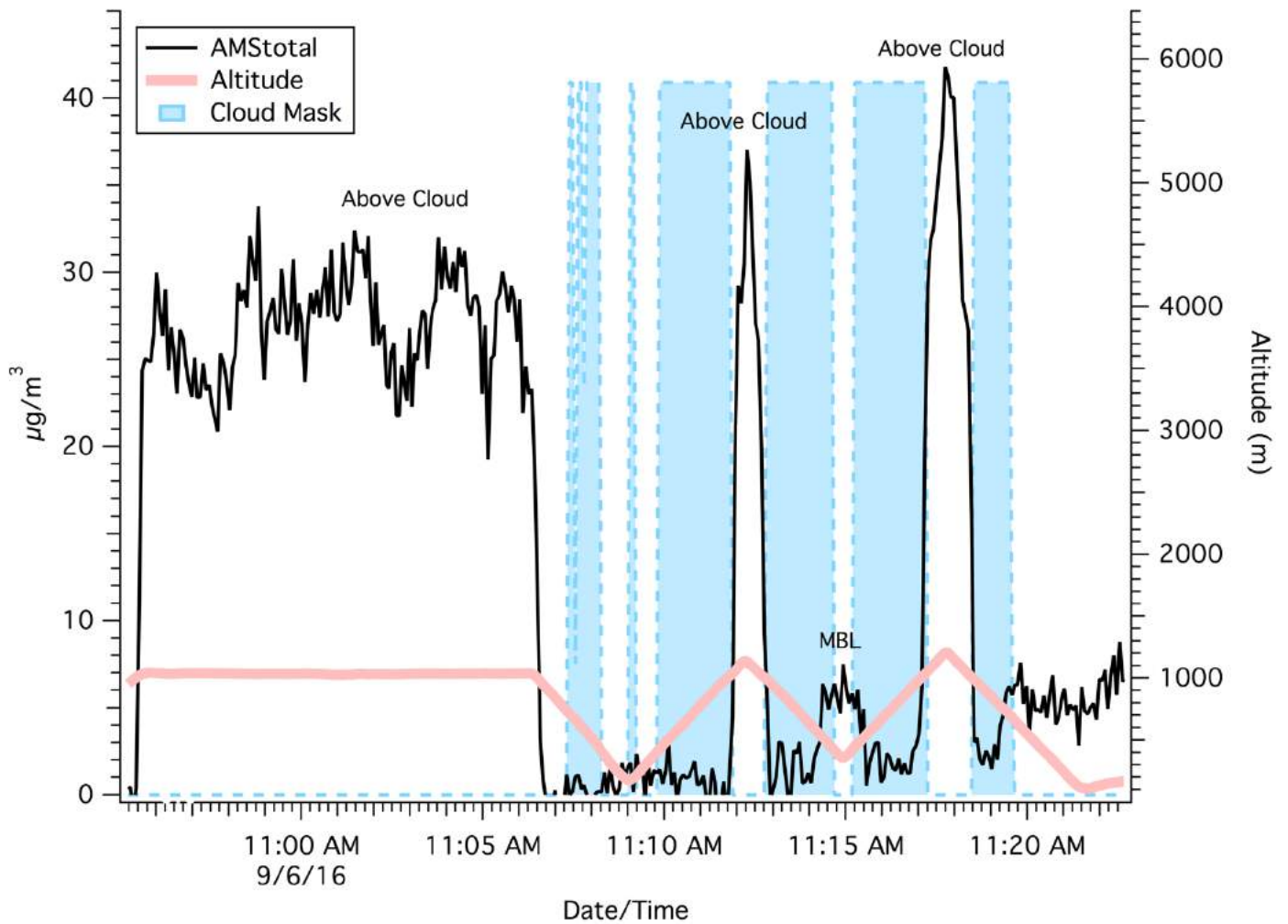


Figure 13. Example of aerosol right above cloud. Between 11:10am and 11:20am the plane flew 3 sawtooth formations where over the course of ~1000m the plane started from cloud top ~1200m, and dipped down to 200m, and then came back up to cloud top. The flight path can be seen in the altitude profile (pink). AMS total ($\mu\text{g}/\text{m}^3$) was observed as soon as the plane came out of cloud at 1200m. Periods of cloud contact are represented in blue boxes. The cloud mask (blue) is meant to indicate this was a period where we had aerosol interacting with the cloud. There was no gap between cloud top and BB aerosol.

Appendix C

Appendix C includes figures and tables from Chapter 4, Discussion, Section 4.1, Organic Aerosol

Figures 1-12: Van Krevelen Diagram. Only includes data for $OA > 12\mu\text{g}/\text{m}^3$. The marker is then sized to that criteria. $HC=a+b(O:C)$

Table C.1: Average Oxidation state for each flight where $OA > 12\mu\text{g}/\text{m}^3$

Table C.2: Average f44 and f60 values for each flight when $OA > 12\mu\text{g}/\text{m}^3$.

Figures 13-24: f44 vs f60 for each flight. Only includes data where $OA > 12\mu\text{g}/\text{m}^3$, the marker is then sized to that criteria.

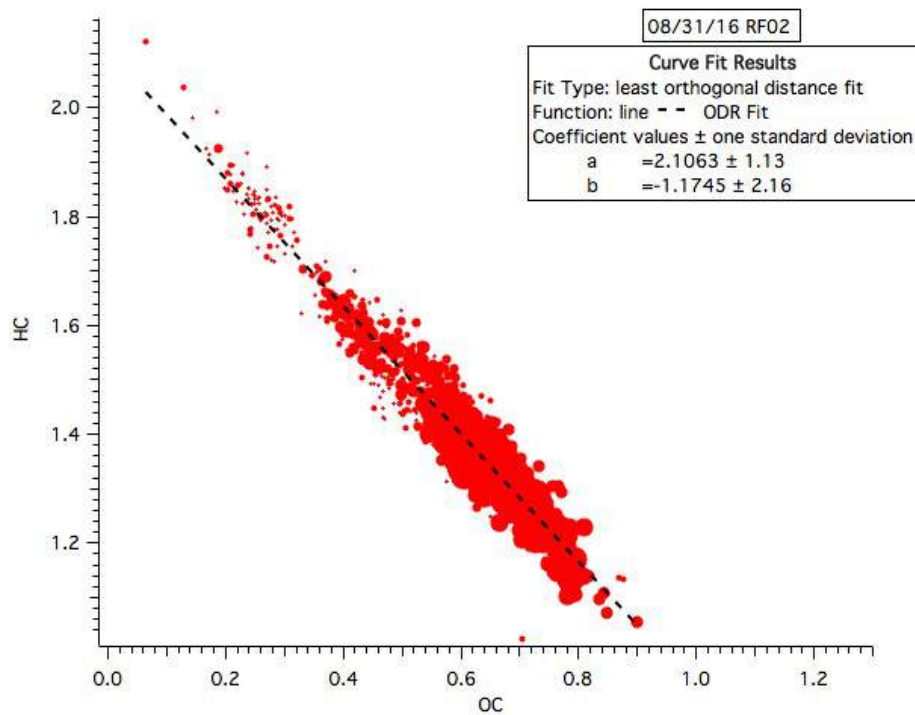


Figure 1. Van Krevelen Diagram RF02 08/31/16

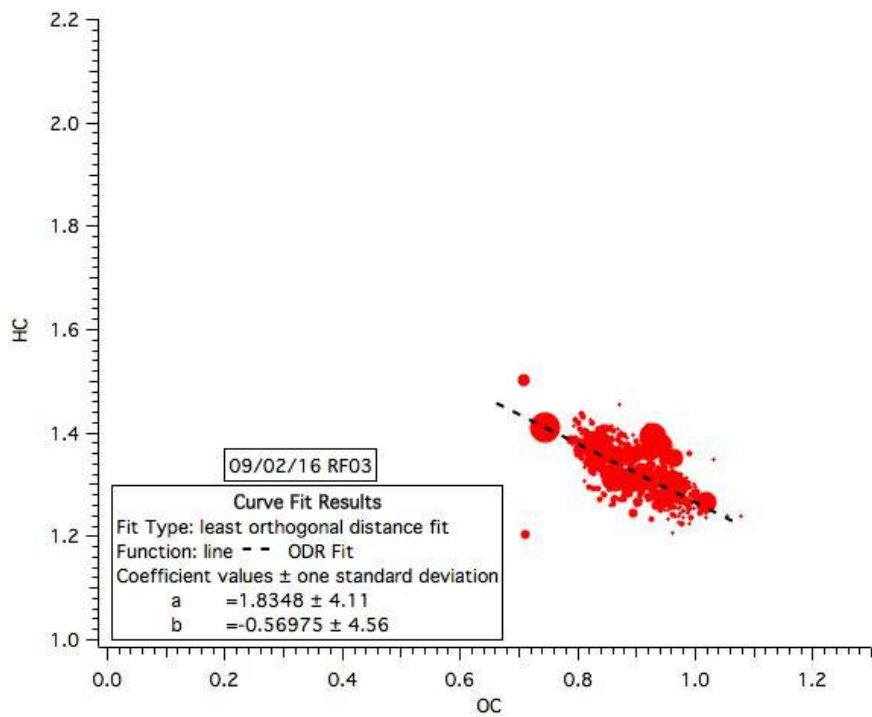


Figure 2. Van Krevelen Diagram RF03 09/02/16

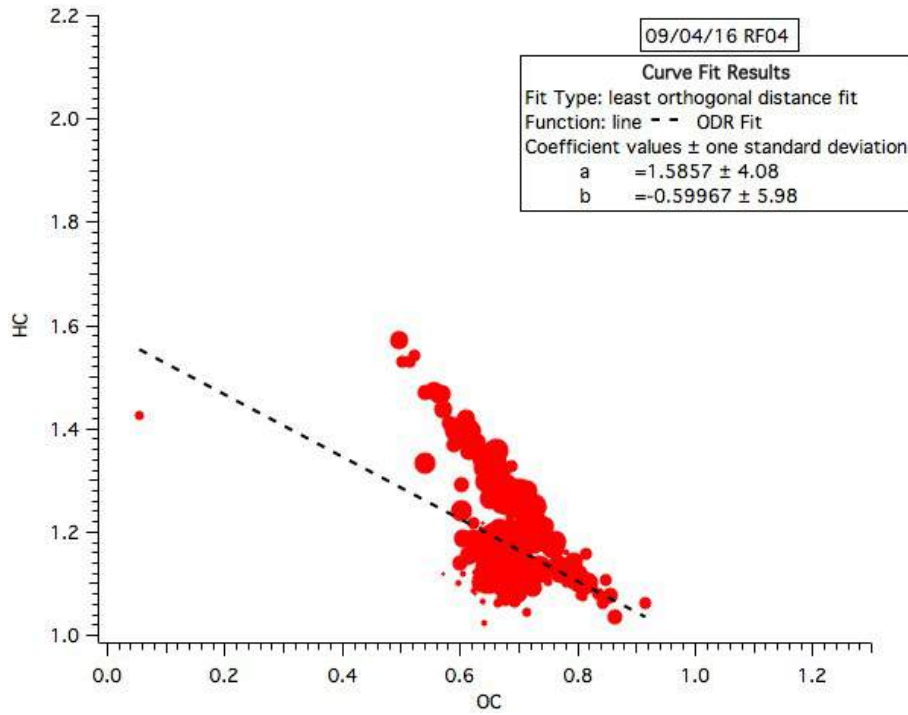


Figure 3. Van Krevelen Diagram RF04 09/04/16

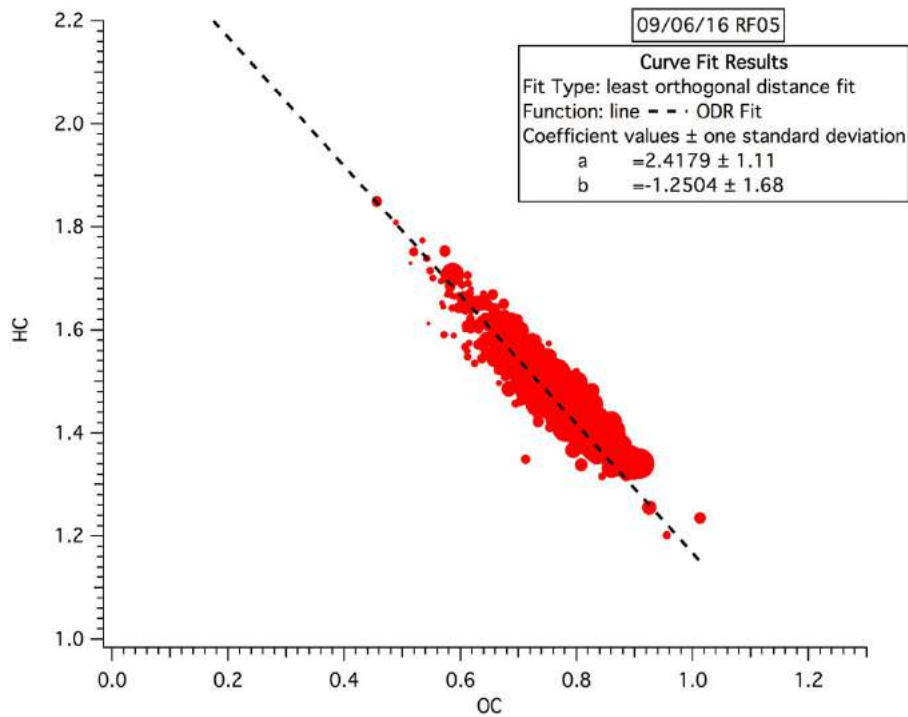


Figure 4. Van Krevelen Diagram RF05 09/06/16

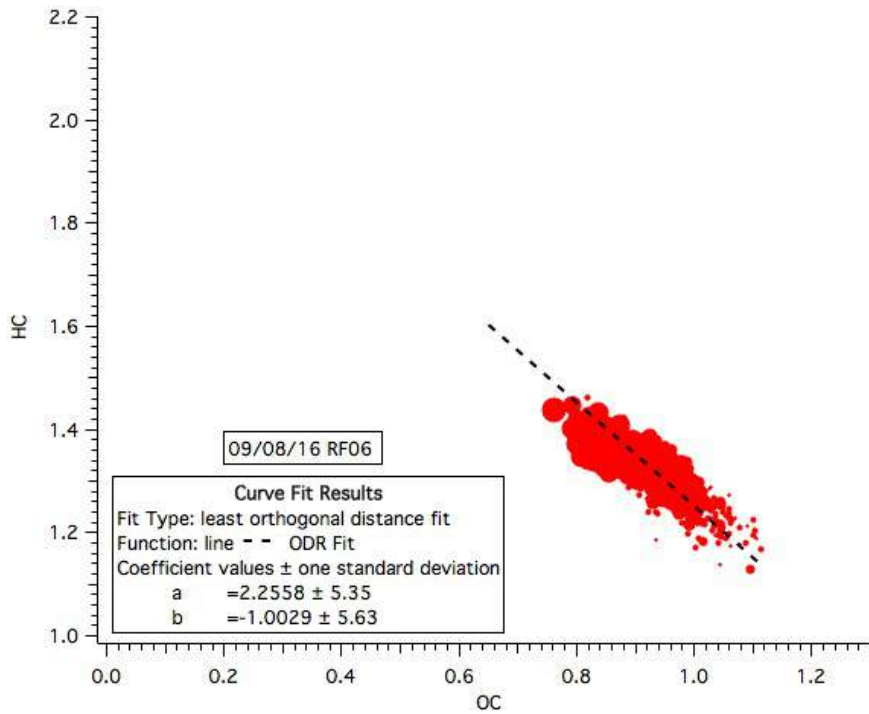


Figure 5. Van Krevelen Diagram RF06 09/08/16

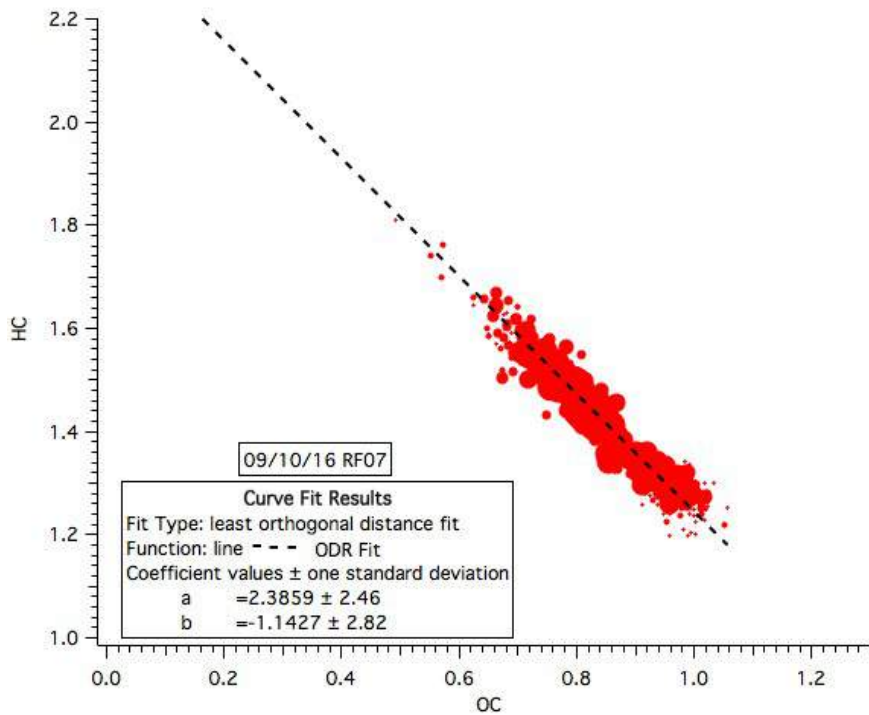


Figure 6. Van Krevelen Diagram RF07 09/10/16

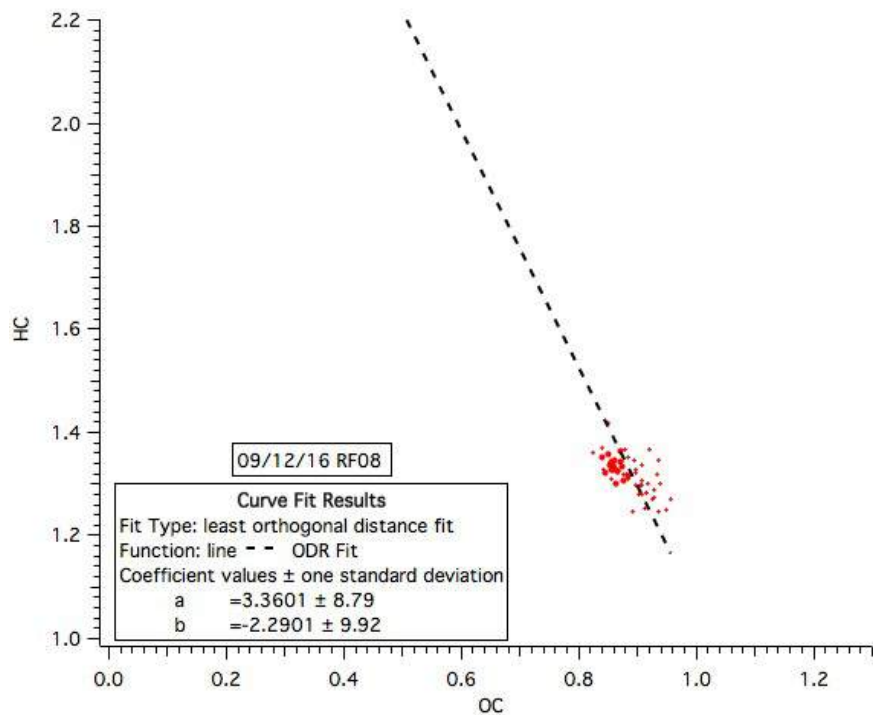


Figure 7. Van Krevelen Diagram RF08 09/12/16

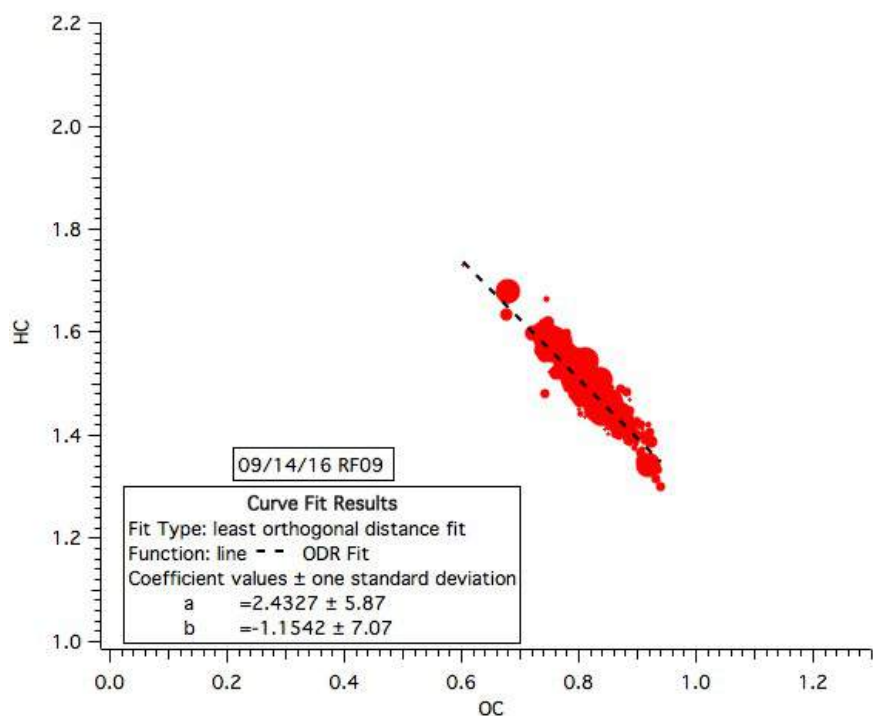


Figure 8. Van Krevelen Diagram RF09 09/14/16

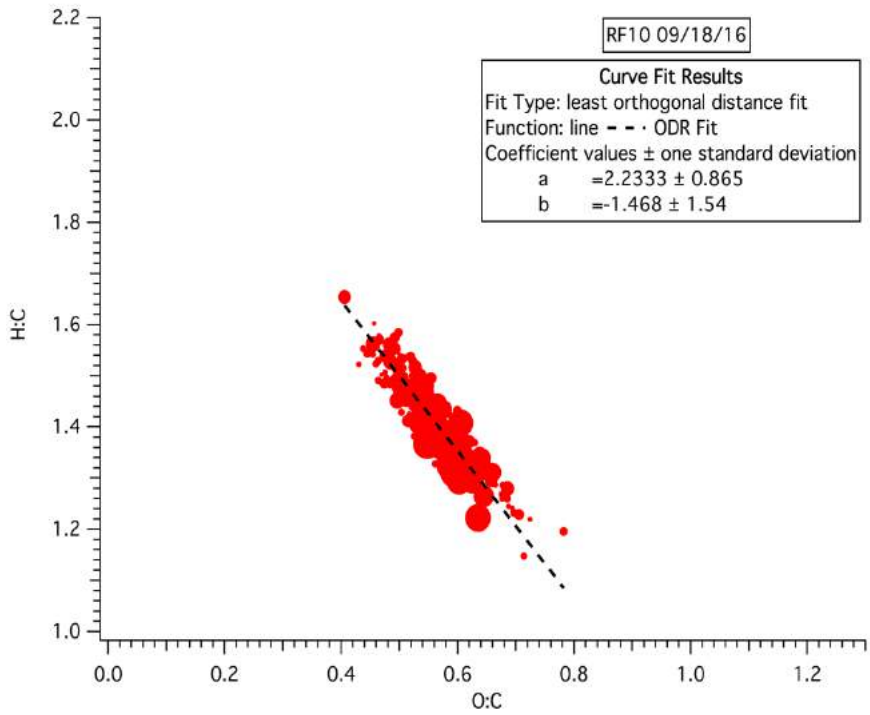


Figure 9. Van Krevelen Diagram RF10 09/18/16

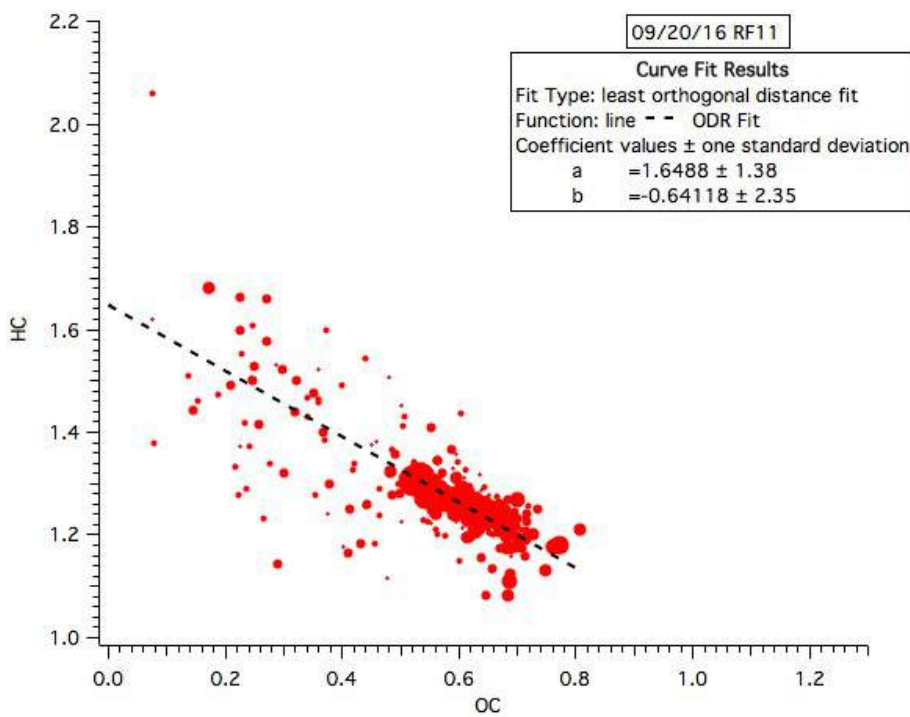


Figure 10. Van Krevelen Diagram RF11 09/20/16

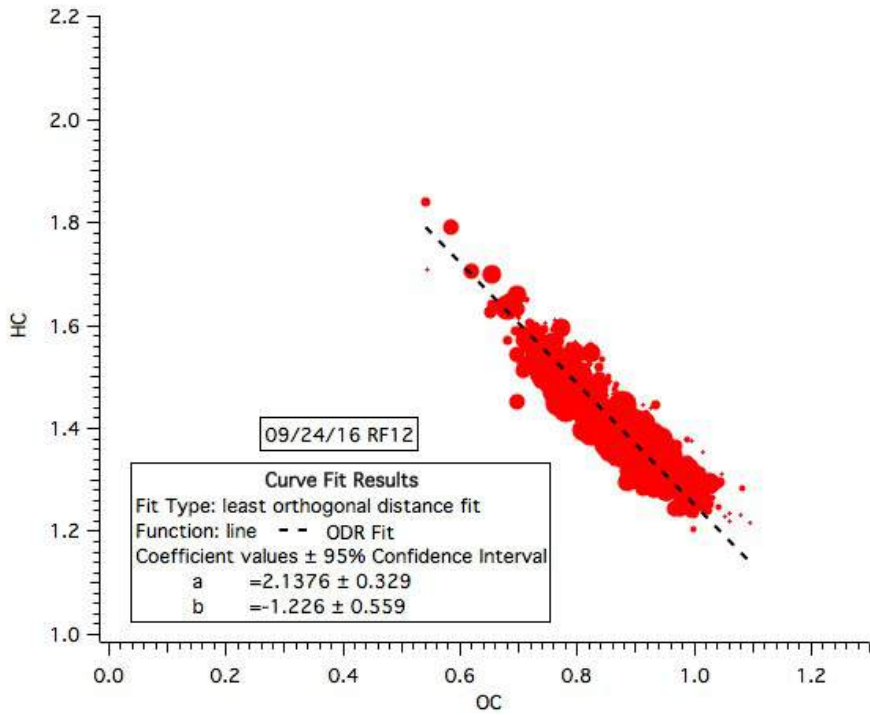


Figure 11. Van Krevelen Diagram RF12 09/24/16

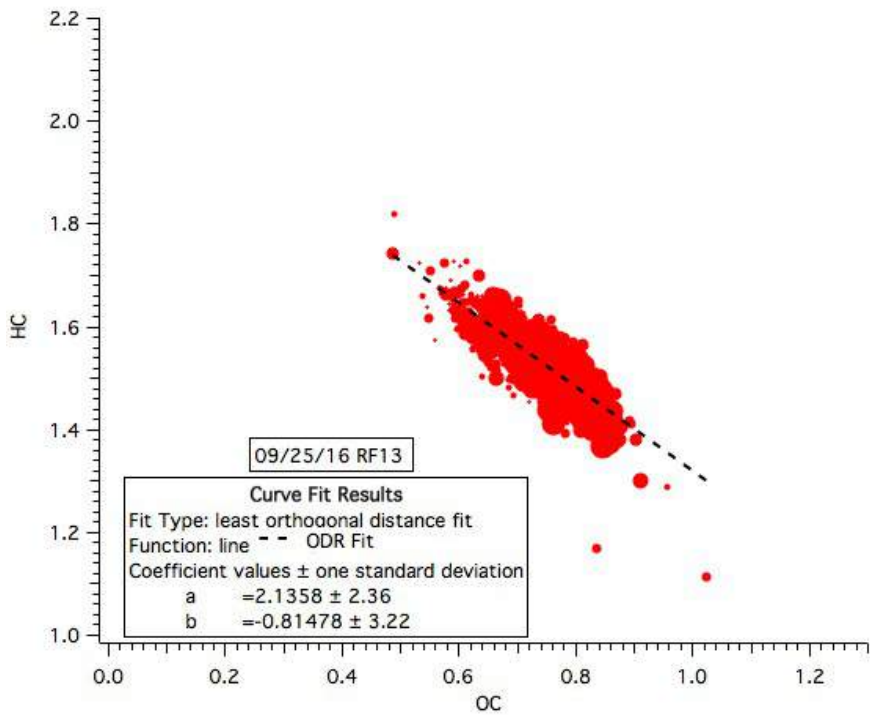


Figure 12. Van Krevelen Diagram RF13 09/25/16

Table C.1. Average Oxidation state for each flight where OA > 12 $\mu\text{g}/\text{m}^3$

Research Flight #	O _{Sc}
2	-0.06±0.58
3	0.46±0.17
4	.17±0.17
5	-0.03±0.21
6	0.53±0.19
7	0.31±0.08
8	-0.99±0.63
9	0.17±0.14
10	0.35±0.26
11	-0.17±0.46
12	0.29±0.32
13	-0.05±0.17

Table C.2 Average f44 and f60 values for each flight when OA >12 $\mu\text{g}/\text{m}^3$.

Research Flight #	F44	F60
02	0.209±0.019	0.007±0.007
03	0.212±0.028	0.016±0.180
04	0.219±0.019	0.005±0.004
05	0.210±0.027	0.006±0.0038
06	0.199±0.017	0.005±0.003
07	0.198±0.009	0.005±0.002
08	0.134±0.072	0.011±0.009
09	0.204±0.009	0.005±0.002
10	0.170±0.042	0.006±0.005
11	0.164±0.017	0.007±0.003
12	0.191±0.017	0.006±0.004
13	0.22±0.015	0.007±0.005

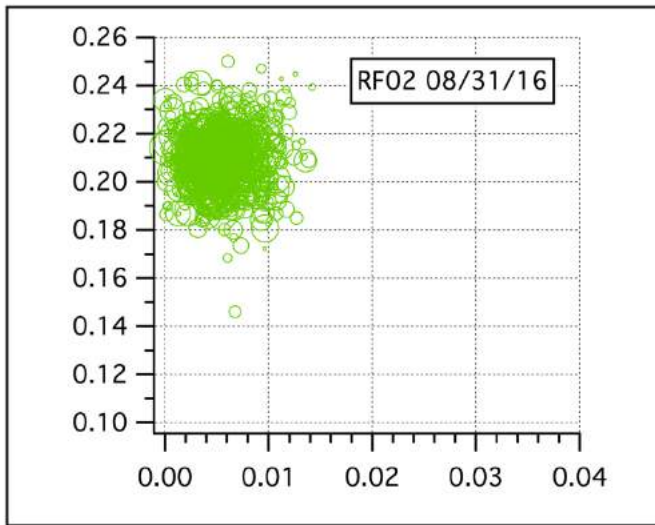


Figure 13. RF02 08/31/16

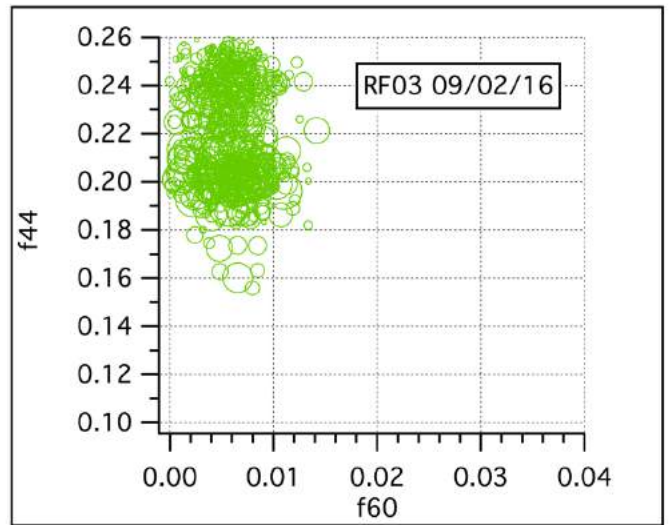


Figure 14. RF03 09/02/16

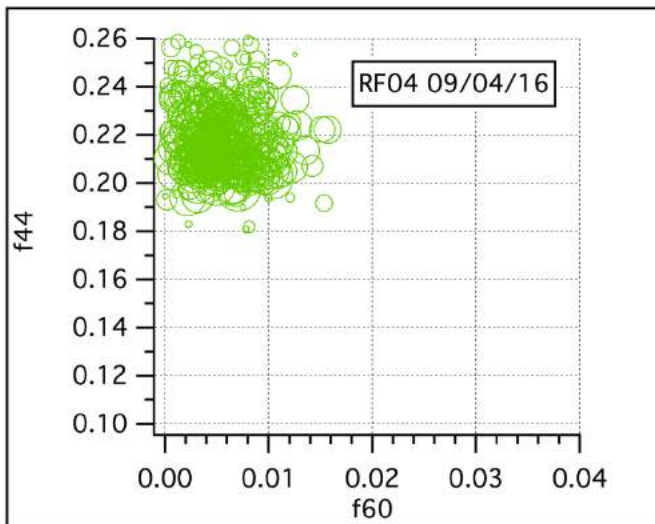


Figure 15. RF04 09/04/16

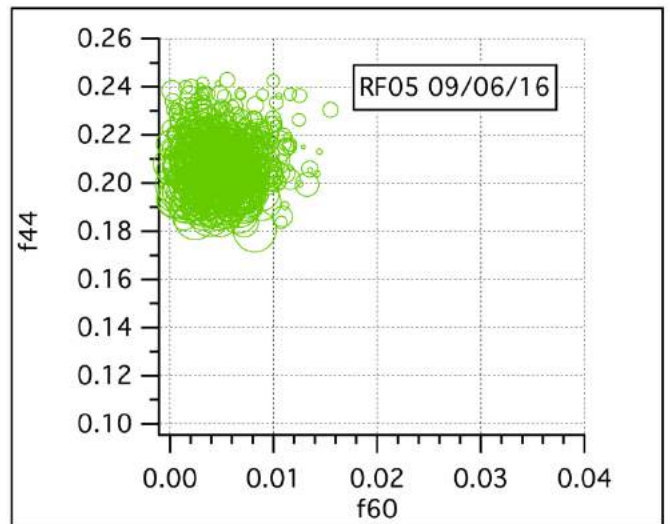


Figure 16. RF05 09/06/16

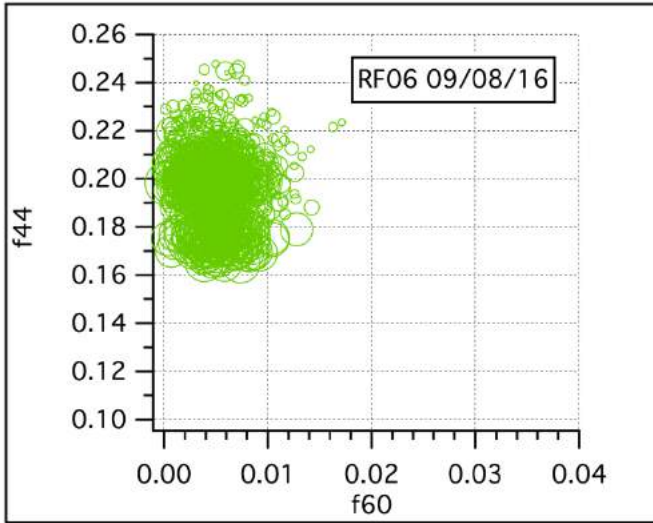


Figure 17. RF06 09/08/16

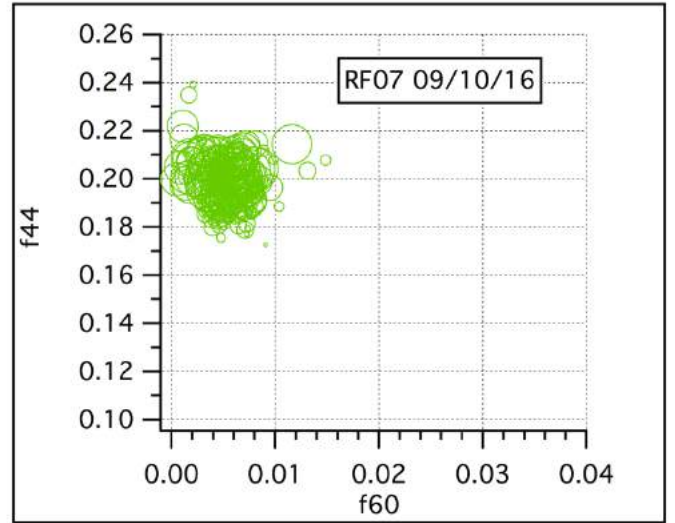


Figure 18. RF07 09/10/16

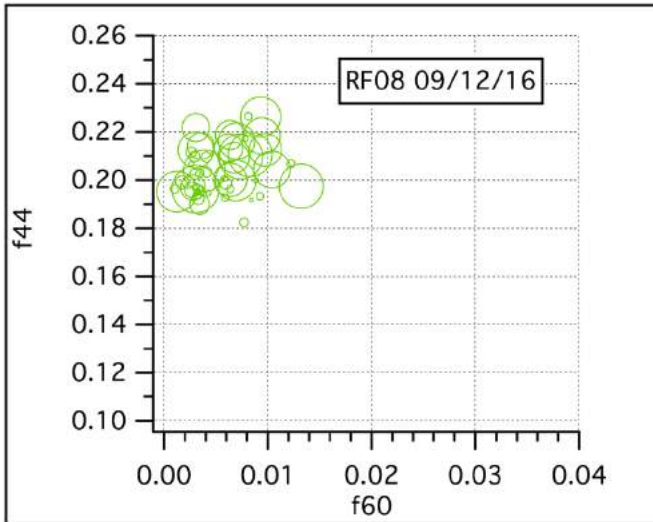


Figure 19. RF08 09/12/16

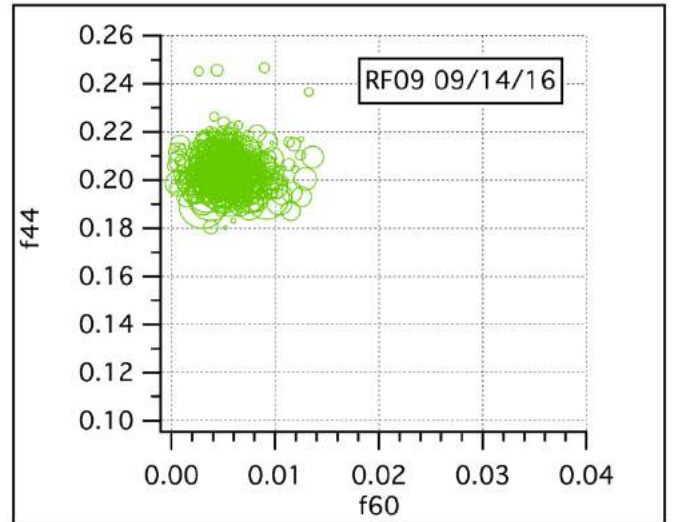


Figure 20. RF09 09/14/16

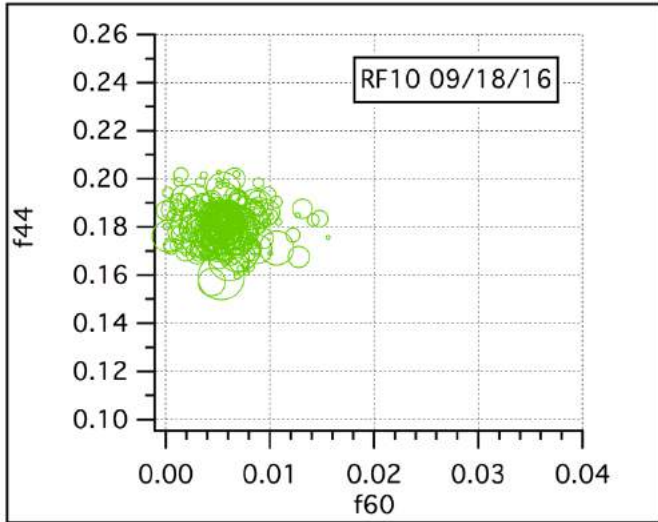


Figure 21. RF10 09/18/16

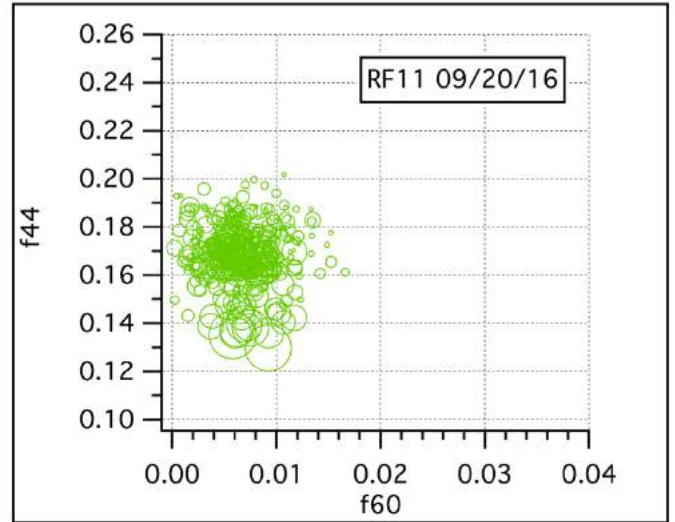


Figure 22. RF11 09/20/16

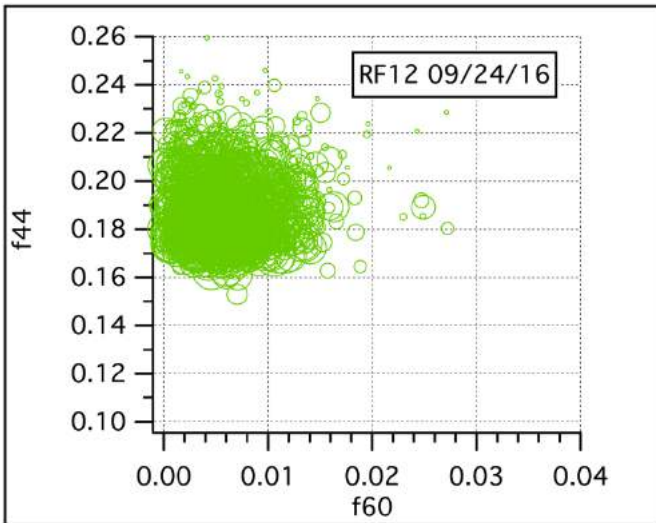


Figure 23. RF12 09/24/16

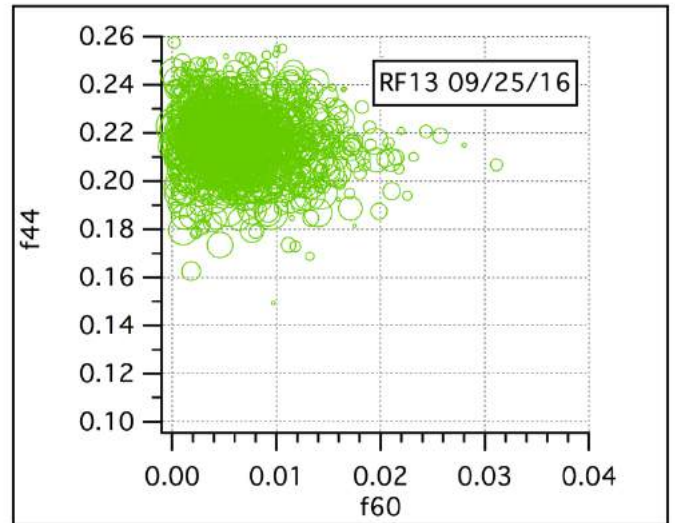


Figure 24. RF13 09/25/16

Appendix D

Appendix D includes figures and tables from Chapter 4, Discussion, Section 4.2, Other chemical tracers of biomass burning

Table D.1: Average MCE for all flights when $OA > 12\mu\text{g}/\text{m}^3$.

Table D.2: Relationship between BC ($\mu\text{g}/\text{m}^3$) and CO (ppbv) Calculated from a simple least squares fit.

Table D.3: Relationship between OA ($\mu\text{g}/\text{m}^3$) and CO (ppbv) Calculated from a simple least squares fit.

Table D.4: Relationship between OA ($\mu\text{g}/\text{m}^3$) and CO (ppbv) Calculated from a least orthogonal distance fit.

Table D.1. Average MCE for all flights when OA > 12 $\mu\text{g}/\text{m}^3$

Research Flight #	MCE
02	0.985 \pm 0.006
03	0.984 \pm 0.007
04	0.981 \pm 0.009
05	0.987 \pm 0.005
06	0.988 \pm 0.008
07	0.991 \pm 0.008
08	0.995 \pm 0.005
09	0.989 \pm 0.007
10	0.990 \pm 0.006
11	0.987 \pm 0.007
12	0.986 \pm 0.006
13	0.986 \pm 0.006

Table D.2. Relationship between BC ($\mu\text{g}/\text{m}^3$) and CO (ppbv) Calculated from a simple least squares fit

Research Flight #	BC:CO
2	0.0134
3	0.0127
4	0.0132
5	0.0124
6	0.0124
7	0.0097
8	0.0097
9	0.0107
10	0.0107
11	0.0117
12	0.0107
13	0.0108

Table D.3. Relationship between OA ($\mu\text{g}/\text{m}^3$) and CO (ppbv) Calculated from a simple least squares fit

Research Flight #	OA:CO
2	0.110
3	0.066
4	0.071
5	0.116
6	0.138
7	0.058
8	0.056
9	0.071
10	0.071
11	0.059
12	0.116
13	0.091

Table D.4. Relationship between OA ($\mu\text{g}/\text{m}^3$) and BC (ppbv) Calculated from a least orthogonal distance fit

Research Flight #	BC:OA
2	0.172
3	0.218
4	0.153
5	0.127
6	0.095
7	0.134
8	0.158
9	0.141
10	0.271
11	0.206
12	0.166
13	0.086

Appendix E

Appendix E includes figures and tables from Chapter 4, Discussion, Section 4.3, Aerosol acid/base balance

Figures 1-12: NH_4 molar ratio plotted against $(2 \cdot \text{SO}_4 + \text{NO}_3)$. Marker sized to $\text{OA} > 12 \mu\text{g}/\text{m}^3$.

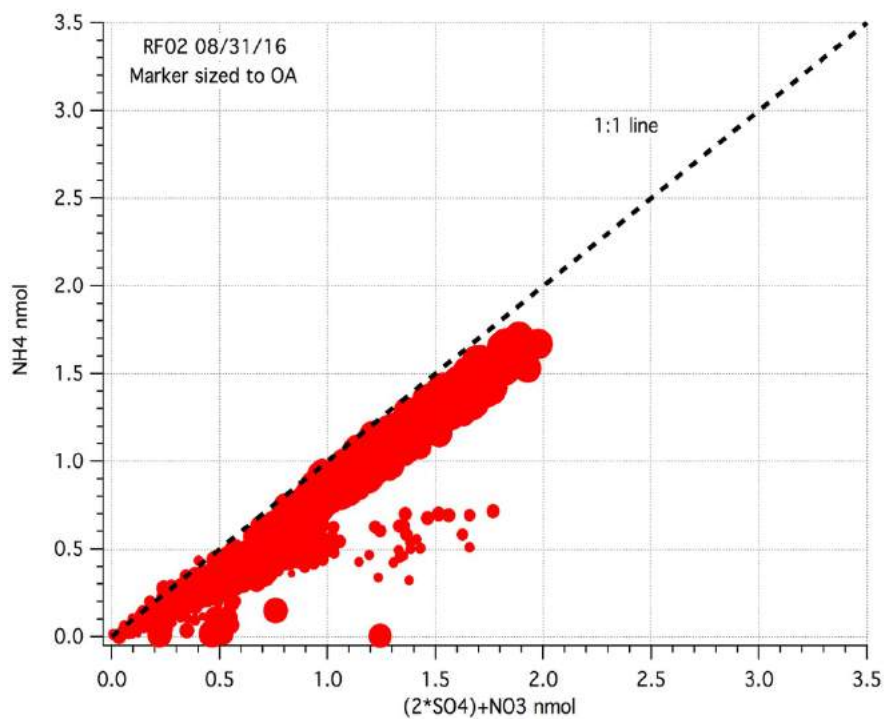


Figure 1. RF02 08/31/16

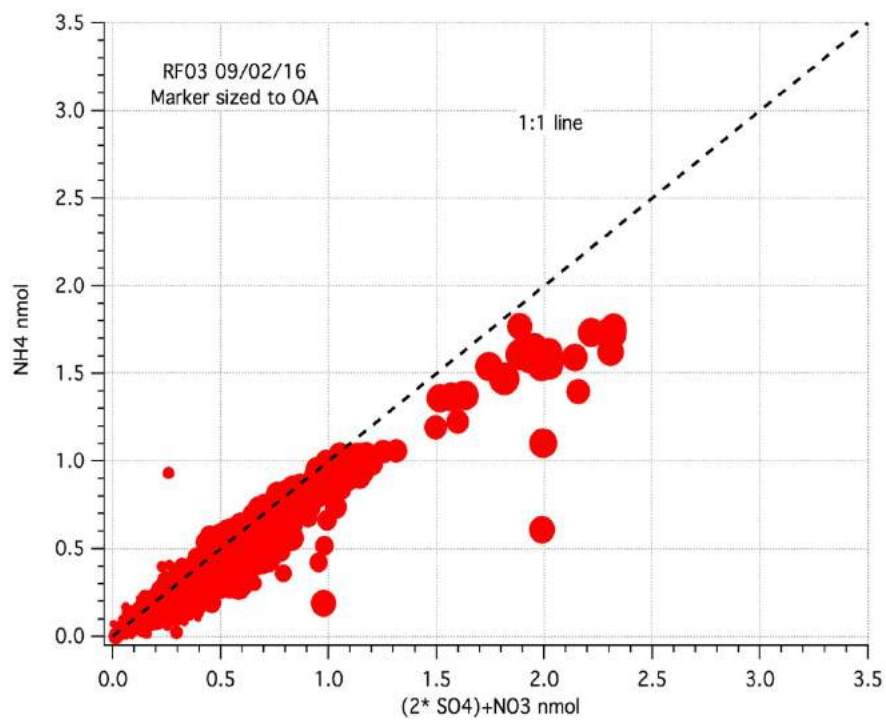


Figure 2. RF03 09/02/16

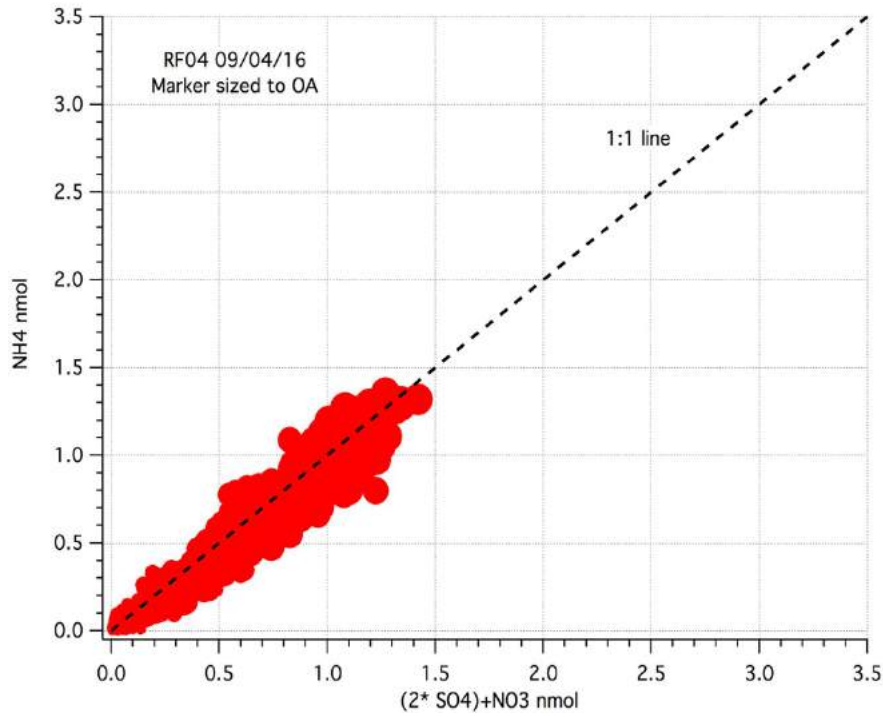


Figure 3. RF04 09/04/16

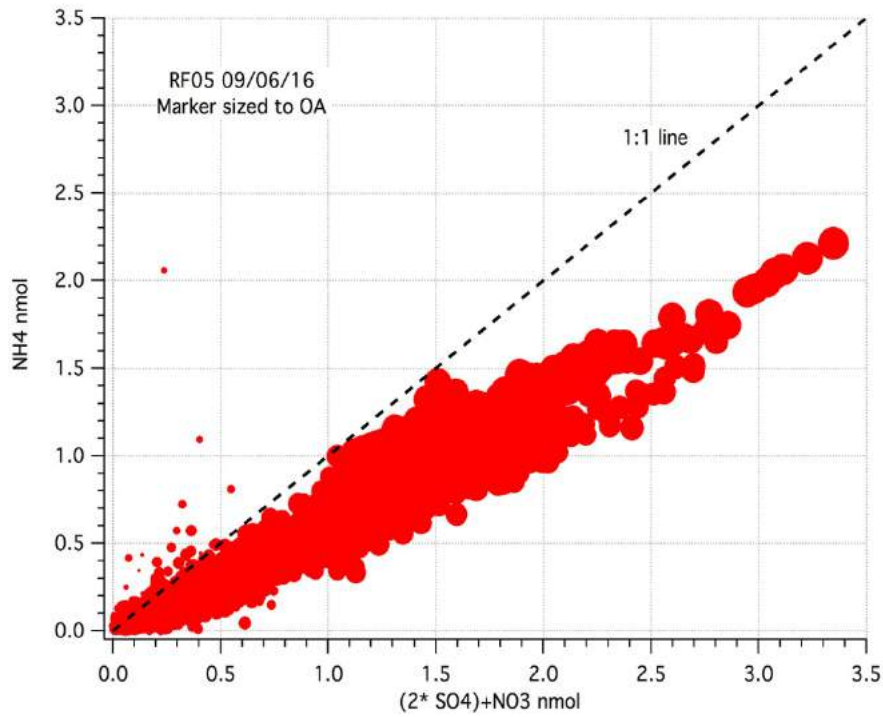


Figure 4. RF05 09/06/16

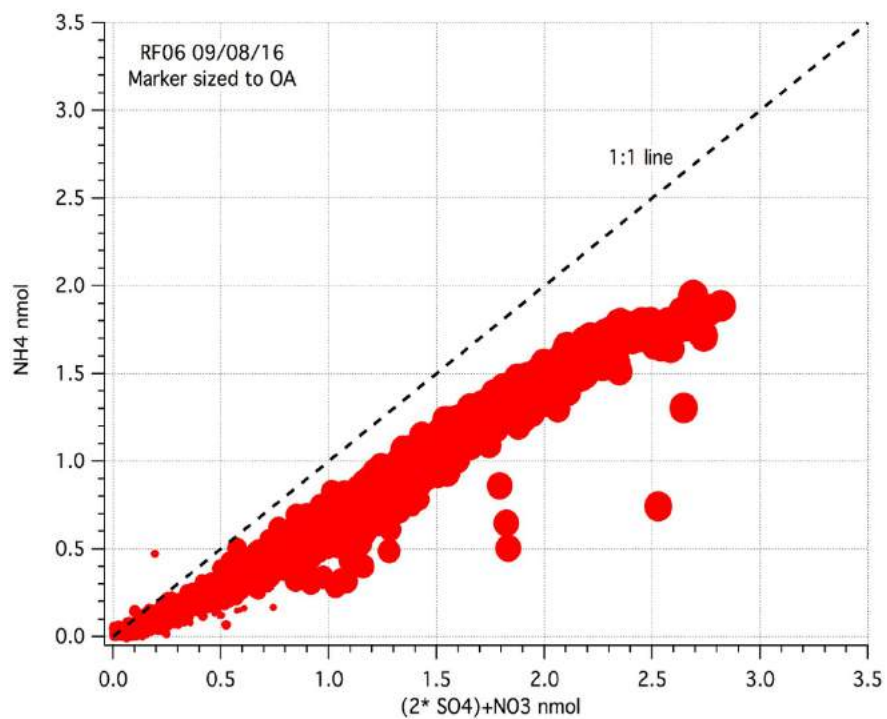


Figure 5. RF06 09/08/16

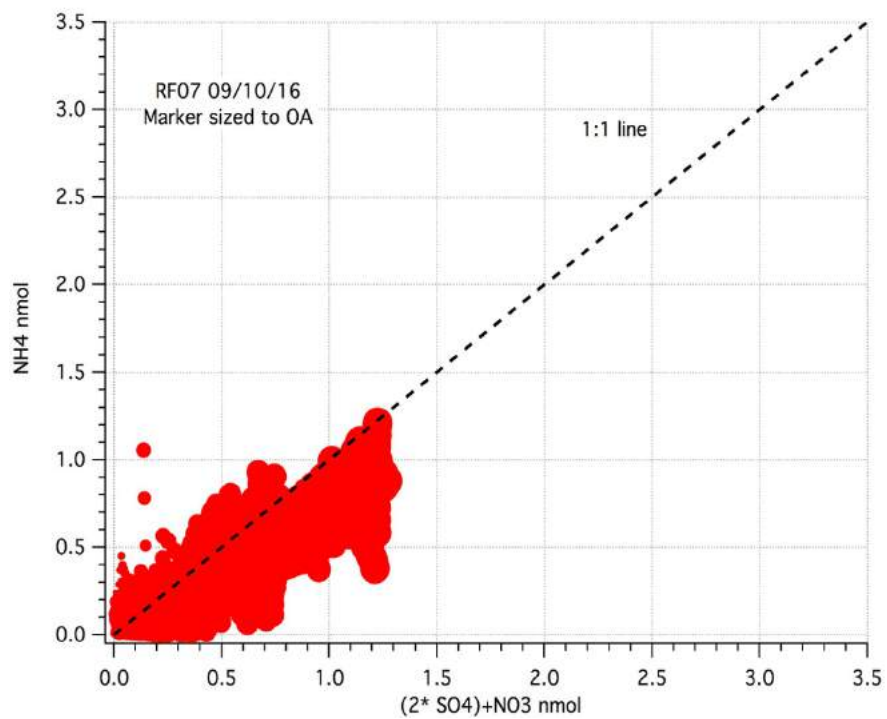


Figure 6. RF07 09/10/16

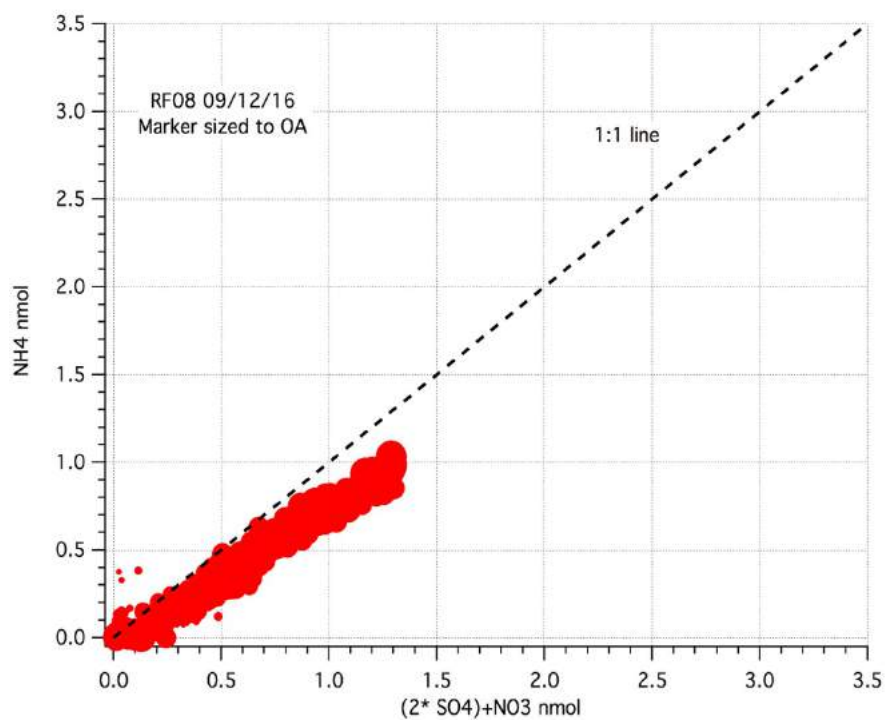


Figure 7. RF08 09/12/16

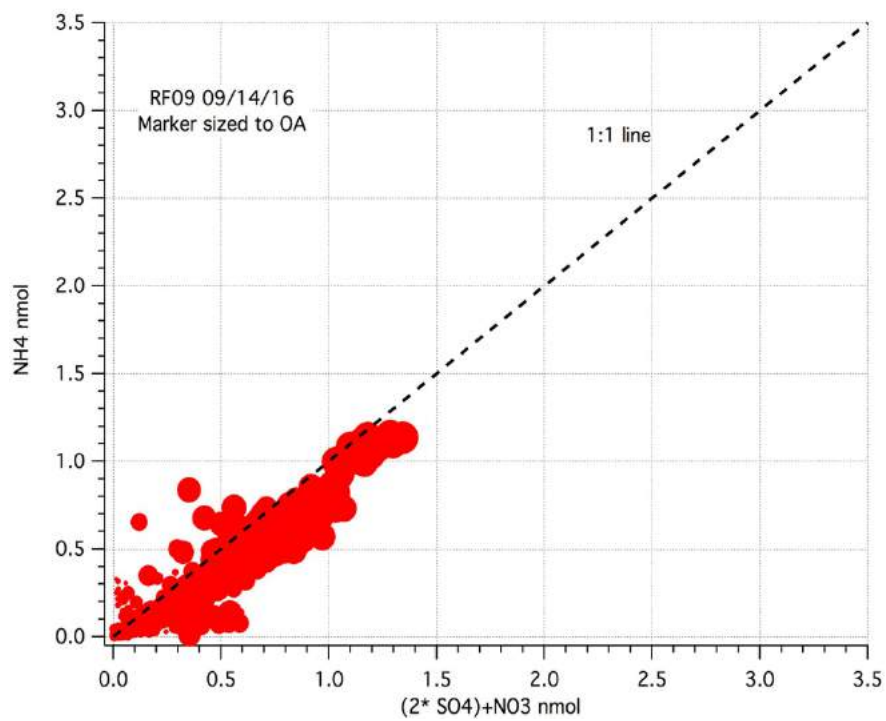


Figure 8. RF09 09/14/16

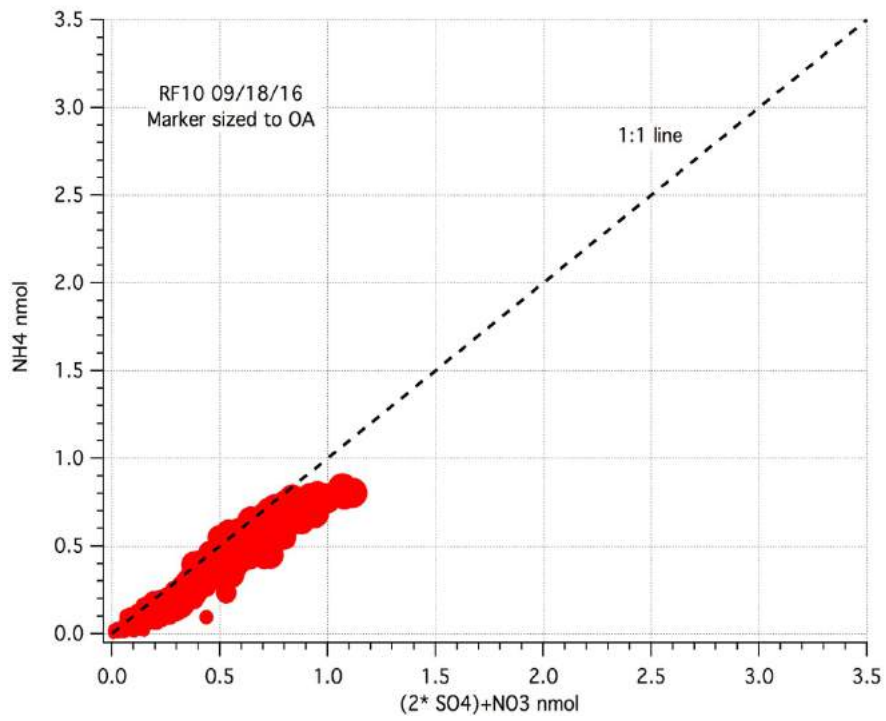


Figure 9. RF10 09/18/16

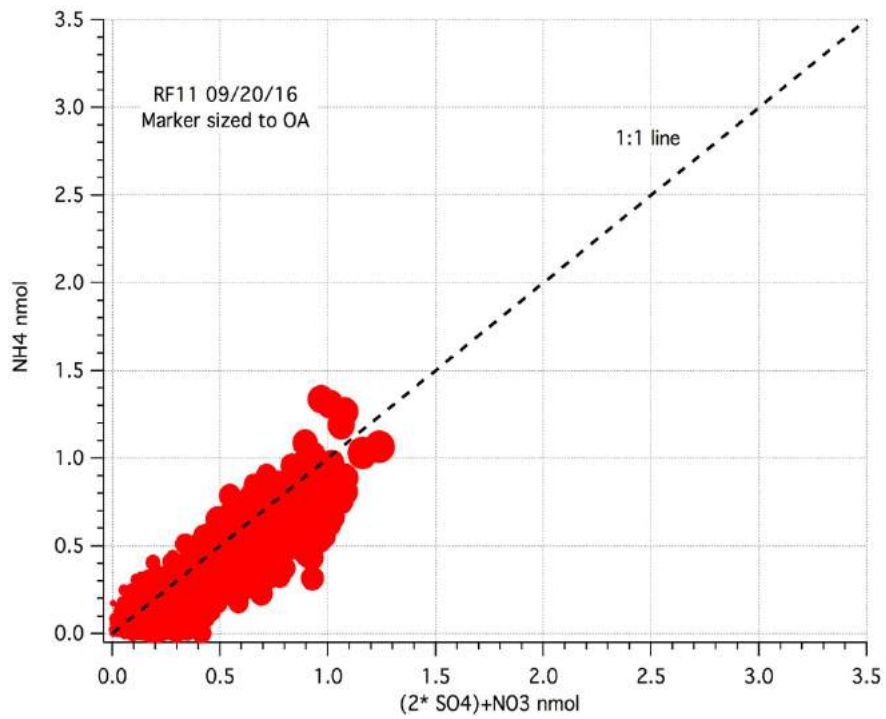


Figure 10. RF11 09/20/16

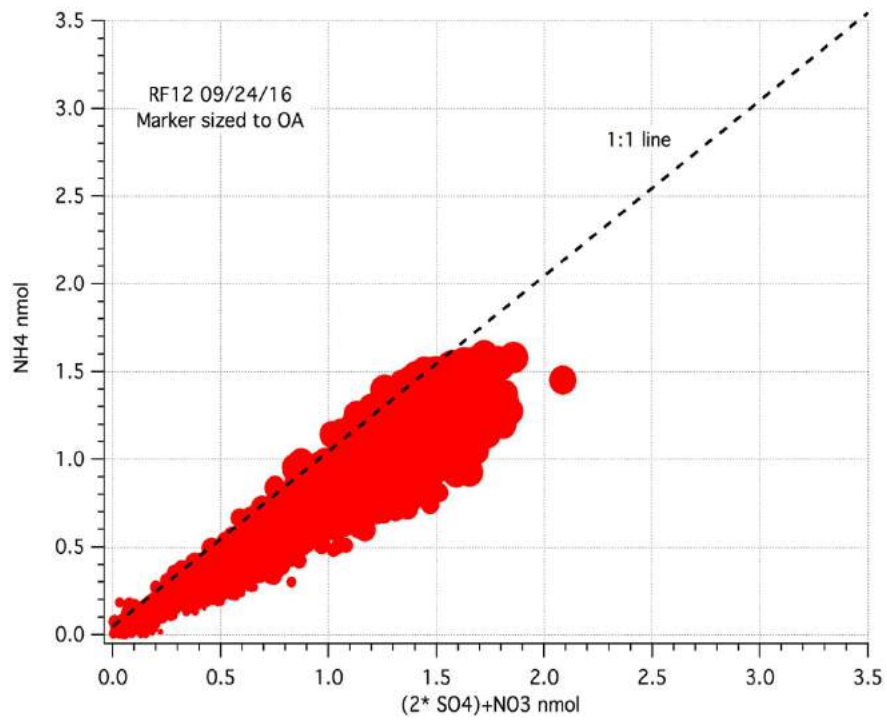


Figure 11. RF12 09/24/16

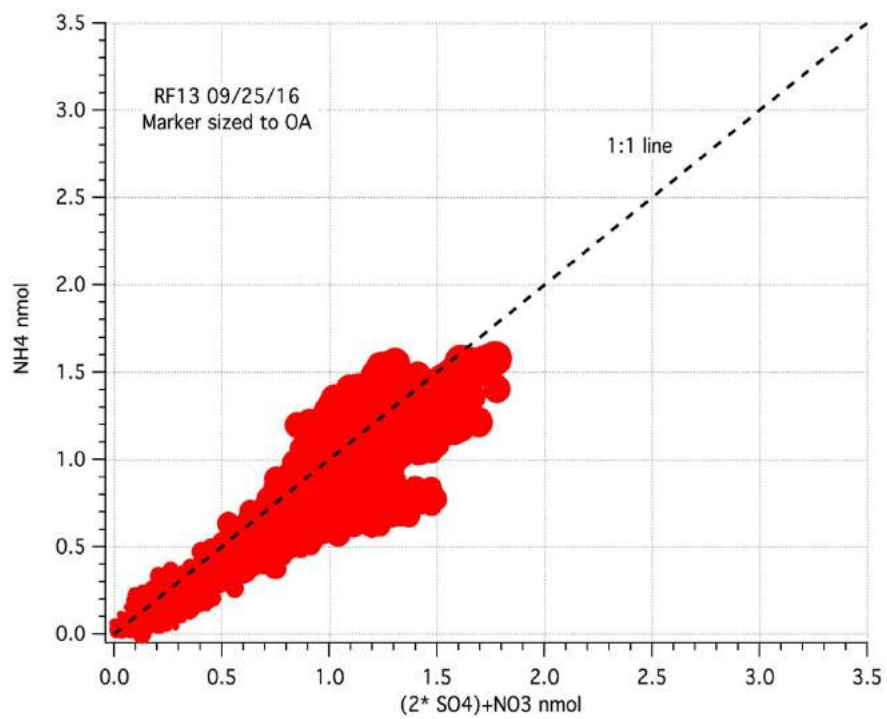


Figure 12. RF13 09/25/16

Appendix F

Appendix F includes figures and tables from Chapter 4, Discussion, Section 4.6, SAFARI 2000 Comparison

Table F.1: ER for Ozone from ORACLES where $OA > 12\mu\text{g}/\text{m}^3$

Table F.2: Comparison of SAFARI 2000 chemical properties to ORACLES 2016 chemical properties

Table F.1. ER for Ozone from ORACLES where OA > 12 $\mu\text{g}/\text{m}^3$

Research Flight #	ER Ozone
02	0.635 \pm 0.174
03	0.451 \pm 0.133
04	0.342 \pm 0.131
05	0.429 \pm 0.141
06	0.327 \pm 0.242
07	0.598 \pm 0.105
08	0.571 \pm 0.0935
09	0.368 \pm 0.0585
10	0.576 \pm 0.162
11	0.482 \pm 0.237
12	0.548 \pm 0.135
13	0.648 \pm 0.176

Table F.2. Average Aerosol concentrations and average chemical ratios from SAFARI 2000 and ORACLES 2016

Where	When	OA $\mu\text{g}/\text{m}^3$	SO ₄ $\mu\text{g}/\text{m}^3$	NH ₄ $\mu\text{g}/\text{m}^3$	NO ₃ $\mu\text{g}/\text{m}^3$	BC $\mu\text{g}/\text{m}^3$	CO ppbv	EC/OC
ORACLES SEA 2016 (1500m-3500m)	Aug-Sept 2016	10.22±9.49	1.91±1.69	0.71±0.65	1.11±1.14	1.34±0.96	188.46±76.98	0.13
SAFARI 2000 SEA (C-130)	Sept 2000	15-35	0.6-5.8	0.15±0.1	1.4±1.8	0.5-2.5	~100-200	0.11
Safari 2000 Mozambique (Convair-580)	Sept 2000	7.26±7.14	8.5±5.0	--	0.8±0.3	1.0±0.5	165±43	0.12
Safari 2000 Namibia (Convair-580)	Sept 2000	5.16	2.8	--	0.8	1.0	162±92	0.19
Safari 2000 Zambia (Convair-580)	Sept 2000	14.58	0.9±0.1	--	0.9±0.1	5.5±1.4	453±101	0.37
Safari 2000 Botswana (Convair-580)	Sept 2000	16.48±9.52	1.9±0.5	--	1.0±1.0	2.6±1.4	369±120	0.15
Safari 2000 South Africa (Convair-580)	Sept 2000	5.72±2.38	8.3±8.1	--	0.3±0.2	1.1±0.4	157±47	0.19

References

- Adler, G., et al. "Chemical, Physical, and Optical Evolution of Biomass Burning Aerosols: a Case Study." *Atmospheric Chemistry and Physics*, vol. 11, no. 4, 16 Feb. 2011, pp. 1491–1503., doi:10.5194/acp-11-1491-2011.
- Aiken, Allison C., et al. "O/C And OM/OC Ratios of Primary, Secondary, and Ambient Organic Aerosols with High-Resolution Time-of-Flight Aerosol Mass Spectrometry." *Environmental Science & Technology*, vol. 42, no. 12, May 2008, pp. 4478–4485., doi:10.1021/es703009q.
- Albrecht, B. A. "Aerosols, Cloud Microphysics, and Fractional Cloudiness." *Science*, vol. 245, no. 4923, 15 Apr. 1989, pp. 1227–1230., doi:10.1126/science.245.4923.1227.
- Bougiatioti, A., et al. "Cloud Condensation Nuclei Measurements in the Marine Boundary Layer of the Eastern Mediterranean: CCN Closure and Droplet Growth Kinetics." *Atmospheric Chemistry and Physics*, vol. 9, no. 18, 24 Mar. 2009, pp. 7053–7066., doi:10.5194/acp-9-7053-2009.
- Cai, Yong, et al. "Performance Characteristics of the Ultra High Sensitivity Aerosol Spectrometer for Particles between 55 and 800nm: Laboratory and Field Studies." *Journal of Aerosol Science*, vol. 39, no. 9, Sept. 2008, pp. 759–769., doi:10.1016/j.jaerosci.2008.04.007.
- Chylek, P., and J. Wong. "Effect of Absorbing Aerosols on Global Radiation Budget." *Geophysical Research Letters*, vol. 22, no. 8, 15 Apr. 1995, pp. 929–931., doi:10.1029/95GL00800.

- Clarke, A. D. "Particle Nucleation in the Tropical Boundary Layer and Its Coupling to Marine Sulfur Sources." *Science*, vol. 282, no. 5386, 2 Feb. 1998, pp. 89–92., doi:10.1126/science.282.5386.89.
- Collier, Sonya, et al. "Regional Influence of Aerosol Emissions from Wildfires Driven by Combustion Efficiency: Insights from the BBOP Campaign." *Environmental Science & Technology*, vol. 50, no. 16, 26 July 2016, pp. 8613–8622., doi:10.1021/acs.est.6b01617.
- Cubison, M. J., et al. "Effects of Aging on Organic Aerosol from Open Biomass Burning Smoke in Aircraft and Laboratory Studies." *Atmospheric Chemistry and Physics*, vol. 11, no. 23, 5 Dec. 2011, pp. 12049–12064., doi:10.5194/acp-11-12049-2011.
- Decarlo, Peter F., et al. "Field-Deployable, High-Resolution, Time-of-Flight Aerosol Mass Spectrometer." *Analytical Chemistry*, vol. 78, no. 24, 11 Nov. 2006, pp. 8281–8289., doi:10.1021/ac061249n.
- Deng, Z. Z., et al. "An Examination of Parameterizations for the CCN Number Concentration Based on in Situ Measurements of Aerosol Activation Properties in the North China Plain." *Atmospheric Chemistry and Physics*, vol. 13, no. 13, 1 July 2013, pp. 6227–6237., doi:10.5194/acp-13-6227-2013.
- Drewnick, F., et al. "Intercomparison and Evaluation of Four Semi-Continuous PM_{2.5} Sulfate Instruments." *Atmospheric Environment*, vol. 37, no. 24, Aug. 2003, pp. 3335–3350., doi:10.1016/s1352-2310(03)00351-0.
- Eck, T. F., et al. "A Seasonal Trend of Single Scattering Albedo in Southern African Biomass-Burning Particles: Implications for Satellite Products and Estimates of Emissions for the World's Largest Biomass-Burning Source." *Journal of*

Geophysical Research: Atmospheres, vol. 118, no. 12, 19 May 2013, pp. 6414–6432., doi:10.1002/jgrd.50500.

Formenti, P., et al. “Inorganic and Carbonaceous Aerosols during the Southern African Regional Science Initiative (SAFARI 2000) Experiment: Chemical Characteristics, Physical Properties, and Emission Data for Smoke from African Biomass Burning.” *Journal of Geophysical Research: Atmospheres*, vol. 108, no. D13, 25 Mar. 2003, doi:10.1029/2002jd002408.

Forrister, Haviland, et al. “Evolution of Brown Carbon in Wildfire Plumes.” *Geophysical Research Letters*, vol. 42, no. 11, 3 May 2015, pp. 4623–4630., doi:10.1002/2015gl063897.

Freitag, S., et al. “Combining Airborne Gas and Aerosol Measurements with HYSPLIT: a Visualization Tool for Simultaneous Evaluation of Air Mass History and Back Trajectory Consistency.” *Atmospheric Measurement Techniques*, vol. 7, no. 1, 14 Jan. 2014, pp. 107–128., doi:10.5194/amt-7-107-2014.

Gouw, Joost De, and Jose L. Jimenez. “Evolution of Organic Aerosols in the Atmosphere.” *Environmental Science & Technology*, vol. 43, no. 20, 2009, pp. 7614–7618., doi:10.1021/es9006004.

Grell, Georg A., et al. “Fully Coupled ‘Online’ Chemistry within the WRF Model.” *Atmospheric Environment*, vol. 39, no. 37, Dec. 2005, pp. 6957–6975., doi:10.1016/j.atmosenv.2005.04.027.

Gysel, M., et al. “Effective Density of Aquadag and Fullerene Soot Black Carbon Reference Materials Used for SP2 Calibration.” *Atmospheric Measurement*

Techniques, vol. 4, no. 12, 22 Dec. 2011, pp. 2851–2858., doi:10.5194/amt-4-2851-2011.

Haywood, Jim M., et al. “The Mean Physical and Optical Properties of Regional Haze Dominated by Biomass Burning Aerosol Measured from the C-130 Aircraft during SAFARI 2000.” *Journal of Geophysical Research: Atmospheres*, vol. 108, no. D13, 18 Feb. 2003, doi:10.1029/2002jd002226.

Heald, C. L., et al. “A Simplified Description of the Evolution of Organic Aerosol Composition in the Atmosphere.” *Geophysical Research Letters*, vol. 37, no. 8, 22 Apr. 2010, doi:10.1029/2010gl042737.

Hennigan, C. J., et al. “Chemical and Physical Transformations of Organic Aerosol from the Photo-Oxidation of Open Biomass Burning Emissions in an Environmental Chamber.” *Atmospheric Chemistry and Physics Discussions*, vol. 11, no. 4, 18 Mar. 2011, pp. 11995–12037., doi:10.5194/acpd-11-11995-2011.

Hodzic, Alma, et al. “Rethinking the Global Secondary Organic Aerosol (SOA) Budget: Stronger Production, Faster Removal, Shorter Lifetime.” *Atmospheric Chemistry and Physics*, vol. 16, no. 12, 29 June 2016, pp. 7917–7941., doi:10.5194/acp-16-7917-2016.

Hudson, James G. “Cloud Condensation Nuclei near Marine Cumulus.” *Journal of Geophysical Research: Atmospheres*, vol. 98, no. D2, 20 May 1993, pp. 2693–2702., doi:10.1029/92jd02169.

Huebert, B. J., et al. “Airborne Aerosol Inlet Passing Efficiency Measurement.” *Journal of Geophysical Research*, vol. 95, no. D10, Sept. 1990, pp. 16369–16381., doi:10.1029/jd095id10p16369.

- Huffman, J. Alex, et al. "Design, Modeling, Optimization, and Experimental Tests of a Particle Beam Width Probe for the Aerodyne Aerosol Mass Spectrometer." *Aerosol Science and Technology*, vol. 39, no. 12, Apr. 2005, pp. 1143–1163., doi:10.1080/02786820500423782.
- Jacobson, Mark Z. "Effects of Biomass Burning on Climate, Accounting for Heat and Moisture Fluxes, Black and Brown Carbon, and Cloud Absorption Effects." *Journal of Geophysical Research: Atmospheres*, vol. 119, no. 14, 21 July 2014, pp. 8980–9002., doi:10.1002/2014jd021861.
- Jimenez , Jose L, et al. "Evolution of Organic Aerosols in the Atmosphere." *Science*, vol. 326, no. 5959, 11 Dec. 2009, pp. 1525–1529., doi:10.1126/science.1180353.
- Jolleys, Matthew D., et al. "Organic Aerosol Emission Ratios from the Laboratory Combustion of Biomass Fuels." *Journal of Geophysical Research: Atmospheres*, vol. 119, no. 22, 26 Oct. 2014, doi:10.1002/2014jd021589.
- Kroll, Jesse H., et al. "Carbon Oxidation State as a Metric for Describing the Chemistry of Atmospheric Organic Aerosol." *Nature Chemistry*, vol. 3, no. 2, 9 Jan. 2011, pp. 133–139., doi:10.1038/nchem.948.
- Lagzi , Istvan, et al. *Atmospheric Chemistry* . Eötvös Loránd University Faculty of Science Institute of Geography and Earth Science, 2013, hgpu.org/?p=11960.
- Lee, Taehyoung, et al. "Chemical Smoke Marker Emissions During Flaming and Smoldering Phases of Laboratory Open Burning of Wildland Fuels." *Aerosol Science and Technology*, vol. 44, no. 9, 9 Aug. 2010, pp. i-v., doi:10.1080/02786826.2010.499884.

- Loo, Sjaak Van, and Jaap Koppejan. *The Handbook of Biomass Combustion and Co-Firing*. Earthscan, 2008.
- Mcnaughton, Cameron S., et al. "Results from the DC-8 Inlet Characterization Experiment (DICE): Airborne Versus Surface Sampling of Mineral Dust and Sea Salt Aerosols." *Aerosol Science and Technology*, vol. 41, no. 2, 14 Nov. 2007, pp. 136–159., doi:10.1080/02786820601118406.
- Moosmaller, H., and C.m. Sorensen. "Small and Large Particle Limits of Single Scattering Albedo for Homogeneous, Spherical Particles." *Journal of Quantitative Spectroscopy and Radiative Transfer*, vol. 204, Jan. 2018, pp. 250–255., doi:10.1016/j.jqsrt.2017.09.029.
- Ng, N. L., et al. "Changes in Organic Aerosol Composition with Aging Inferred from Aerosol Mass Spectra." *Atmospheric Chemistry and Physics Discussions*, vol. 11, no. 3, 2 July 2011, pp. 7095–7112., doi:10.5194/acpd-11-7095-2011.
- Petters, M. D., and S. M. Kreidenweis. "A Single Parameter Representation of Hygroscopic Growth and Cloud Condensation Nucleus Activity ‐ Part 2: Including Solubility." *Atmospheric Chemistry and Physics Discussions*, vol. 8, no. 2, 25 Oct. 2008, pp. 5939–5955., doi:10.5194/acpd-8-5939-2008.
- Poeschl, Ulrich. "Atmospheric Aerosols: Composition, Transformation, Climate and Health Effects." *Angewandte Chemie International Edition*, vol. 37, no. 7, 14 Jan. 2006, doi:10.1002/chin.200607299.

- Rosenfeld, Daniel, and Meinrat O Andreae. "Aerosol-Cloud-Precipitation Interactions. Part 1. The Nature and Sources of Cloud-Active Aerosols." *Earth-Science Reviews*, vol. 89, no. 1-2, July 2008, pp. 13–41., doi:10.1016/j.earscirev.2008.03.001.
- Schwarz, J. P., et al. "Global-Scale Black Carbon Profiles Observed in the Remote Atmosphere and Compared to Models." *Geophysical Research Letters*, vol. 37, no. 18, 28 Sept. 2010, doi:10.1029/2010gl044372.
- Schwarz, J. P., et al. "Single-Particle Measurements of Midlatitude Black Carbon and Light-Scattering Aerosols from the Boundary Layer to the Lower Stratosphere." *Journal of Geophysical Research*, vol. 111, no. D16, Aug. 2006, doi:10.1029/2006jd007076.
- Seinfeld, John H., and Spyros N. Pandis. *Atmospheric Chemistry and Physics: from Air Pollution to Climate Change*. John Wiley & Sons, 2016.
- Simoneit, B., et al. "Levoglucosan, a Tracer for Cellulose in Biomass Burning and Atmospheric Particles." *Atmospheric Environment*, vol. 33, no. 2, Jan. 1999, pp. 173–182., doi:10.1016/s1352-2310(98)00145-9.
- Sinha, Parikhit. "Distributions of Trace Gases and Aerosols during the Dry Biomass Burning Season in Southern Africa." *Journal of Geophysical Research*, vol. 108, no. D17, Sept. 2003, doi:10.1029/2003jd003691.
- Squires, P. "The Spatial Variation of Liquid Water and Droplet Concentration in Cumuli." *Tellus*, vol. 10, no. 3, Aug. 1958, pp. 372–380., doi:10.1111/j.2153-3490.1958.tb02024.x.

Stocker, Thomas F. *Climate Change 2013: the Physical Science Basis: Summary for Policymakers, a Report of Working Group I of the IPCC, Technical Summary, a Report Accepted by Working Group I of the. Contribution to the Fifth Assessment Report of the Intergovernmental Panel on Climate Change*. Intergovernmental Panel on Climate Change, 2013.

Tomasi, Claudio, and Angelo Lupi. "Coagulation, Condensation, Dry and Wet Deposition, and Cloud Droplet Formation in the Atmospheric Aerosol Life Cycle." *Atmospheric Aerosols*, 4 Nov. 2016, pp. 115–182., doi:10.1002/9783527336449.ch3.

Trenberth, Kevin E., et al. "Earth's Global Energy Budget." *Bulletin of the American Meteorological Society*, vol. 90, no. 3, July 2009, pp. 311–324., doi:10.1175/2008bams2634.1.

Twomey, S., and P. Squires. "The Influence of Cloud Nucleus Population on the Microstructure and Stability of Convective Clouds." *Tellus*, vol. 11, no. 4, Aug. 1959, pp. 408–411., doi:10.1111/j.2153-3490.1959.tb00050.x.

Twomey, S. "The Influence of Pollution on the Shortwave Albedo of Clouds." *Journal of the Atmospheric Sciences*, vol. 34, no. 7, July 1977, pp. 1149–1152., doi:10.1175/1520-0469(1977)0342.0.co;2.

Wang, Kai, et al. "Implementation and Initial Application of New Chemistry-Aerosol Options in WRF/Chem for Simulating Secondary Organic Aerosols and Aerosol Indirect Effects for Regional Air Quality." *Atmospheric Environment*, vol. 115, Aug. 2015, pp. 716–732., doi:10.1016/j.atmosenv.2014.12.007.

- Warren, S.g., et al. "Global Distribution of Total Cloud Cover and Cloud Type Amounts over the Ocean." Jan. 1988, doi:10.2172/5415329.
- Wood, Robert. "Stratocumulus Clouds." *Monthly Weather Review*, vol. 140, no. 8, Aug. 2012, pp. 2373–2423., doi:10.1175/mwr-d-11-00121.1.
- Zhang, Q., et al. "Ubiquity and Dominance of Oxygenated Species in Organic Aerosols in Anthropogenically-Influenced Northern Hemisphere Midlatitudes." *Geophysical Research Letters*, vol. 34, no. 13, 7 July 2007, doi:10.1029/2007gl029979.
- Zhou, Shan, et al. "Regional Influence of Wildfires on Aerosol Chemistry in the Western US and Insights into Atmospheric Aging of Biomass Burning Organic Aerosol." *Atmospheric Chemistry and Physics Discussions*, 23 Feb. 2016, pp. 1–27., doi:10.5194/acp-2016-823.
- Zuidema, Paquita, et al. "Smoke and Clouds above the Southeast Atlantic: Upcoming Field Campaigns Probe Absorbing Aerosols Impact on Climate." *Bulletin of the American Meteorological Society*, vol. 97, no. 7, 22 Aug. 2016, pp. 1131–1135., doi:10.1175/bams-d-15-00082.1.